TECHNISCHE UNIVERSITÄT MÜNCHEN

Fakultät für Chemie

Lehrstuhl für Biochemie

Structural and biochemical characterization of the YaxAB pore-forming toxin from *Yersinia enterocolitica*

Bastian Loong Wang Yung Shan Bräuning

Vollständiger Abdruck der von der Fakultät für Chemie der Technischen Universität München zur Erlangung des akademischen Grades eines

Doktors der Naturwissenschaften (Dr. rer. nat.)

genehmigten Dissertation.

Vorsitzende/-r: Prof. Dr. Matthias Feige

Prüfende/-r der Dissertation:

1. Prof. Dr. Michael Groll
2. Prof. Dr. Franz Hagn
3. Prof. Dr. Michal Sharon (schriftliche Begutachtung),
   Prof. Dr. Tanja Gulder (mündliche Prüfung)

Die Dissertation wurde am 09.04.2018 bei der Technischen Universität München eingereicht und durch die Fakultät für Chemie am 23.05.2018 angenommen.

Table of contents

Abstract

Many pathogenic bacteria have acquired an arsenal of proteinaceous virulence factors, to counteract and highjack host immune response systems. Among these factors, pore-forming toxins (PFTs) are some of the most conserved and potent. A hallmark of PFTs is their ability to transform from soluble to membrane-bound states, a transition often accompanied by formation of large transmembrane oligomers. The vast majority of structurally elucidated PFTs form homooligomeric assemblies and produce β-barrel type pores (β-PFT). YaxAB from *Yersinia enterocolitica*, along with its orthologues from insect and plant pathogens, are two-component PFTs predicted to be entirely α-helical. As a putative virulence factor, obtaining mechanistic insights into its binary mode of action would inform future efforts to target the proteins therapeutically as well as to exploit them for biotechnological purposes. In this thesis, structures of the soluble components YaxA and YaxB could be obtained by X-ray crystallography, along with a cryo-electron microscopy structure of the reconstituted YaxAB pore. Together with structure-guided mutagenesis and biochemical assays, a plausible pathway of pore formation could be proposed. Comparison with the ClyA pore revealed great compositional diversity amongst members from the wider family of ClyA-like α-PFTs, which includes homomeric, binary and tripartite assemblies.

Zusammenfassung

Viele pathogene Bakterien besitzen ein Arsenal an Virulenzfaktoren, wovon der Großteil Proteine sind. Diese Faktoren sind wesentlich daran beteiligt, die wirtseigene Immunabwehr zu modulieren oder dieser entgegenzuwirken. Porenbildende Toxine sind mitunter die ältesten und effektivsten Virulenzfaktoren. Bezeichnend für diese Toxine ist deren Eigenschaft, von löslicher zu membrangebundener Form zu transformieren. Die Bildung von Transmembranoligomeren geht in der Regel mit dieser Transformation einher. Strukturell am besten charakterisiert sind Porentoxine welche homooligomere Komplexe bilden, wobei die Pore aus einem β-Barrel besteht (sogenannte β-Porentoxine). Das YaxAB Toxin aus *Yersinia enterocolitica*, genauso wie Orthologe aus insekten- und pflanzenpathogener Bakterien, ist aufgebaut aus zwei Komponenten und besitzt gänzlich α-helikale Sekundärstruktur. Um diesen potenziellen Virulenzfaktor therapeutisch angreifen zu können oder biotechnologisch auszunutzen, ist dessen Strukturaufklärung notwendig. Im Rahmen dieser Doktorarbeit wurden Strukturen der Untereinheiten YaxA und YaxB röntgenkristallographisch ermittelt und eine Kryo-elektronenmikroskopische Rekonstruktion der YaxAB Pore erreicht. Zusammen mit strukturbasierter Mutagenese und biochemischen Experimenten wird ein möglicher Wirkmechanismus der Porenbildung vorgeschlagen. Der Vergleich mit der ClyA Pore offenbart eine große strukturelle Vielfalt innerhalb der erweiterten Familie ClyA ähnlicher Porentoxine, vertreten durch Ein-, Zwei- und Dreikomponentensysteme.

Abbreviations

2xTY	twice tryptone and yeast extract
α-PFT	alpha-helical pore-forming toxin
ADP	adenosine diphosphate
Ail	attachment invasion locus protein
APS	ammonium persulfate
β-PFT	beta-barrel pore-forming toxin
CDC	cholesterol-dependent cytolysin
cDNA	copy deoxyribonucleic acid
ClyA	cytolysin A
Cry	crystal
Cryo-EM	cryogenic electron microscopy
C-terminal	carboxy-terminal
CytK	cytolysin K
Da	Dalton [g/mol]
DEN	dynamic elastic network
DNA	deoxyribonucleic acid
DNAse	deoxyribonuclease
dNTP	deoxyribonucleotide
DMSO	dimethylsulfoxide

DSBU	disuccinimidyl dibutyric urea
DSMZ	*Deutsche Sammlung von Mikroorganismen und Zellkulturen* (German Collection of Microorganisms and Cell Cultures)
DTT	dithiothreitol
EDTA	ethylenediaminetetraacetic acid
EHEC	enterohemorrhagic *E. coli*
ESI	electrospray ionization
et al.	*et alia*
FF	fast flow
FPLC	fast protein liquid chromatography
FraC	fragaceatoxin C
FSC	Fourier shell correlation
g	gravity
GTPase	guanosine triphosphate hydrolase
Hbl	hemolysin BL
HEPES	4-(2-hydroxyethyl)-1-piperazineethanesulfonic acid
His_6	hexahistidine
Hlg2	gamma-hemolysin component A
HPLC	high-performance liquid chromatography
HT	his_6-TEV
IPTG	isopropylthiogalactoside
LB	lysogeny broth

LLG	log-likelihood gradient
LukF	leukocidin-F subunit precursor
MBP	maltose-binding protein
MPD	2-methyl-2,4-pentanediol
MR	molecular replacement
MS	mass spectrometry
MW	molecular weight
NCS	non-crystallographic symmetry
Nhe	non-hemolytic enterotoxin
ORF	open reading frame
PAGE	polyacrylamide gel electrophoresis
Pax	xenorhabdolysin: Photorhabdus orthologue
PBS	phosphate buffered saline
PCR	polymerase chain reaction
PDB	protein data bank
PEG	polyethylenglycol
PFT	pore-forming toxin
PMSF	phenylmethylsulfonylfluorid
RMSD	root mean square deviation
RovA	regulator of virulence protein A
SAD	single-wavelength anomalous dispersion
SDS	sodium dodecyl sulfate

SOC	super optimal broth with catabolite repression
SUMO	small ubiquitin-related modifier
T_a	annealing temperature
Taq	*Thermus aquaticus* (polymerase)
Tc	toxin complex
TEMED	tetramethylethylenediamine
TEM	transmission electron microscopy
TEV	tobacco etch virus
TLS	translation-liberation-screw
Tris	tris(hydroxymethyl)aminomethane
UV/VIS	ultra-violet/visible
WT	wild-type
Xax	xenorhabdolysin
YadA	adhesin A
Yax	xenorhabdolysin: Yersinia orthologue
Yop	Yersinia outer proteins
Ysc	yop proteins translocation protein

Chapter 1

Introduction

1.1   The enterobacteriaceae: successful pathogens with a broad host spectrum

The family of Enterobacteriaceae comprises a vast number of gram-negative bacterial genera, many of which are characterized by the ability to colonize the intestinal tracts of their host organism[1]. Pathogenic members of this family can colonize an impressive variety of animal hosts, ranging from nematodes to humans. To accomplish the feat of switching between different intermediate and terminal hosts within one life cycle, many pathogenic enterobacteriaceae have acquired complex arsenals of proteinaceous factors, which modulate and block host cellular defense mechanisms[2–4]. This thesis will focus on the structural elucidation of one particular protein factor present in at least six pathogenic enterobacteriaceae genera, with experimental evidence supporting a role in pathogenesis in three genera. As orthologous proteins from *Yersinia enterocolitica* and *Photorhabdus luminescens* were characterized, brief introductions into their respective roles as human and insect pathogens will be outlined in the following section.

1.1.1 The human pathogen *Yersinia enterocolitica*

The family of Yersiniaceae contains three main human pathogenic species: *Y. pestis*, the causative agent of the plague[5], *Y. pseudotuberculosis*, the causative agent of Far East scarlet-like fever[6] and *Y. enterocolitica*, the most common cause of human gastrointestinal yersiniosis[7]. These three species have long served as a model to study the molecular genetic basis of virulence evolution and host species adaptation[8,9], reflected in the very different modes of infection between the three species. While *Y. pestis* infection manifests itself in acute pneumonic plague of the respiratory tissue, *Y. enterocolitica* and *Y. pseudotuberculosis* have evolved into consummate colonizers of the gastrointestinal tract and the underlying lymph system. Infection with *Y. enterocolitica* occurs most frequently via ingestion of contaminated foot – undercooked pork in particular, given the prevalence of high-pathogenicity strains within porcine reservoirs[10] – and less frequently through contaminated blood transfusions, where the species represents the most significant bacterial contaminant given its ability to reproduce at low temperatures[11]. Once in the gastrointestinal tract, the bacterium can adhere to the gut epithelium via a set of chromosomally encoded adherence proteins - Invasin and Ail – as well as a plasmid encoded adherin called YadA[7]. Once past the epithelial layer, the bacterium progresses into the Peyer's patches, which are gut-associated lymph nodes. It is here that the tissue pathologies associated with yersiniosis begin to manifest: as a response to pathogen intrusion, the host immune system initiates inflammatory lymphocyte infiltration at the site of bacterial accumulation[3]. For this, the bacterium possesses a powerful defense mechanism termed the Ysc-Yop Type III system[12], comprising a needle-like injection apparatus at the bacterial cell surface which can deliver a slew of so-called effector proteins (Yops) into the targeted host cell. In the case of macrophages, these Yop effectors are understood to interfere with the phagocytotic machinery allowing the engulfment and destruction of the bacterial pathogen[13].

1.1.2 The insect pathogen *Photorhabdus luminescens*

P. luminescens, belongs to the genus Photorhabdus, which comprise several species of bioluminescent, entomopathogenic (insect pathogenic) bacteria living symbiotically within nematode worms[14]. This bacterium displays a fascinating life cycle, which is split between a

replicative phase within the nematode host (*Heterorhabditis megidis*) and a highly pathogenic phase within the insect larva, into which the bacterium is released upon larval infection by the nematode symbiont. Symbiosis is achieved by the bacterium feeding off the larval biomass (which is gradually decomposed, presumably by a host of toxins released by *P. luminescens* in the later stages of infection), replicating and in turn feeding the nematode. The symbiotic bacteria-nematode pair is so effective in infection and killing of a number of agricultural insect pests, that bacteria-bearing nematodes have become a popular pesticide, persistent in soil for several years[15,16]. Like other pathogenic Enterobacteriaceae such as *Y. enterocolitica*, *P. luminescens* must face a rapid host immune response upon entering the insect prey. Like its human pathogenic relative, *P. luminescens* relies on a Type III injection system to deliver toxic effector proteins into lymphocytes, which inactivate the phagocytotic machinery of these host immune cells[17,18], thereby evading destruction.

1.2   Pore-forming toxins (PFT) as virulence factors of enteropathogenic bacteria from the genera Enterobacteriaceae and Bacillus

The two genera Enterobacteriaceae and Bacillus contain many enteropathogenic species and as mentioned in the previous sections, many Enterobacteriaceae possess an arsenal of protein virulence factors to aid them in host colonization and immune suppression. Amongst the well-characterized group of such factors are the pore-forming toxins (PFT), which are an evolutionarily ancient and widespread protein family ubiquitous both in prokaryotes as well as eukaryotes[4,19]. Indicative of their success as virulence factors, many PFT families are well conserved across genera of enteropathogens. Notably, PFT-encoding genes tend to be retained in high-pathogenicity strains of bacteria while being discarded or interrupted in more innocuous strains[4]. Both Yersinia and Photorhabdus species harbor related PFTs, several of which are now believed to be important virulence factors. Evidence points to their relevance in not only the destruction of host immune cells, but also in other phases of the pathogen's life cycle, such as egress from infected cells and host organelles[20–23].

The largest and best-understood family of PFTs from Yersinia and Photorhabdus are the toxin complexes (Tc), discovered in *P. luminescens*[24,25]. These large (> 1 MDa) protein assemblies carry a membrane receptor binding and pore-forming subunit (the A subunit) and the effector-shuttling and effector proteins (the B and C subunits, respectively). It has been shown that the effector protein (C subunit) being shuttled by the A and B subunits into target cells is an ADP-ribosyl-transferase modifying the actin skeleton and small GTPases[26], which in turn inactive the phagocytotic machinery.

In the related genera Escherichia (including the highly pathogenic enterohemorrhagic strains, EHEC) and Salmonella, the PFT ClyA (also known as HlyE) is another example of a likely virulence factor[27,28]. Unlike the Tc family of proteins, ClyA is a single-component PFT[29] and does not primarily act as a pore to deliver a downstream effector molecule. All biochemical evidence suggest that ClyA mediated cytotoxicity occurs via osmotic lysis of target cells, as ClyA pores possess a large diameter of about 40 Å[30].

From the genus Bacillus, *B. cereus* and *B. thuringiensis* are two enteropathogens of humans and insects, respectively[1]. These two species are known for producing an impressive number of diverse PFTs, with the insecticidal Cry family of PFT from *B. thuringiensis* having found widespread application in agricultural pest control due to their oral toxicity to a variety of insect larvae[31]. An emerging foodborne pathogen of the human gastrointestinal tract[32], infection with *B. cereus* can cause severe diarrheal syndromes, which is believed to be caused by a trio of PFTs termed the Hbl, Nhe and CytK toxins[33].

The great number of different PFT families utilized by a diversity of enteropathogens suggests that these are versatile and successful virulence factors, which have, over the course of evolution, helped the bacteria to endure in the arms race against the host immune system. As will be outlined in the following section, PFTs come in a large variety of sizes and shapes and have been subject to many years of structural research. Since the focus of this thesis is placed on PFT structure and function, the major classes of bacterial PFTs will be discussed in some detail.

1.3   Structure and mechanism of PFTs

A hallmark of all PFTs studied to date is their ability to transform from soluble to membrane-bound oligomeric states[19]. This feature is important, as in many cases these soluble proteins, once translated in the bacterial cytosol, need to be released into the extracellular space and bind to their target cells. This release can occur via secretion, in which case the PFT monomers carry secretion signals and are called exotoxins. Alternatively, synthesized PFT proteins can be released upon destruction of the bacterial cell (for instance when targeted by the host immune system) and are called endotoxins.

For cell binding, numerous PFTs have evolved highly specific binding interfaces with a receptor molecule on susceptible membranes. These receptors can be a cell type specific protein as in the example of intermedilysin binding to the CD59 protein of the human complement system[34] or the well-studied case of various leukocidin PFTs binding to different classes of chemokine receptors[35–37]. In other instances, binding to a particular lipid in the target membrane is necessary[38,39]. Despite this biologically relevant affinity to particular cell surface molecules, many PFTs *in vitro* can be induced to assemble into their membrane pore state in absence of a lipid bilayer, for example by treatment with detergent[29].

The final step in all PFT modes of action is the formation of a transmembrane pore. This usually involves the exposure of amphipathic moieties, previously tucked inside the protein interior in the soluble state. The assembly paths can differ greatly between PFT families. Monomers can bind separately to membranes and then oligomerize sequentially towards pore formation, as in the case of ClyA[40]. More often, a soluble and oligomeric pre-pore structure is formed, which binds as a high-molecular weight (MW) complex to membranes and exposes the transmembrane domains in a concerted fashion[41,42]. All structurally elucidated PFTs fall into two structural groups, depending on the secondary structure of the transmembrane pore: α-PFTs for alpha-helical pores and β-PFTs for beta-barrel pores. Examples for each class are discussed in the following sections.

1.3.1 Homomultimeric β-PFT

β-PFTs with homomultimeric pore assemblies are vastly overrepresented amongst structurally elucidated PFTs. They are characterized by a single protein component carrying both membrane-binding and lytic domains. α-hemolysin from *Staphylococcus aureus* was the first PFT pore structure solved in 1996 by Eric Gouaux and colleagues[43] (incidentally before the soluble monomer structure was determined by the same group[44]) and to this day remains prototypical for the assembly principle of many homomultimeric β-PFTs. **Figure 1.1** shows a gallery of representative β-PFTs, with available structures for monomers and pore assemblies. Though varying in subunit stoichiometry and overall size (ranging from seven to 42 subunits for α-hemolysin and pneumolysin, respectively), one common mechanistic feature of β-PFTs is the exposure of β-hairpin elements from the monomers upon oligomerization into a β-barrel transmembrane pore (**Fig. 1.1a**). For the majority of β-PFTs studied (including the anthrax protective antigen[45] not shown here) a single hairpin structure containing two β-strands is contributed from each toxin protomer, whereas four β-strands are exposed per protomer for cholesterol dependent cytolysins (CDC), as represented by pneumolysin[46]. An interesting aspect of this transition from soluble to pore state is the degree to which structural elements of the soluble protein are remodeled to accommodate pore formation. This can be a localized patch already possessing much of the secondary structure of the final pore, such as the so-called pre-stem region of α-hemolysin, or a more extensive network of interactions which needs to be remodeled, as in the case of lysenin or pneumolysin. While the similarities on the primary sequence level are negligible between α-hemolysin and lysenin – and the tertiary structures show different folds – both these PFTs contribute a two-stranded β-hairpin per protomer in assembling the transmembrane pore. Other similarities in structure and mechanism between PFT families unrelated on the sequence level will be discussed throughout this thesis and are amongst the most characteristic aspects of these proteins.

While strict secondary structure constraints underlie the architecture of any β-barrel, β-PFTs from across different families nevertheless display an impressive range of stoichiometry, ranging from seven to 42 protomers (**Fig. 1.1b**). A distinct "mushroom" appearance, stemming from the often-voluminous extramembrane domains, is common to many β-PFTs. These

Fig. 1.1 Gallery of representative homomultimeric β-PFTs in their soluble and pore-protomeric forms. a) Structural transition from solube (*left*) to protomeric (*right*) conformation. Protein regions becoming part of the transmembrane pore are colored in gold. The corresponding PDB codes are: 4YHD (α-hemolysin, monomer), 7AHL (α-hemolysin, pore), 1XEZ (Vc cytolysin, monomer), 3O44 (Vc cytolysin, pore), 3ZXG (Lysenin, monomer), 5EC5 (Lysenin, pore), 5AOD (Pneumolysin, monomer), 5LY6 (Pneumolysin, pore). b) Two orthogonal views of the pore assemblies from the respective PFTs in a). One protomer is highlighted in yellow. Different PFT cartoons are not shown to scale.

domains can carry important membrane-targeting moieties, such as binding pockets for specific lipid head groups [47]. In some cases, these soluble domains can actually dip partially into the membrane and expand the hydrophobic footprint considerably.

1.3.2 Homomultimeric α-PFTs

Compared to the wealth of structural data on β-PFTs, much fewer α-PFTs – that is PFTs forming α-helical transmembrane pores – have been structurally elucidated. In 2017 there were three α-PFTs with solved structures for both soluble components and assembled pores and all three formed homomultimeric complexes (**Fig. 1.2**). Nevertheless, these structures revealed a striking diversity of pore architectures and lytic mechanisms. Smallest in size amongst these α-PFTs, the eukaryotic Fragaceatoxin C (FraC)[48] presumably forms a pre-pore oligomer on target membranes followed by a switchblade-like outward movement of the amphipathic helices that perforate the lipid bilayer. Forming a much larger complex of 400 kDa, Cytolysin A (ClyA) from *E. coli* is perhaps the best understood α-PFT in terms of its assembly pathway, thanks to a series of elegant structural and spectroscopic investigations by the Glockshuber group[30,40]. Transformation of the soluble ClyA monomer into the pore oligomer entails a massive rearrangement of the protein backbone in which more than half of all residues partake (see **Fig. 1.2a**). Unlike many other PFTs, ClyA does not form pre-pores but rather assembles into the final 12-meric pore by incremental association of membrane-bound, partially oligomerized intermediates[40]. The toxin complex A (TcA) PFT – acting most famously as a toxin injector in insect pathogens, as outlined in section 1.2 – is the most complex homomultimeric α-PFT characterized to date[49,50]. As the pore-forming subunit of the toxin complex, this impressive protein achieves membrane perforation by an injector-like mechanism, extruding its α-helical vuvuzela-shaped transmembrane channel out of a pH-gated shell. TcA is not a classical PFT in the sense that its soluble state is never monomeric but rather a pentamer.

As these three examples suggest, PFTs accomplish their remarkable transition through many distinct routes. **Figure 1.3** illustrates that while the membrane thickness that needs to be traversed remains approximately constant for all PFT classes, toxin families have evolved

tremendous structural and mechanistic diversity to achieve the feat of transmembrane pore formation.
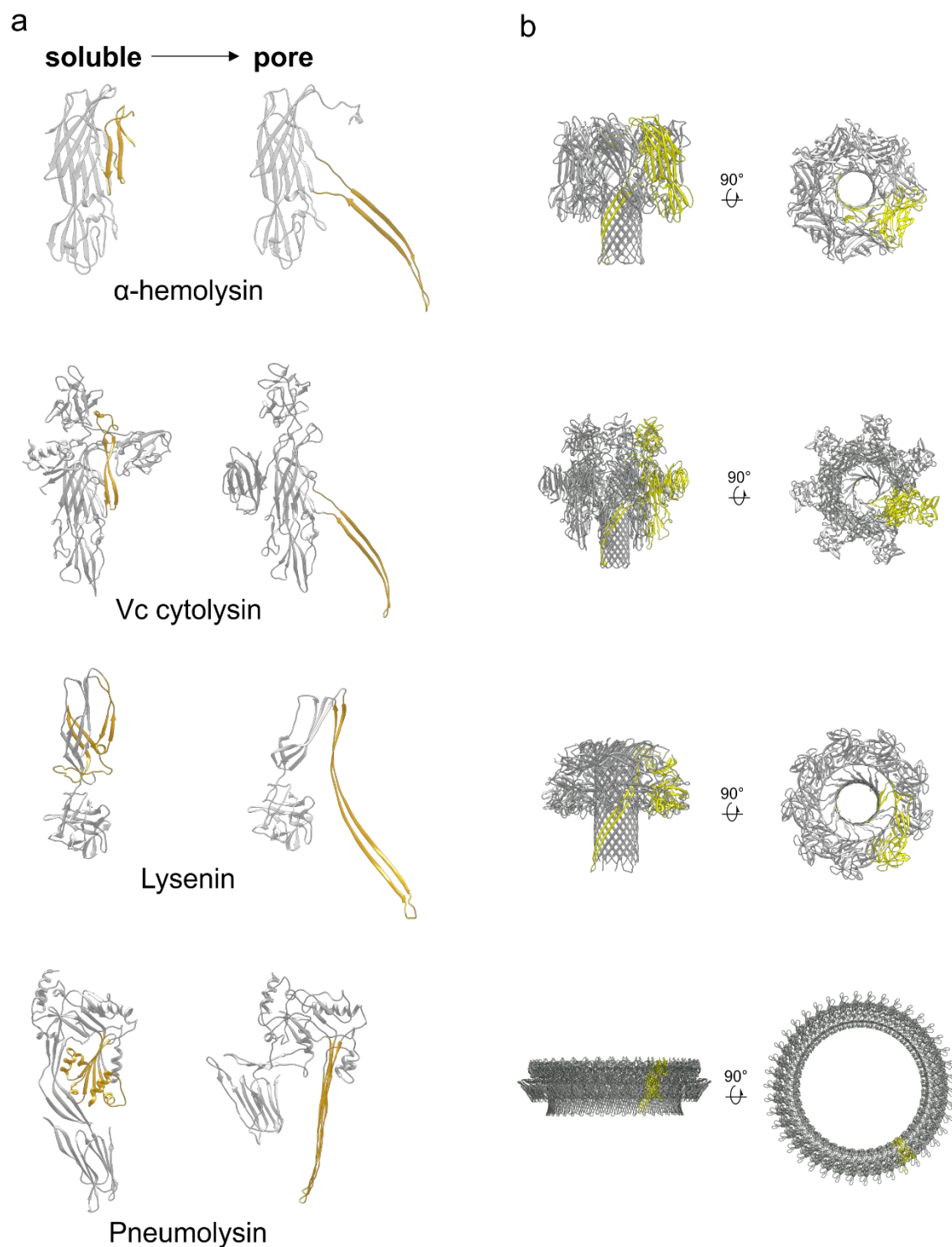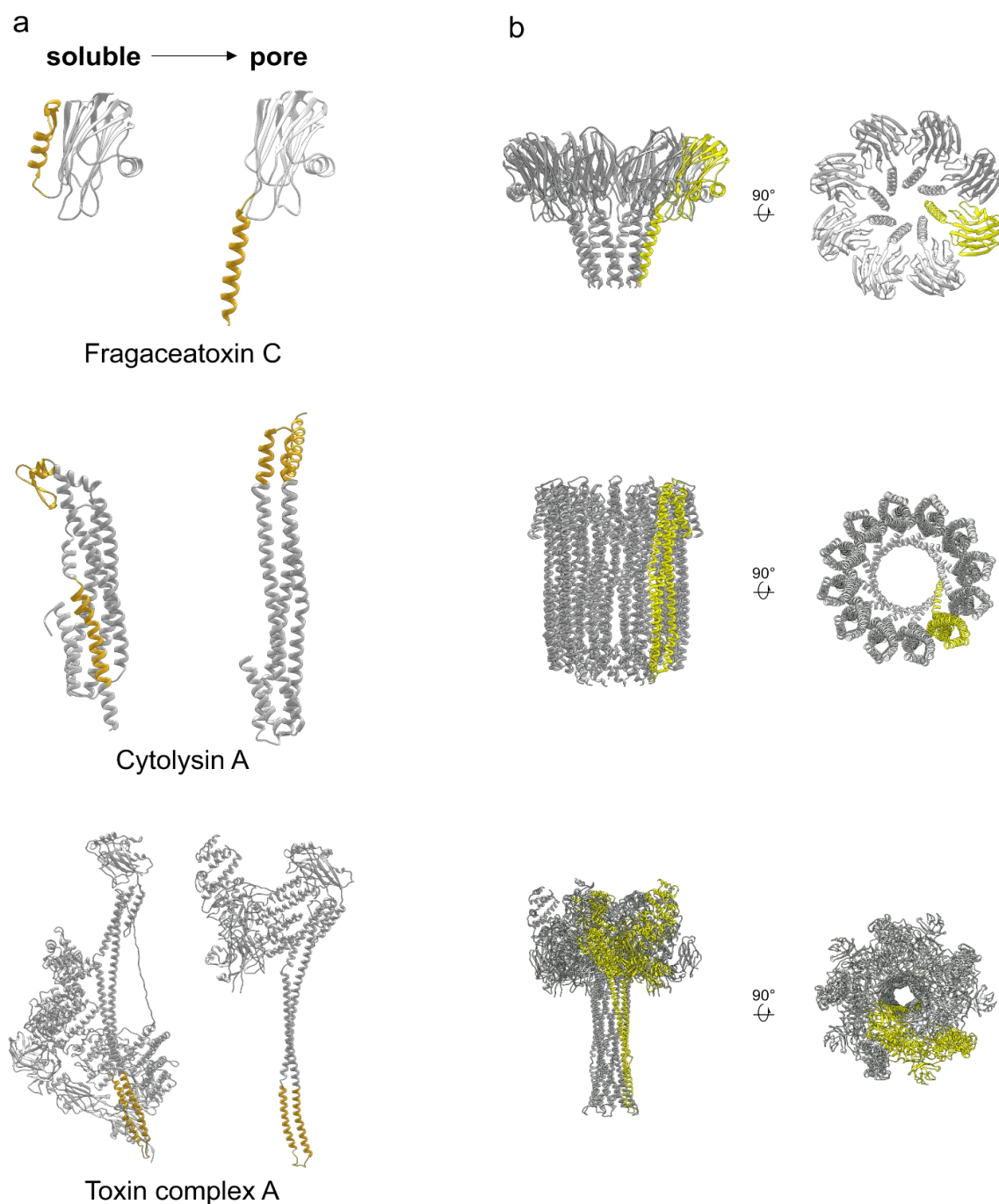

Fig. 1.2 Gallery of representative homomultimeric α-PFTs in their soluble and pore-protomeric forms. a) Structural transition from solube (*left*) to protomeric (*right*) conformation. Protein regions becoming part of the transmembrane pore are colored in gold. The corresponding PDB codes are: 3VWI (Fragaceatoxin C, monomer), 4TSY (Fragaceatoxin C, pore), 1QOY (Cytolysin A, monomer), 2WCD (Cytolysin A, pore), 4O9Y (Toxin complex A, monomer), 5LKI (Toxin complex A, pore). b) Two orthogonal views of the pore assemblies from the respective PFTs in a). One protomer is highlighted in yellow. Different PFT cartoons are not shown to scale.
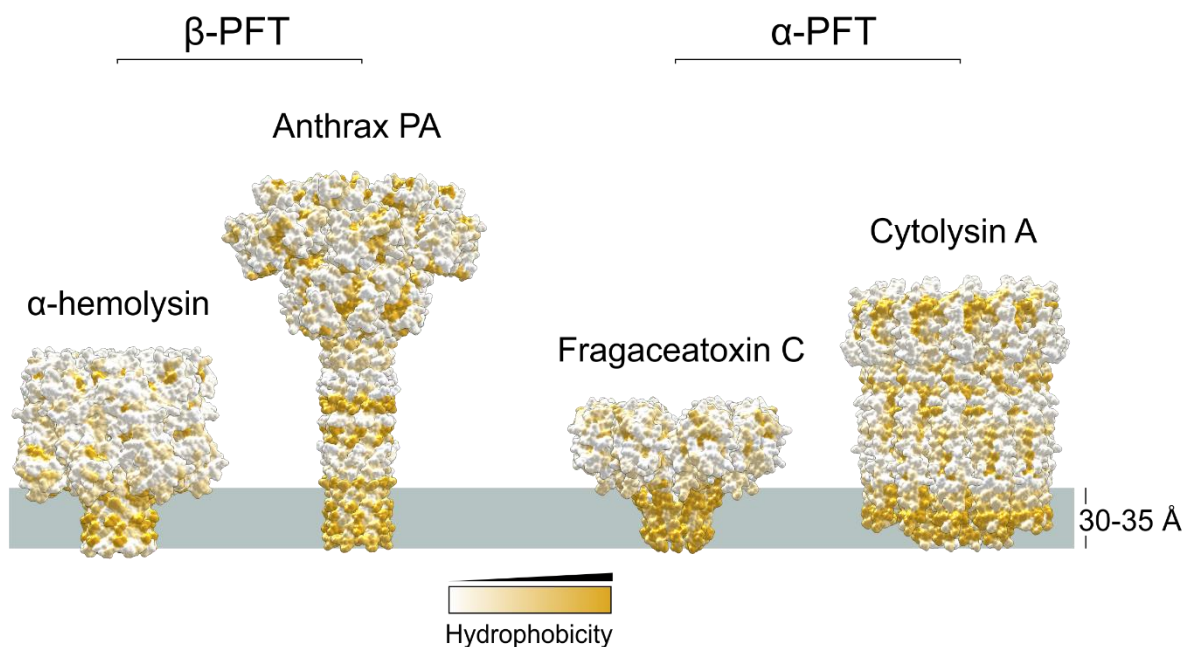
Fig. 1.3 Hydrophobic surface rendering of PFTs delineates their approximate transmembrane regions. Shown are the pores of α-hemolysin (PDB code 7AHL), anthrax protective antigen (PA, PDB code 3J9C), Fragaceatoxin C (PDB code 4TSY), Cytolysin A (PDB code 1Q0Y). Surfaces are colored from hydrophilic (white) to hydrophobic (gold). The approximate membrane boundaries are indicated by the grey box.

1.3.3 Heteromultimeric PFT

At the time of writing of this thesis, only one high-resolution structural study on a heteromultimeric PFT existed in the literature. This work revealed the bicomponent architecture of γ-hemolysin, an octameric β-PFT of the α-hemolysin toxin fold and an important virulence factor of *Staphylococcus aureus*[47]. As **Figure 1.4a** illustrates, the two components, LukF and Hlg2, share 30 % sequence identity and produce a β-hairpin extrusion upon pore formation just like α-hemolysin.

Though structurally very similar (RMSD of 1.1 Å between C_α), LukF and Hlg2 have distinct functional roles in pore formation. Featuring a lipid head group binding moiety, LukF is the toxin component binding initially to susceptible membranes[44]. In the crystal structure of the pore, this moiety is occupied by an organic solvent molecule (2-methyl-2,4-pentanediol, MPD), which can induce oligomerization of LukF and Hlg2 in solution[51] (**Fig. 1.4b**).
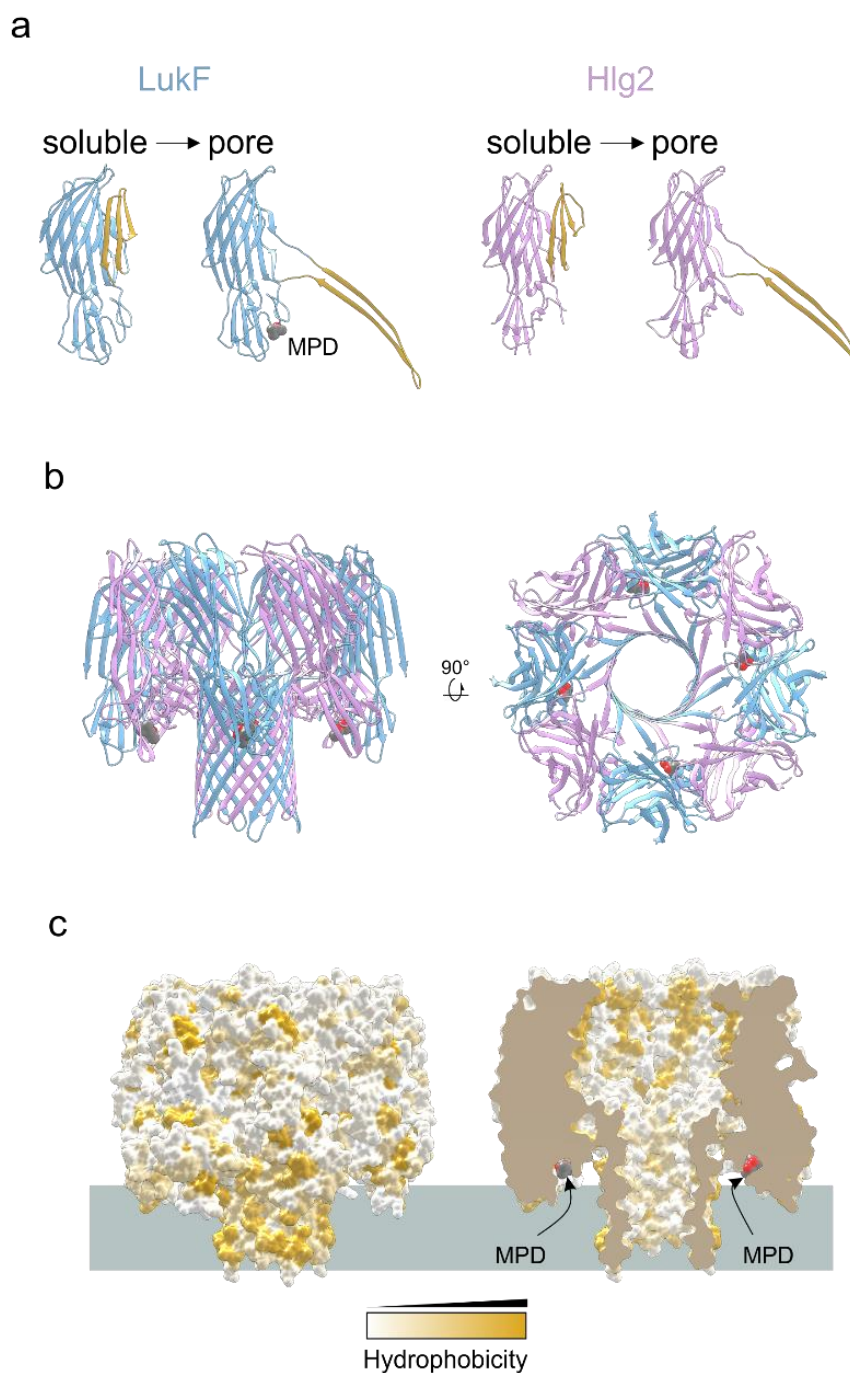
Fig. 1.4 The heteromultimeric β-PFT γ-hemolysin. a) Conformational changes going from monomeric to protomeric states for LukF (blue) and Hgl2 (pink). Regions of the protein becoming part of the transmembrane pore are colored in gold. The 2-methyl-2,4-pentanediol (MPD) molecule bound to protomeric LukF is shown in sphere representation. PDB codes are: 1LKF (LukF, soluble), 2QK7 (Hlg2, soluble), 3B071 (pore assembly). (b) Ribbon model of the heteromultimeric γ-hemolysin pore assembled in the presence of MPD. c) Surface rendering of the pore according to hydrophobicity. Approximate membrane boundaries are indicated by the grey box. A clipped view into the pore interior (right) visualizes the MPD binding pockets of LukF, which at this distance to the hydrophobic membrane plane mimic phospholipid head groups.

Looking at the approximate membrane boundaries of the γ-hemolysin pore, this MPD molecule seems to mimic a lipid head group (**Fig. 1.4c**).

Though perhaps not as widely distributed as homomultimeric PFT families, heteromeric PFTs are found in several human pathogenic bacteria, such as the tripartite Nhe and Hbl α-PFTs of *B. cereus* outlined in **Section 1.2**. These multicomponent PFTs were found to possess a complex sequential mode of assembly involving the consecutive association of the three toxin components upon targeted membranes[52]. Interestingly, the toxin components NheA and HblB were shown to possess structural similarity to each other and to ClyA, the latter acting as a homomultimeric PFT as outlined above[53,54].

A more recently discovered two-component PFT family termed the XaxAB toxins, after the prototypic orthologue from *Xenorhabdus nematophila*[55], was shown to possess sequence similarity to ClyA and Hbl-B. The structural and mechanistic analysis of this PFT family was the goal of this thesis. In the following section, published literature on the biology and biochemistry of XaxAB orthologues will be reviewed.

1.4   The XaxAB family of heteromultimeric α-PFTs

Xenorhabdus nematophila is an insect pathogen very closely related to members of the Photorhabdus genus described in **Section 1.1.2**[1]. It was shown that *X. nematophila* liquid cultures secrete at least two protein factors into the growth medium, which are strongly cytotoxic to insects[56]. In 2007, Brehelin and colleagues identified one of the main cytolytic factors in *X. nematophila* cultures as an uncharacterized pair of proteins, which they termed XaxA and XaxB[55]. The authors demonstrated that the two proteins act as a cytolytic protein complex, XaxAB, with orthologues in other insect pathogens like *P. luminescens* and *Pseudomonas entomophila*; human pathogens like *Y. enterocolitica* and *Proteus mirabilis*; and even plant pathogens like *Pseudomonas synringae*. A follow-up study on the biological role of XaxAB has revealed the toxin to be expressed in the latest stages of infection, when the bacterium has spread inside the insect larva[57]. It was proposed that XaxAB functions in degrading the insect cadaver, making nutrients available to *X. nematophila* as well as allowing the bacterium and its

nematode symbiont to escape the larval body. Supporting the notion that XaxAB is a virulence factor is the observation that the genes encoding XaxA and XaxB are disrupted in non-virulent strains of *X. bovienii* (a related species of Xenorhabdus)[58]. Orthologues of XaxAB have been characterized in two other bacterial pathogens, *Y. enterocolitica*[59] and *P. luminescens*[60].

A 2013 study by Miller and colleagues[59] investigated the biological role of *Y. enterocolitica* XaxAB orthologue (YaxAB) in a murine infection model. The authors had previously undertaken an expression profiling study to identify new transcriptional targets of the Yersinia master virulence regulator RovA[61]. This earlier study showed that the small operon encoding YaxA and YaxB was under strong transcriptional stimulation by RovA, pointing to a role in virulence. In the 2013 paper, a *Y. enterocolitica* YaxAB deletion strain (*ΔyaxAB*) was found to cause an altered splenic tissue pathology in infected mice compared to the wild-type (WT) strain. More specifically, the number of splenic inflammatory lesions observed was significantly higher in the toxin knock-out strain, leading the authors to suggest that YaxAB may have a role in host immunosuppression. Incidentally, *in vitro* cytolytic activity of YaxAB was more pronounced towards immune cells compared to epithelial or cancer cells. The authors additionally identified a distant but detectable protein sequence similarity of YaxA to the α-PFTs ClyA and the HblB subunit of the tripartite Hbl toxin, prompting the authors to generate a homology model of YaxA based on HblB. Focusing on the XaxAB orthologue from *P. luminescens* ("PaxAB", following previous nomenclature), a 2014 study[60] could confirm the insecticidal and biochemical properties observed with XaxAB.

A number of conclusions on the biochemical mode of action of XaxAB orthologues can be drawn from the studies cited above. 1) Both XaxA and XaxB are absolutely required for cytolytic activity and neither subunit shows toxicity when administered alone. 2) A mixture of XaxA and XaxB, when expressed separately, shows no cytolytic activity. 3) Demonstrated for *X. nematophila* and *Y. enterocolitica* orthologues, adding XaxA and XaxB sequentially to susceptible membranes is necessary for cytolytic activity *in vitro*. Reversing the order of contact results in no cytolysis. These conclusions imply a strong functional divergence of XaxA and XaxB, presumably into membrane-binding (XaxA) and lytic components (XaxB).

Bibliography

1. *The prokaryotes: a handbook on the biology of bacteria*. (Springer, 2006).

2. Holst, O. *Bacterial toxins: methods and protocols*. (Humana Press, 2000).

3. Finlay, B. B. & McFadden, G. Anti-Immunology: Evasion of the Host Immune System by Bacterial and Viral Pathogens. *Cell* **124,** 767–782 (2006).

4. Los, F. C. O., Randis, T. M., Aroian, R. V. & Ratner, A. J. Role of Pore-Forming Toxins in Bacterial Infectious Diseases. *Microbiol. Mol. Biol. Rev.* **77,** 173–207 (2013).

5. Perry, R. D. & Fetherston, J. D. Yersinia pestis--etiologic agent of plague. *Clin. Microbiol. Rev.* **10,** 35–66 (1997).

6. Amphlett, A. Far East Scarlet-Like Fever: A Review of the Epidemiology, Symptomatology, and Role of Superantigenic Toxin: *Yersinia pseudotuberculosis-* Derived Mitogen A. *Open Forum Infect. Dis.* **3,** ofv202 (2016).

7. Bottone, E. J. Yersinia enterocolitica: the charisma continues. *Clin. Microbiol. Rev.* **10,** 257–276 (1997).

8. Wren, B. W. The Yersiniae — a model genus to study the rapid evolution of bacterial pathogens. *Nat. Rev. Microbiol.* **1,** 55–64 (2003).

9. McNally, A., Thomson, N. R., Reuter, S. & Wren, B. W. 'Add, stir and reduce': Yersinia spp. as model bacteria for pathogen evolution. *Nat. Rev. Microbiol.* **14,** 177–190 (2016).

10. Bhaduri, S., Wesley, I. V. & Bush, E. J. Prevalence of Pathogenic Yersinia enterocolitica Strains in Pigs in the United States. *Appl. Environ. Microbiol.* **71,** 7117–7121 (2005).

11. Guinet, F., Carniel, E. & Leclercq, A. Transfusion-Transmitted Yersinia enterocolitica Sepsis. *Clin. Infect. Dis.* **53,** 583–591 (2011).

12. Cornelis, G. R. The Yersinia Ysc–Yop 'Type III' weaponry. *Nat. Rev. Mol. Cell Biol.* **3,** 742–754 (2002).

13. Grosdent, N., Maridonneau-Parini, I., Sory, M.-P. & Cornelis, G. R. Role of Yops and adhesins in resistance of Yersinia enterocolitica to phagocytosis. *Infect. Immun.* **70,** 4165–4176 (2002).

14. Waterfield, N. R., Ciche, T. & Clarke, D. Photorhabdus and a host of hosts. *Annu. Rev. Microbiol.* **63,** 557–574 (2009).

15. Lacey, L. A. & Georgis, R. Entomopathogenic Nematodes for Control of Insect Pests Above and Below Ground with Comments on Commercial Production. *J. Nematol.* **44,** 218–225 (2012).

16. Puža, V., Mráček, Z. & Nermut, J. Novelties in Pest Control by Entomopathogenic and Mollusc-Parasitic Nematodes. in *Integrated Pest Management (IPM): Environmentally Sound Pest Management* (eds. Gill, H. K. & Goyal, G.) (InTech, 2016). doi:10.5772/64578

17. Brugirard-Ricaud, K. *et al.* Variation in the effectors of the type III secretion system among Photorhabdus species as revealed by genomic analysis. *J. Bacteriol.* **186,** 4376–4381 (2004).

18. Brugirard-Ricaud, K. *et al.* Site-specific antiphagocytic function of the Photorhabdus luminescens type III secretion system during insect colonization. *Cell. Microbiol.* **7,** 363–371 (2005).

19. Dal Peraro, M. & van der Goot, F. G. Pore-forming toxins: ancient, but never really out of fashion. *Nat. Rev. Microbiol.* **14,** 77–92 (2016).

20. Frehel, C. *et al.* Capacity of ivanolysin O to replace listeriolysin O in phagosomal escape and in vivo survival of Listeria monocytogenes. *Microbiol. Read. Engl.* **149,** 611–620 (2003).

21. Hara, H. *et al.* Cytolysin-Dependent Escape of the Bacterium from the Phagosome Is Required but Not Sufficient for Induction of the Th1 Immune Response against Listeria monocytogenes Infection: Distinct Role of Listeriolysin O Determined by Cytolysin Gene Replacement. *Infect. Immun.* **75,** 3791–3801 (2007).

22. Roiko, M. S. & Carruthers, V. B. New roles for perforins and proteases in apicomplexan egress. *Cell. Microbiol.* **11,** 1444–1452 (2009).

23. Di Venanzio, G., Lazzaro, M., Morales, E. S., Krapf, D. & García Véscovi, E. A pore-forming toxin enables *Serratia* a nonlytic egress from host cells: *Serratia* exits from host cells by a nonlytic strategy. *Cell. Microbiol.* **19,** e12656 (2017).

24. Blackburn, null, Golubeva, null, Bowen, null & Ffrench-Constant, null. A novel insecticidal toxin from photorhabdus luminescens, toxin complex a (Tca), and its histopathological effects on the midgut of manduca sexta. *Appl. Environ. Microbiol.* **64,** 3036–3041 (1998).

25. Waterfield, N., Hares, M., Hinchliffe, S., Wren, B. & ffrench-Constant, R. The insect toxin complex of Yersinia. *Adv. Exp. Med. Biol.* **603,** 247–257 (2007).

26. Lang, A. E. *et al.* Photorhabdus luminescens toxins ADP-ribosylate actin and RhoA to force actin clustering. *Science* **327,** 1139–1142 (2010).

27. Ludwig, A., von Rhein, C., Bauer, S., Hüttinger, C. & Goebel, W. Molecular analysis of cytolysin A (ClyA) in pathogenic Escherichia coli strains. *J. Bacteriol.* **186,** 5311–5320 (2004).

28. Fuentes, J. A., Villagra, N., Castillo-Ruiz, M. & Mora, G. C. The Salmonella Typhi hlyE gene plays a role in invasion of cultured epithelial cells and its functional transfer to S. Typhimurium promotes deep organ infection in mice. *Res. Microbiol.* **159,** 279–287 (2008).

29. Wallace, A. J. *et al.* E. coli hemolysin E (HlyE, ClyA, SheA): X-ray crystal structure of the toxin and observation of membrane pores by electron microscopy. *Cell* **100,** 265–276 (2000).

30. Mueller, M., Grauschopf, U., Maier, T., Glockshuber, R. & Ban, N. The structure of a cytolytic α-helical toxin pore reveals its assembly mechanism. *Nature* **459,** 726–730 (2009).

31. Pardo-López, L., Soberón, M. & Bravo, A. Bacillus thuringiensis insecticidal three-domain Cry toxins: mode of action, insect resistance and consequences for crop protection. *FEMS Microbiol. Rev.* **37,** 3–22 (2013).

32. Bottone, E. J. Bacillus cereus, a Volatile Human Pathogen. *Clin. Microbiol. Rev.* **23,** 382–398 (2010).

33. Stenfors Arnesen, L. P., Fagerlund, A. & Granum, P. E. From soil to gut: *Bacillus cereus* and its food poisoning toxins. *FEMS Microbiol. Rev.* **32,** 579–606 (2008).

34. Johnson, S., Brooks, N. J., Smith, R. A. G., Lea, S. M. & Bubeck, D. Structural basis for recognition of the pore-forming toxin intermedilysin by human complement receptor CD59. *Cell Rep.* **3,** 1369–1377 (2013).

35. Alonzo III, F. *et al.* CCR5 is a receptor for Staphylococcus aureus leukotoxin ED. *Nature* **493,** 51–55 (2012).

36. Reyes-Robles, T. *et al.* Staphylococcus aureus leukotoxin ED targets the chemokine receptors CXCR1 and CXCR2 to kill leukocytes and promote infection. *Cell Host Microbe* **14,** 453–459 (2013).

37. Spaan, A. N. *et al.* The staphylococcal toxins γ-haemolysin AB and CB differentially target phagocytes by employing specific chemokine receptors. *Nat. Commun.* **5,** 5438 (2014).

38. Abrami, L. & van Der Goot, F. G. Plasma membrane microdomains act as concentration platforms to facilitate intoxication by aerolysin. *J. Cell Biol.* **147,** 175–184 (1999).

39. Tweten, R. K. Cholesterol-dependent cytolysins, a family of versatile pore-forming toxins. *Infect. Immun.* **73,** 6199–6209 (2005).

40. Benke, S. *et al.* The assembly dynamics of the cytolytic pore toxin ClyA. *Nat. Commun.* **6,** 6198 (2015).

41. Degiacomi, M. T. *et al.* Molecular assembly of the aerolysin pore reveals a swirling membrane-insertion mechanism. *Nat. Chem. Biol.* **9,** 623–629 (2013).

42. Leung, C. *et al.* Real-time visualization of perforin nanopore assembly. *Nat. Nanotechnol.* **12,** 467–473 (2017).

43. Song, L. *et al.* Structure of staphylococcal alpha-hemolysin, a heptameric transmembrane pore. *Science* **274,** 1859–1866 (1996).

44. Olson, R., Nariya, H., Yokota, K., Kamio, Y. & Gouaux, E. Crystal structure of staphylococcal LukF delineates conformational changes accompanying formation of a transmembrane channel. *Nat. Struct. Biol.* **6,** 134–140 (1999).

45. Jiang, J., Pentelute, B. L., Collier, R. J. & Zhou, Z. H. Atomic structure of anthrax protective antigen pore elucidates toxin translocation. *Nature* **521,** 545–549 (2015).

46. van Pee, K. *et al.* CryoEM structures of membrane pore and prepore complex reveal cytolytic mechanism of Pneumolysin. *eLife* **6,** (2017).

47. Yamashita, K. *et al.* Crystal structure of the octameric pore of staphylococcal -hemolysin reveals the -barrel pore formation mechanism by two components. *Proc. Natl. Acad. Sci.* **108,** 17314–17319 (2011).

48. Tanaka, K., Caaveiro, J. M. M., Morante, K., González-Mañas, J. M. & Tsumoto, K. Structural basis for self-assembly of a cytolytic pore lined by protein and lipid. *Nat. Commun.* **6,** 6337 (2015).

49. Meusch, D. *et al.* Mechanism of Tc toxin action revealed in molecular detail. *Nature* **508,** 61–65 (2014).

50. Gatsogiannis, C. *et al.* Membrane insertion of a Tc toxin in near-atomic detail. *Nat. Struct. Mol. Biol.* (2016). doi:10.1038/nsmb.3281

51. Tanaka, Y. *et al.* 2-Methyl-2,4-pentanediol induces spontaneous assembly of staphylococcal α-hemolysin into heptameric pore structure. *Protein Sci. Publ. Protein Soc.* **20,** 448–456 (2011).

52. Sastalla, I. *et al.* The Bacillus cereus Hbl and Nhe Tripartite Enterotoxin Components Assemble Sequentially on the Surface of Target Cells and Are Not Interchangeable. *PLoS ONE* **8,** e76955 (2013).

53. Madegowda, M., Eswaramoorthy, S., Burley, S. K. & Swaminathan, S. X-ray crystal structure of the B component of Hemolysin BL fromBacillus cereus. *Proteins Struct. Funct. Bioinforma.* **71,** 534–540 (2008).

54. Ganash, M. *et al.* Structure of the NheA Component of the Nhe Toxin from Bacillus cereus: Implications for Function. *PLoS ONE* **8,** e74748 (2013).

55. Vigneux, F. *et al.* The xaxAB Genes Encoding a New Apoptotic Toxin from the Insect Pathogen Xenorhabdus nematophila Are Present in Plant and Human Pathogens. *J. Biol. Chem.* **282,** 9571–9580 (2007).

56. Brillard, J., Ribeiro, C., Boemare, N., Brehelin, M. & Givaudan, A. Two Distinct Hemolytic Activities in Xenorhabdus nematophila Are Active against Immunocompetent Insect Cells. *Appl. Environ. Microbiol.* **67,** 2515–2525 (2001).

57. Jubelin, G. *et al.* Studies of the dynamic expression of the Xenorhabdus FliAZ regulon reveal atypical iron-dependent regulation of the flagellin and haemolysin genes during insect infection. *Environ. Microbiol.* **13,** 1271–1284 (2011).

58. Bisch, G. *et al.* Comparative Genomics between Two *Xenorhabdus bovienii* Strains Highlights Differential Evolutionary Scenarios within an Entomopathogenic Bacterial Species. *Genome Biol. Evol.* **8,** 148–160 (2016).

59. Wagner, N. J., Lin, C. P., Borst, L. B. & Miller, V. L. YaxAB, a Yersinia enterocolitica Pore-Forming Toxin Regulated by RovA. *Infect. Immun.* **81,** 4208–4219 (2013).

60. Zhang, X. *et al.* XaxAB-like binary toxin from Photorhabdus luminescens exhibits both insecticidal activity and cytotoxicity. *FEMS Microbiol. Lett.* **350,** 48–56 (2014).

61. Cathelyn, J. S., Ellison, D. W., Hinchliffe, S. J., Wren, B. W. & Miller, V. L. The RovA regulons of Yersinia enterocolitica and Yersinia pestis are distinct: evidence that many RovA-regulated genes were acquired more recently than the core genome. *Mol. Microbiol.* **66,** 189–205 (2007).

Chapter 2

Objectives

Orthologues of the YaxAB PFT are implicated as virulence factors both in insect pathogens of the genera Xenorhabdus and Photorhabdus, as well as the human pathogen *Y. enterocolitica*. Structural data is missing entirely on this class of PFTs, precluding a detailed mechanistic understanding of the assembly principle and lytic mode of action. As a two -component PFT and with its subunits predicted to contain only α-helices, elucidating the architecture of the YaxAB PFT would furthemore provide the first structural view on a heteromultimeric α-PFT.

The first objective was to obtain crystal structures of the monomeric forms of YaxA and YaxB. Here, orthologous proteins from several organisms should be tested for recombinant expression levels, solubility and achievable diffraction limits once crystallized. Obtaining reasonable yields of protein in the milligram scale was also crucial in order to perform structure-guided mutagenesis experiments to validate the mechanistic model of toxin action.

With the soluble components at hand, the next important step was to establish a reconstitution protocol for the pore complex. The stoichiometry and overall shape of the pore should be estimated using a combination of analytical ultracentrifugation and negative-stain transmission electron microscopy (TEM). Finally, a structure of the complex at a resolution sufficient for unambiguous assignment of secondary structure was sought: here, the aim was to obtain a cryo-TEM map at high resolution to allow visualization of the subunit conformational changes accompanying pore formation.

Based on both monomeric and pore complex structures, together with a series of biochemical mutagenesis studies, the major goal was to suggest a plausible mechanistic model for YaxAB pore formation, which rationalizes the peculiar properties of this binary PFT.

Chapter 3

Materials & Methods

3.1 Materials

3.1.1 Standard laboratory chemicals

Standard chemicals used for buffer preparation and crystallization were purchased from the following vendors, unless stated otherwise: Anatrace (USA), AppliChem (Germany), Avanti Polar Lipids (USA), Fluka (Germany), Glycon (Germany), Merck (Germany), Sigma-Aldrich (Germany), Serva (Germany), Roth (Germany), VWR (Germany),

3.1.2 Material for molecular cloning and expression vectors

Sources of gene-encoding DNA

Source DNA	Description	Manufacturer
Yersinia enterocolitica subsp. enterocolitica, serovar 8, biovar 1, genomic DNA	Source for amplification of YaxA and YaxB encoding genes	DSZM (Germany)
Synthesized gene encoding PaxB	Synthetic DNA encoding the gene for PaxB	Eurofins Genomics (Germany)

DNA primer list

Primer name	Primer sequence	Description	Manufacturer
T7	TAATACGACTCACTATAGGG	Complementary to the T7 promotor sequence of pRSET-A; used for colony-PCR and DNA sequencing	Biomers (Germany)
pRSET-RP	ATGCTAGTTATTGCTCAGC	Complementary to the T7 terminator sequence of pRSET-A; used for colony-PCR, mutagenesis and DNA sequencing	
pRSET-HT-YaxA-F	<u>CCAACGACCGAAAACCTGTATTTTC AG</u>**GGAATGACACAAACACAATTGG CTATTGATAATGTCTTGG**	Inserting YaxA into pRSET-A vector	
pRSET-HT-YaxA-R	<u>CTGCAGATCTCGAGCTCGGATCC</u>**TT AGCCATACACTTTTTTGTATTCTT TTATTGCC**		
pRSET-HT-YaxB-F	<u>CCAACGACCGAAAACCTGTATTTTC AG</u>**GGAGCCGAAATAAGCACATTTC C**	Inserting YaxB into pRSET-A vector	
pRSET-HT-YaxB-R	<u>CTGCAGATCTCGAGCTCGGATCC</u>**TC AAATCAGCTGTTTGATTAATGAC TCTAAATAGATCTGC**		
pRSET-SUMO-F	<u>GATTACGATATCCCAACGACCGAAA ACCTG</u>**TCGGACTCAGAAGTCAATC AAGAAGCTAAGCC**	Transfer of the SUMO sequence from pET28-SUMO (AG Groll) downstream of the His$_6$ sequence on pRSET-A	
pRSET-SUMO-R	<u>GCAGATCTCGAGCTCGGATCCCTGA AAATA</u>**TCCACCAATCTGTTCTCTG TGAGCCTCAATAATATCG**		

SUMO-YaxA-V264D-F	GAGCAACTAAAGAAAGATTACGATAAGTTT*GAT*GGGTTGTCTTTTACTGGGGCCATAGGCGGT	YaxA foot domain point mutant (reverse primer exactly complementary)
SUMO-YaxA-L266D-F	CTAAAGAAAGATTACGATAAGTTTGTCGGG*GAT*TCTTTTACTGGGGCCATAGGCGGTATAATA	YaxA foot domain point mutant (reverse primer exactly complementary)
SUMO-YaxA-F268D-F	AAAGATTACGATAAGTTTGTCGGGTTGTCT*GAT*ACTGGGGCCATAGGCGGTATAATAGCGATG	YaxA foot domain point mutant (reverse primer exactly complementary)
SUMO-YaxA-I272D-F	AAGTTTGTCGGGTTGTCTTTTACTGGGGCC*GAT*GGCGGTATAATAGCGATGGCTATTACTGGT	YaxA foot domain point mutant (reverse primer exactly complementary)
d238-309YaxA-F	CTGATGGAAAAAAGCAATATGAGGAAATCA**TCTGGATCT**AGCTCGCAAAGAGCATTACAAACTGCGTTA	YaxA head domain (reverse primer exactly complementary)
d153-278YaxB-F	GTAGTGATTATTGAAGGAACCGACAAAGTC**TCTGGATCT**GCCGGTGTTAACGCGATTATTAAAATTGAT	YaxB head domain (reverse primer exactly complementary)
d265-284YaxA-F	CTAAAGAAAGATTACGATAAGTTTGTCGGG**GGAAGTGGATCTGGA**GGTGCTAAAGCTGAAAACGCCAGAAAAGAA	YaxA foot domain deleted (reverse primer exactly complementary)
YaxA-MBP-F	GCAATAAAAGAATACAAAAAAGTGTATGGC**AACACTAGTAAAATCGAAGAAGGTA**	Transferring MBP tag from pMAL vector to YaxA C-terminus
YaxA-MBP-R	GTACCAGCTGCAGATCTCGAGCTCGGATTAA**TCAGCCATGGAATAATTCTCC**	
YaxB-MBP-F	TATTTAGAGTCATTAATCAAACAGCTGATT**AACACTAGTAAAATCGAAGAAGG**	Transferring MBP tag from pMAL vector to YaxB C-terminus
YaxB-MBP-R	GTACCAGCTGCAGATCTCGAGCTCGGATCA**ATCAGCCATGGAATAATTCTCC**	

YaxB-I184C-F	<u>AGAAAAGAGATTGAGAAAAAAAGA GATAAG</u>*TGC*<u>ATAGAAGCCTTGGATG TTATTCGCGAGCAT</u>	Generating pRSET-HT-YaxB-I184C/I229C (reverse primer exactly complementary)
YaxB-I229C-F	<u>GAAATAGAATTGCTTAAACAGTCAT TAGAA</u>*TGC*<u>ACCAAGAAATTATTGGG GCAGTTTTCCGAG</u>	Generating pRSET-HT-YaxB-I184C/I229C (reverse primer exactly complementary)
YaxB-V190C-F	<u>AAAAGAGATAAGATAATAGAAGCC TTGGAT</u>*TGC*<u>ATTCGCGAGCATAATC TGGTCGATGCATTC</u>	Generating pRSET-HT-YaxB-V190C/L223C (reverse primer exactly complementary)
YaxB-L223C-F	<u>TTAGATCTGGCTAAACCTGAAATAG AATTG</u>*TGC*<u>AAACAGTCATTAGAAAT TACCAAGAAATTA</u>	Generating pRSET-HT-YaxB-V190C/L223C (reverse primer exactly complementary)

Expression plasmids

Name of plasmid	Decription	Manufacturer
pRSET-A	High-copy expression vector, Amp^r	Thermo Fischer (Germany)
pRSET-A-His$_6$-SUMO-YaxA	Expression of His$_6$-SUMO-YaxA	This work
pRSET-A-His$_6$-TEV-YaxB	Expression of His$_6$-TEV-YaxB	This work
pRSET-A-His$_6$-SUMO-PaxB	Expression of His$_6$-SUMO-PaxB	This work
pRSET-A-His$_6$-SUMO-YaxA(V264D)	Expression of His$_6$-SUMO-YaxA(V264D) mutant	This work
pRSET-A-His$_6$-SUMO-YaxA(L266D)	Expression of His$_6$-SUMO-YaxA(L266D) mutant	This work
pRSET-A-His$_6$-SUMO-YaxA(F268D)	Expression of His$_6$-SUMO-YaxA(F268D) mutant	This work
pRSET-A-His$_6$-SUMO-YaxA(I272D)	Expression of His$_6$-SUMO-YaxA(I272D) mutant	This work
pRSET-A-His$_6$-SUMO-YaxAΔ(265-284)	Expression of His$_6$-SUMO-YaxA Δ(265-284) mutant	This work

pRSET-A-His$_6$-TEV-YaxB^{Head}	Expression of YaxBΔ(153-278) with Ser-Gly-Ser linker	This work
pRSET-A-His$_6$-SUMO-YaxA^{Head}	Expression of YaxAΔ(238-309) with Ser-Gly-Ser linker	This work
pRSET-A-His$_6$-SUMO-YaxA-MBP	Expression of His$_6$-SUMO-YaxA with C-terminal MBP tag	This work
pRSET-A-His$_6$-TEV-YaxB-MBP	Expression of His$_6$-TEV-YaxB with C-terminal MBP tag	This work
pRSET-His$_6$-TEV-YaxB(I184C/I229C)	Disulfide-locked YaxB foot mutant	This work
pRSET-His$_6$-TEV-YaxB(V190C/L223C)	Disulfide-locked YaxB foot mutant	This work

Enzymes for molecular cloning

Enzyme	Description	Manufacturer
Phusion DNA polymerase	High-fidelity DNA polymerase	NEB (US)
Taq DNA polymerase	Standard purpose DNA polymerase	NEB (USA)
DpnI	Restriction enzyme which digests methylated DNA	Gift from the group of Prof. Aymelt Itzen, TU Munich

3.1.3 Protein and DNA standards

peqGOLD DNA Ladder Mix (100-10,000 bp)	Peqlab (Germany)
Roti-Mark STANDARD (14-200 kDa)	Carl Roth (Germany)

3.1.4 Bacterial strains and growth media

Bacterial strains

Name of strain	Genotype	Manufacturer
E. coli XL1-Blue	*recA1 endA1 gyrA96 thi-1 hsdR17 supE44 relA1 lac* [F *proAB lacI^{q}ZΔM15* Tet^r]	Agilent (USA)

E. coli BL21 (DE3)	*ompT gal dcm lon hsdS_B*($r_B^-m_B^-$) λ(DE3 [*lacI lacUV5-T7p07 ind1 sam7 nin5*]) [*malB+*]$_{K-12}$($λ^S$)	Novagen (USA)
E. coli SoluBL21 (DE3)	BL21 (DE3) parent strain with proprietary mutations to enhance soluble protein expression	Genlantis (USA)

Bacterial growth media

LB medium	Peptone	1 % (w/v)
	Yeast extract	0.5 % (w/v)
	NaCl	0.5 % (w/v)
	(Agar)	2 % (w/v)
SOC medium	Peptone	2 % (w/v)
	Yeast extract	0.5 % (w/v)
	Glucose	20 mM
	$MgSO_4$	10 mM
	NaCl	10 mM
	KCl	2.5 mM
2xTY medium	Peptone	1.6 % (w/v)
	Yeast extract	1 % (w/v)
	NaCl	0.5 % (w/v)
M9 minimal medium	Na_2HPO_4	48 mM
	KH_2PO_4	22 mM
	NaCl	9 mM
	NH_4Cl	19 mM
	$MgSO_4$	2 mM
	Glucose	0.4 % (w/v)
	Vitamins (1000x)	1 mL (see Appendix)
	Trace elements (100x)	10 mL (see Appendix)

3.1.5 FPLC chromatography

All protein purification procedures were performed on an ÄKTA Pure FPLC system (GE Healthcare, USA) operating at 4 °C.

FPLC columns

Name of column	Type of chromatography	Manufacturer
HisTrap crude 5 mL	Nickel affinity	GE Healthcare (USA)
HiTrap TALON crude 5 mL	Cobalt affinity	
Resource Q 6 mL	Anion exchange	
Superdex 75 16/60 HiLoad	Size-exclusion	
Superdex 200 10/300	Size-exclusion	
Superose 6 10/100	Size-exclusion	
HiTrap Desalting 5mL	Desalting	

3.1.6 Protein crystallization

Crystallization screens

Screen name	Manufacturer
Classics Suite	Qiagen (Germany)
Classics II Suite	
JCSG+ Suite	
ComPAS Suite	
Protein Complex Suite	
PEGs Suite	
PEGs II Suite	
PACT Suite	
The MPD Suite	
Additive Screen	Hampton Research (USA)

Crystallization tools

Tool name	Manufacturer
Cooled Incubator Series 3000	RUMED Rubarth Apparate (Germany)
CryoLoop	Hampton Research (USA)

CrystalCap HT Vial	Hampton Research (USA)
CrystalWand Magnetic	Hampton Research (USA)
Intelli-Plate 96-well	Art Robbins Instruments (USA)
Linbro Plate 24-well	Jena Bioscience (Germany)
Siliconized Glass Cover Slides 22mm	Hampton Research (USA)
MICROLAB STARlet	Hamilton (USA)
Phoenix Liquid Handling System	Art Robbins Instruments (USA)
Oryx4 pipetting robot	Douglas Instruments (UK)
Storage dewar HC20	Taylor-Wharton (Germany)
Zoom stereo microscope SZX10/KL1500LCD	Olympus (Japan)

3.1.7 Software

ApE (A Plasmid Editor)	M. Wayne Davis
CCP4 Program Suite 7.0	www.ccp4.ac.uk
Coot 0.8.7	Emsley & Cowtan, 2004[1]
CorelDRAW X8	Corel (Canada)
ESPript 3	Robert & Gouet, 2014[2]
Graph Pad Prism 5	GraphPad Software Inc. (USA)
HOLE	Smart, 1993[3]
Microsoft Office 2013	Microsoft (USA)
PHENIX	Adams et al., 2010[4]
UCSF Chimera	Pettersen et al., 2004[5]
XDS/XSCALE	Kabsch, 2010[6]
Zotero	www.zotero.org

3.2   General biochemical techniques

3.2.1 Molecular cloning

All expression plasmids used in this thesis were generated using the restriction-free cloning approach after Unger et al., 2010[7] (**Fig. 3.1**).
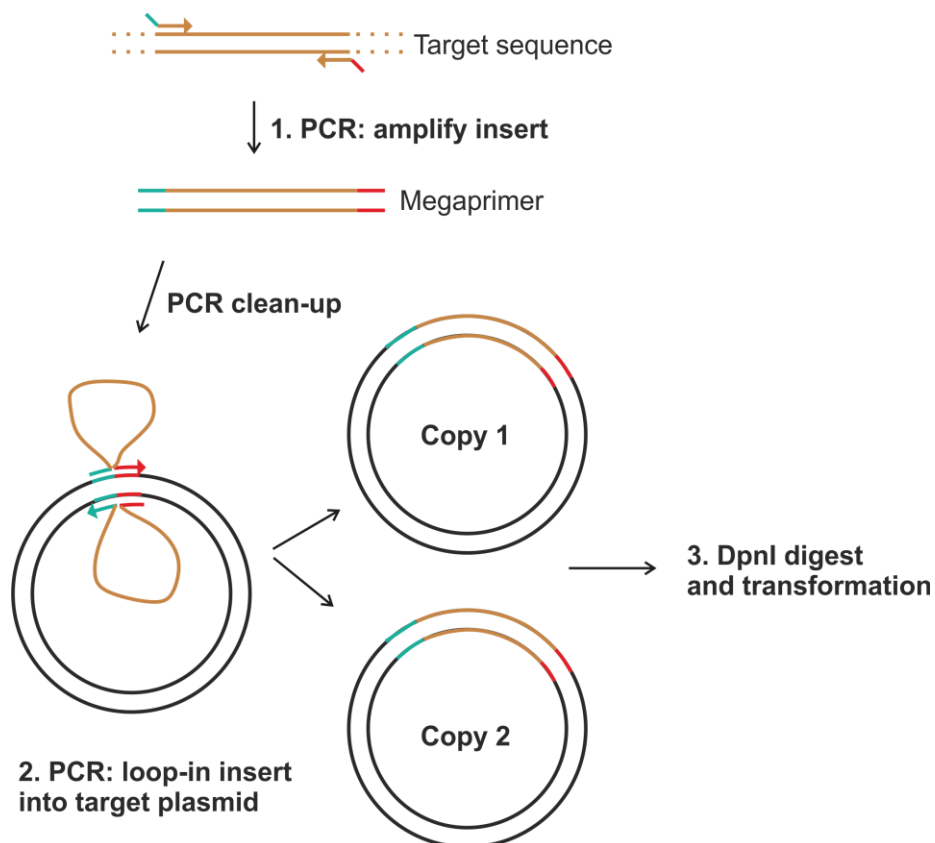
Fig. 3.1 Restriction-free cloning principle. In the first PCR reaction, an insert of interest is amplified using primers 5' complementary to 30 base pairs upstream of the target vector insertion site and 3' complementary to the start of the insert sequence. The same design holds true for the reverse primer, with 5' complementarity to the 30 base pairs downstream of the target vector insertion site. In a second PCR, this megaprimer is inserted into a defined site on the target vector by whole-plasmid amplification. Lastly, the PCR reaction is digested with DpnI to eliminate original, methylated target vectors and transformed into competent *E. coli* cells.

The insert in transformant colonies were screened by standard colony PCR (polymerase chain reaction) and subsequently sent to Sanger sequence analysis at GATC sequencing services (Germany).

PCR reaction mixture (per 50 μL) for 1. PCR: megaprimer generation

5x Phusion HF Buffer	10 μL
10 mM dNTPs	1 μL
Forward primer (10 μM)r	2.5 μL
Reverse primer (10 μM)	2.5 μL

Template DNA	1-10 pg
DMSO	1.5 µL
Phusion DNA Polymerase	0.5 µL
Water	Add to 50 µL

PCR reaction thermocycler program for 1. PCR: megaprimer generation

1.	98 °C	10 minutes
2.	98 °C	30 seconds
3.	Calculated T_a for primer pair (NEB calculator)	30 seconds
4.	72 °C	30 seconds / kilobase
5.	Go to Step 2 (25-30x)	
6.	72 °C	7 minutes
7.	10 °C	Hold

PCR reaction mixture (per 50 µL) for 2. PCR: whole plasmid synthesis

5x Phusion HF Buffer	10 µL
10 mM dNTPs	1 µL
Megaprimer	100 ng
Target vector	20 ng
DMSO	1.5 µL
Phusion DNA Polymerase	0.5 µL
Water	Add to 50 µL

PCR reaction thermocycler program for 2. PCR: whole plasmid synthesis

1.	98 °C	10 minutes
2.	98 °C	30 seconds
3.	60 °C	1 minute
4.	72 °C	5 minutes
5.	Go to Step 2 (40x)	
6.	72 °C	7 minutes
7.	10 °C	Hold

3.2.2 Agarose gel electrophoresis

DNA analysis was routinely performed by agarose gel electrophoresis, using 1 % (w/v) agarose gels prepared with 1x TAE buffer:

DNA loading dye (5x)	Tris/HCl, pH 8.2	10 mM
	EDTA	1 mM
	Glycerol	50 % (v/v)
	Xylene cyanol	0.25 % (w/v)
	Bromphenol blue	0.25 % (w/v)
TAE buffer (50x)	Tris/acetate, pH 8.2	2 M
	EDTA	100 mM

After electrophoresis (~30 minutes, 120 V), gels were stained for 20 minutes with 1 mg / mL ethidium bromide. Band visualization was performed at a wavelength of 360 nm.

3.2.3 DNA isolation and PCR clean-up

DNA plamids were isolated from transformed *E. coli* cells using the peqGOLD Plasmid Miniprep Kit (Peqlab, Germany). PCR generated DNA fragments were isolated using the peqGOLD Cycle-Pure Kit (Peqlab, Germany).

3.2.4 SDS-PAGE analysis

Protein sample purity was routinely assessed with denaturing SDS-PAGE analysis. Both 12 % and 15 % (w/v) acrylamide gels were prepared.

Buffer composition for four gels

Separating gel	Separation buffer	5 mL
	0.4 % SDS (w/v)	
	1.5 M Tris/HCl pH 8.8	
	Acrylamide (40%)	12 % gel: 6 mL
		15 % gel: 7.5 mL

	APS (10%)	100 µL
	TEMED	10 µL
	Water	12 % gel: 9 mL
		15 % gel: 7.5 mL
Stacking gel	Stacking buffer	5 mL
	0.4 %SDS (w/v)	
	0.5 M Tris/HCl pH 6.8	
	Acrylamide (40%)	1 mL
	APS (10%)	100 µL
	TEMED	10 µL
	Water	4 mL
Electrophoresis buffer (10x)	Glycin	1 M
	SDS	1 % (w/v)
	Tris	0.25 M
SDS sample buffer (5x)	Tris/HCl, pH 6.8	60 mM
	Glycerol	30 % (v/v)
	Saccharose	10 % (w/v)
	SDS	5 % (w/v)
	2-mercaptoethanol	3 % (v/v)
	Bromphenol blue	0.02 % (w/v)
Coomassie staining solution (1L)	Coomassie Brilliant Blue G-250	80 mg
	HCl (37 %)	3 mL

Electrophoresis was carried out in 1x electrophoresis buffer at a constant current of 45 mA per gel for 45 minutes. Afterwards gels were first boiled in water and then covered in Coomassie staining solution, boiled again and then gently rocked on an orbital shaker for 20 minutes prior to analysis. For better contrast, gels were left in water overnight.

3.2.5 Determination of protein concentration

Protein concentrations were routinely determined spectrophotometrically (Lambert-Beer's rule) at an absorption wavelength of 280 nm, considering each protein's molecular weight and molar extinction coefficient (www. https://web.expasy.org/protparam).

3.3   Recombinant toxin expression and purification

The ORFs encoding *Y. enterocolitica* orthologues YaxA and YaxB (YE1984, Gene ID 4715532 and YE1985, Gene ID 4715533, respectively) were amplified from total cDNA of *Y. enterocolitica* serovar 8, biovar 1 (ATCC 23715). The ORF for *P. luminescens* orthologue PaxB (NCBI accession number WP_046395991) was synthesized by Eurofins Genomics (Germany). YaxA was cloned as N-terminal His$_6$-SUMO fusion into a pRSET-A vector, YaxB and PaxB as N-terminal His$_6$-fusions into the same vector containing a TEV cleavage site. All constructs and mutants used in this study were generated by restriction-free cloning, following the general protocol of Unger et al.[7]

YaxA was expressed in SoluBL21 (DE3) *E.coli* cells (amsbio) grown at 20 °C in 2xTY medium overnight following induction with 0.5 mM IPTG. YaxB and PaxB were expressed in the BL21 (DE3) strain under the same culture conditions. Selenomethionine substituted protein was produced by the methionine feed-back inhibition method[8] in M9 minimal medium under otherwise identical culture and expression conditions.

Purification of YaxA, YaxB and PaxB was carried out according to the identical protocol. Cell pellets were resuspended in lysis buffer (50 mM Tris-HCl pH 8.0, 300 mM NaCl, 1 mM PMSF, 1 µg/mL DNase I, 0.2 mg/mL lysozyme) and broken by sonication. Clarified lysate was loaded onto a 5 mL Talon cobalt affinity column (GE Healthcare) equilibrated with buffer A (50 mM Tris-HCl pH 8.0, 300 mM NaCl, 10 mM imidazole) and bound protein eluted in one step with buffer B (50 mM Tris-HCl pH 8.0, 300 mM NaCl, 100 mM imidazole). Pooled eluates were dialyzed overnight at 4 °C against buffer C (20 mM HEPES pH 7.0, 25 mM NaCl) in presence of either SUMO protease (YaxA) or TEV protease (YaxB, PaxB). Next, samples were bound to a 6 mL Resource Q column

(GE Healthcare) equilibrated in buffer C and eluted within a linear salt gradient from 25 mM to 1 M NaCl. Peak fractions were further purified on a Superdex 75 16/60 gel filtration column (GE Healthcare) running with buffer D (25 mM HEPES pH 7.0, 150 mM NaCl). Proteins were concentrated to 10-15 mg/mL using 30 kDa MW cut-off centrifugal concentrators (Sartorius) and flash frozen in liquid nitrogen for storage. Purification of selenomethionine derivatized protein followed the same strategy, except for the addition of 2 mM DTT to all buffers.

3.4   Protein crystallization

Native and selenomethionine substituted YaxA (2 mg/mL) were crystallized using the sitting-drop vapor diffusion method in 0.2 M lithium chloride, 37-40 % 2-methyl-2,4-pentanediol, at 4 °C. 0.2 μL of protein solution were mixed with 0.2 μL reservoir solution. Crystals were harvested and plunged directly into liquid nitrogen for storage.

Both YaxB and PaxB required prior reductive lysine methylation[9] before crystals could be obtained. Methylated YaxB (14 mg/mL) was crystallized in the hanging-drop vapor diffusion set-up at 20 °C. 2 μL of protein was mixed with 2 μL reservoir solution containing 1.2 M sodium/potassium phosphate. Reservoir solution supplemented with ~ 4 M sodium malonate[10] was used as cryoprotectant prior to plunging into liquid nitrogen.

Methylated PaxB yielded sizable crystals only following several rounds of streak seeding in the presence of sodium thiocyanate (NaSCN) as a critical additive. Crystals were grown in hanging-drop set-up at 20 °C by mixing 2 μL methylated protein (20 mg/mL) with 2 μL reservoir solution containing 0.2 M magnesium chloride, 0.1 M Bis-Tris pH 5.5, 23-25 % PEG 3350, 0.2 M NaSCN. Selenomethionine derivatized crystals were produced by streak seeding native crystal seeds into drops containing derivatized protein. Reservoir solution supplemented with 20 % (w/v) 2,5-hexanediol was used as cryoprotectant.

3.5   X-ray data collection and structure determination

Diffraction data were collected on beamline X06SA at the Swiss Light Source (Paul Scherrer Institute, Villigen, Switzerland) using a wavelength of 1 Å for all native crystals. Indexing and data reduction were performed with XDS and XSCALE[6] (see Supplementary Table S1 for statistics).

Experimental phases for YaxA were obtained by single-wavelength anomalous dispersion (SAD) methods using a single crystal of selenomethionine derivatized YaxA and a wavelength of 0.979 Å. A total of 500 degrees of data were collected, yielding an anomalous dataset to 2.8 Å resolution. SHELXD[11] (run within HKL2MAP[12]) identified seven sites and a first electron density map was calculated with SHELXE, in which helical features were clearly visible. Using *phenix.find_helices_strands*, implemented through the PHENIX GUI[4], helical densities were fit with poly-alanine models to approximately 50 % of all residues. Heavy atom sites were polished including the built model in a Phaser MR-SAD[13] routine. Performing density modification in RESOLVE[14] and aided by Phaser LLG maps[15] to visualize selenomethionine positions, the amino acid sequence was gradually traced. Iterative rounds of secondary structure- and experimental phase restrained refinement in *phenix.refine,* with manual rebuilding in Coot[1], finally yielded a model encompassing ~80 % of all residues. At this stage, we incorporated near isomorphous native data to 1.8 Å resolution in model refinement. Translation-liberation-screw (TLS) and individual B-factor refinement finally yielded a complete model with converging R_{work}/R_{free} of 19.0 %/22.8 % and promising bond- and angle RMSDs. Validation with MolProbity[16] confirmed excellent model stereochemistry with no Ramachandran plot outliers.

Phases for PaxB were also obtained by SAD methods using selenomethionine derivatized crystals. Reflections were recorded at a wavelength of 0.978 Å to 2.9 Å resolution. 14 initial selenium sites were found in PHENIX AutoSol[17] and subsequent density modification adopting the 4-fold non-crystallographic symmetry (NCS) operators produced a readily interpretable map dominated by alpha-helical features. An initial model of poly-alanine α-helices was produced using *phenix.find_helices_strands*, automatically placing ~60 % of all C_α residues of the four-copy asymmetric unit. This model served to refine the selenium sites using Phaser MR-SAD,

iteratively improving the map and allowing for sequence tracing during rounds of model rebuilding in Coot. The model was refined with NCS-, secondary structure- and experimental phase restraints in *phenix.refine*. Once the majority of sequence was traced, the model was further refined against the native, near-isomorphous dataset at 2.8 Å. NCS restraints were enabled and finally released once it became clear that residues 188-245 showed marked flexibility within the individual subunits, with density missing in significant portions of this region for one of the four NCS copies. REFMAC 5[18] was used in the last stages of model refinement, yielding R_{work}/R_{free} values of 24.1 %/26.8 % and overall good stereochemistry across the four copies in the asymmetric unit, with 0.2 % Ramachandran outliers remaining in the model.

The native YaxB dataset was recorded at 4 Å resolution and phased by molecular replacement on the PaxB crystal structure (Chain A). Homology modeling was performed with MODELLER[19] interfaced through UCSF Chimera[5] and the obtained coordinates applied for Patterson search calculations in Phaser. Though appropriate rotation solutions were achieved, the full-length model was unable to be positioned in its translation, which was due to residues 188-245. Subsequently, these residues were removed from the search model, resulting in a single strong solution, with one copy of YaxB in the asymmetric unit. Following initial rigid-body minimization in *phenix.refine*, DEN refinement[20] in PHENIX was implemented to account for re-orientation of the coiled-coil stalk relative to the original PaxB coordinates. Further TLS and grouped B-factor refinement in REFMAC resulted in converging R_{work}/R_{free} of 32.1 %/33.9 % with excellent model stereochemistry. Due to missing density, residues 188-245 remain un-modelled.

3.6   Reconstitution and purification of YaxAB pores from human erythrocyte membranes

Expired and defibrillated human erythrocytes (purchased from the Blutspendedienst des Bayerischen Roten Kreuzes) were lysed hypotonically in 40 volumes of deionized water and pelleted by centrifugation (5000 x g, 10 minutes). The procedure was repeated four times to obtain washed erythrocyte ghosts, which were frozen and stored as 200 mg/mL aliquots.

Pore reconstitution begun typically by incubating 2 mg of YaxA with 200 mg of erythrocyte ghosts and incubation for 30 minutes at room temperature with gentle rotation. YaxB was added in 1.5-fold molar excess to YaxA and the mixture was incubated for another 30 minutes. Membranes were pelleted by centrifugation (5000 x g, 5 minutes) and resuspended in 15 mL buffer D (25 mM HEPES pH 7.0, 150 mM NaCl). The wash was repeated five times to remove soluble, unbound protein. For detergent extraction of reconstituted pores, YaxAB enriched membranes were resuspended in 1 mL solubilization buffer (25 mM HEPES pH 7.0, 150 mM NaCl, 1.5 % w/v Cymal-6) per 100 mg membranes and rotated gently for 30 minutes at 4°C. Insoluble material was removed by ultracentrifugation (100,000 x g, 30 minutes) and the supernatant concentrated with a 100 kDa MW cut-off centrifugal concentrator. The sample was injected onto a Superose 6 10/30 gel filtration column (GE Healthcare) running with buffer E (25 mM HEPES pH 7.0, 150 mM NaCl, 0.05 % w/v Cymal-6). YaxAB eluted in the first peak of the chromatogram shortly after the column void volume (between 9-10 mL elution volume). Fractions from this peak were pooled, concentrated and 200 µL applied onto a 3.8 mL 10-40 % w/v sucrose gradient (25 mM HEPES pH 7.0, 150 mM NaCl, 0.05 % w/v Cymal-6, 10 -40 % w/v sucrose). Centrifugation was performed at 100,000 x g for 18 hours at 4 °C. 200 µL fractions were taken from top to bottom of the gradient and those containing YaxAB desalted in buffer E using a 5 mL HiTrap Desalting column (GE Healthcare).

3.7 Negative-stain EM data acquisition and image processing

Membrane-extracted YaxAB pores at 0.1 mg/mL were applied to freshly glow-discharged Formvar-supported carbon-coated Cu400 TEM grids (Science Services, Munich) and stained using a 2 % aqueous uranyl formate solution containing 25 mM NaOH (sample incubation 30-60 seconds, staining 30 seconds). Images were acquired at 30,000-fold magnification on a Tecnai Spirit (FEI) operated at 120 kV using either Eagle 4K (FEI) or TVIPS F416 detectors (Tietz Camera Systems). Automated particle picking and 2D classification were performed using Xmipp 3.0[21]. Based on the 2D averages, 14,600 particles were selected and imported into RELION[22]. Using IMAGIC[23] the initial model for the negative stain 3D reconstruction was generated from

three 2D averages assuming either 10-fold, 11-fold or 12-fold rotational symmetry. Individual 3D classification runs using either of the constructed initial models always produced classes with 11-fold symmetry.

3.8   Preparation of the detergent-treated YaxAB complex for cryo-EM

Typically, 1 mg each of YaxA and YaxB were combined and incubated at room temperature for 30 minutes. Cymal-6 was added to 1.5 % (w/v) and the mixture incubated at 4 °C for 30 minutes, after which it was injected onto a Superose 6 column running in buffer E (25 mM HEPES pH 7.0, 150 mM NaCl, 0.05 % w/v Cymal-6). Peak fractions were pooled and 3 mg of amphipol A8-35 were (Anatrace) added. The complex was left to incubate for 4 hours at 4 °C, after which 20 mg of Bio-Beads (Bio-Rad) were added over night at 4 °C. The next day, amphipol exchanged protein was separated on a Superose 6 column running in detergent free buffer D (25 mM HEPES pH 7.0, 150 mM NaCl) and used immediately for cryo-EM.

3.9   Cryo-EM: sample vitrification and data acquisition

Grids for cryo-EM measurements were prepared using a FEI Vitrobot. 4 μL of YaxAB, prepared by detergent treatment and amphipol exchange, at a concentration of 2 mg/mL, was applied onto glow-discharged C-flat 2/1 grids. Prior to vitrification, fluorinated Fos-Choline-8 (Anatrace) was added to the sample in concentrations up to 3 mM to improve the particle orientation distribution. The grids were blotted for 3 to 4 seconds by two blotting papers with an offset of -1 to -2 mm at 100 % humidity and then plunged into liquid ethane cooled with liquid nitrogen. In total, three datasets were collected on a Titan Krios (FEI) electron microscope operating at an acceleration voltage of 300 kV. Images were acquired with a Falcon-III detector (FEI) in linear mode, at a magnification of 59,000, corresponding to a magnified pixel size of 1.106 Å/pixel. During each exposure, 13 frames were collected with a total dose of ~60 e$^-$/ Å^2 and a total

exposure time of 1 second. A total of 4,859 images were automatically acquired using EPU (FEI), with a defocus of -2 μm.

3.10 Cryo-EM: image processing

The image processing workflow was performed with RELION 2.1[24]. Image stacks were motion corrected with the program MotionCor2, after which the contrast transfer function (CTF) values were estimated and corrected using Kai Zhang's Gctf. 1,009 particles were manually picked to create templates for autopicking. 178,149 particles were automatically selected and sorted through four runs of 2D classification. 113,613 particles were chosen for a run of unsupervised 3D classification, using our negative-stain reconstruction as initial reference. Only the class composed of 10 radial spokes was considered (24,822 particles) and further refined imposing C10 symmetry. After movie refinement and particle polishing, the particles were again refined. Since the reconstructed map had the wrong handedness, apparent by the unusual left-handed coil-coil density, the refined map was flipped and finally post processed. The final reconstruction used for model building had a resolution of 6.1 Å according to the Fourier Shell Correlation (FSC) = 0.143 criterion. For validation, the final 3D map was projected in two dimensions for comparison with the experimental 2D class averages using EMAN2[25], imposing C10 symmetry and using 5° rotational steps. FSC between the model and the final map was computed using an online tool based on EMAN2 (https://www.ebi.ac.uk/pdbe/emdb/validation/fsc/), which revealed an agreement between map and model up to a resolution of 6.6 Å (FSC = 0.5).

3.11 Modelling the YaxAB pore into the cryo-EM density

Given the good quality of our cryo-EM map, unambiguous assignment of YaxA and YaxB densities in the map was straightforward. A full model of YaxB was obtained with the Phyre2 One-to-one threading service[26] based on the complete model of PaxB (chain A). YaxA and YaxB were first placed by rigid fitting of the monomers into the density map using Coot, whereby the head

domain helices of both proteins could be positioned unambiguously. Further implementation of Jiggle Fit and Morphing in Coot placed the coiled-coils inside the helical densities, highlighting that the foot domain of YaxB needed to major remodeling. Strikingly, the connectivity of the map was clear in almost all regions and bulky side chain densities for tryptophan, phenylalanine, tyrosine, arginine and lysine were visible in several instances. This allowed confidence in assigning the amino acid register of our pore model, by implementing our refined high-resolution crystal structures. The model was subjected to several rounds of geometry and B-factor refinement in *phenix.real_space_refine*, including secondary structure and NCS restraints. The final model includes YaxA residues 45-153 and 169-410, and YaxB residues 12-343. Analysis of pore diameter was performed with the program HOLE[3].

3.12 Generation of figures

All figures pertaining to protein structure and electron densities were generated and rendered in UCSF Chimera[5]. Figures were arranged and labelled using CorelDRAW X8 (Corel Corporation, USA).

3.13 Liposome floatation assays

Liposomes from bovine heart lipid extract (Avanti Polar Lipids) were prepared by extrusion through 0.1 μm membranes using a mini extruding device (Avanti Polar Lipids) in buffer D (25 mM HEPES pH 7.0, 150 mM NaCl), following the manufacturer's instructions. For the liposome floatation assay, 10 μg of protein was added to ~300 μg of liposomes and incubated for 20 minutes at 37°C. Addition of the second protein (or buffer D, for single protein samples) was carried out and the sample was incubated for another 20 minutes at 37°C. Next, 55 % (w/v) sucrose in buffer D was added to the protein/liposome mixture, to a final volume of 800 μL and transferred to open ultracentrifugation tubes (Beckman Coulter). These were carefully overlaid with 2.8 mL 40 % sucrose (w/v) in buffer D and finally with 400 μL buffer D. The samples were

spun at 55,000 x rpm in a Beckman Coulter SW 55 Ti rotor at 4°C for four hours. 100 µL were fractioned six times from the top of the gradient, then 2.8 mL removed and six fractions of 100 µL taken from the bottom of the gradient. Fractions were mixed with Laemmli buffer and analysed by SDS-PAGE and Coomassie staining.

3.14   Erythrocyte membrane co-sedimentation assay

10 mg of hemoglobin depleted erythrocyte membranes (ghosts) were pelleted by centrifugation (5000 x g, 5 minutes) and resuspended in 20 µL of protein at 0.3 mg/mL. After incubation for 20 minutes at 37 °C, 20 µL of the second protein was added at 0.3 mg/mL and incubated for another 20 minutes. The membranes were centrifuged and washed four times in 1 mL of buffer D (25 mM HEPES pH 7.0, 150 mM NaCl). The final membrane pellet was analyzed by SDS-PAGE following resuspension in 20 µL Laemmli buffer including 2 % (w/v) SDS and 100 mM β-mercaptoethanol.

3.15   Hemolysis assays

Hemoglobin release upon cytolysis was used to measure hemolytic activity of wild type (WT) and mutant toxins. Defibrillated human erythrocytes were washed extensively in PBS (Sigma Aldrich) and collected by centrifugation (1000 x g, 5 minutes). A 2.5 % (w/v) suspension was made in PBS and 100 µL dispensed in 96-well format. Erythrocytes were primed with serial dilutions of YaxA and incubated at 37 °C for 20 minutes. Subsequently, 100 µL of YaxB (2 µM) in PBS were added and plates incubated for another 20 minutes. After centrifugation (300 x g, 5 minutes) 20 µL of supernatant was diluted into 180 µL of PBS in a new 96-well plate. Absorption at 413 nm was measured and normalized to PBS and 1 % (w/v) Triton X-100 values for 0 % and 100 % hemolysis, respectively. Data points from three biological replicates were plotted using GraphPad Prism software and fitted with a variable-slope dose-response curve.

For hemolysis assays using disulfide-locked YaxB foot domain mutants, proteins were oxidized at 1 mg/mL with 100 µM Cu(II):1-10 Phenanthroline at 4 °C overnight. The next day, sample was purified by SEC in buffer D (25 mM HEPES pH 7.0, 150 mM NaCl) on a Superdex75 10/300 column.

3.16 MBP-tag localization and negative-stain analysis

C-terminal maltose-binding protein (MBP) fusions were generated as described in **Section 3.1.x**. Proteins were expressed as described in **Section 3.3** and detergent treatment of 1:1 mixed YaxA (with or without MBP tag) and YaxB (with or without MBP-tag) performed as described in **Section 3.8**. Negative-stain sample preparation, imaging and single-particle analysis were performed essentially as described in **Section 3.7.**

3.17 Crosslinking/mass spectrometry

Cross-linking experiments of the YaxAB complex, extracted and purified from erythrocyte membranes, were performed with the amine-reactive MS-cleavable DSBU-linker[27]. A 5-10 µM solution of the purified protein complex was used. The reaction was conducted in 20 mM HEPES, pH 7.0, 150 mM NaCl, 0.06 % Cymal-6. Freshly prepared stock solution of the DSBU-linker (in DMSO) was added to a final concentration of 7 mM to the protein solution. Cross-linking was conducted for 120 minutes at 4 °C, before the reaction was quenched by adding ammonium bicarbonate to a concentration of 20 mM. Subsequently, the cross-linked YaxAB complex was digested *in-solution* with trypsin according to the manufacturer's protocol (Smart Digest, Thermo Fisher Scientific, 70 °C, 30 minutes). Fractionation of the generated peptide fragments was carried out on an Ultimate 3000 RSLC nano-HPLC system (Thermo Fisher Scientific). Separation of the generated peptide mixtures was performed on an Ultimate 3000 RSLC nano-HPLC system using a 90 minute gradient from 0.1% formic acid (FA) to 35% acetonitrile, 0.08% FA. The nano-HPLC system was directly coupled to the Nanospray Flex Ion Source (Thermo Fisher Scientific) of an Orbitrap Fusion Tribrid mass spectrometer (Thermo Fisher Scientific).

Data were acquired in data-dependent MS/MS mode with higher energy collision-induced dissociation (HCD). Each high-resolution full scan (m/z 300 to 1500, R = 120,000) in the orbitrap was followed by high-resolution product ion scans (R = 15,000) within 5 seconds, starting with the most intense signal in the full scan mass spectrum (isolation window 2 Th). To identify cross-linked products, raw data were converted into *mgf* files using the Proteome Discoverer 2.0 (Thermo Fisher Scientific). Cross-linked products were analyzed with the *in-house* software MeroX 1.6.0[28]. MS and MS/MS data were automatically analyzed, annotated and manually verified.

3.18   Native mass spectrometry

YaxA and YaxB were diluted to 10 uM and then buffer exchanged to 200 mM ammonium acetate, using microbiospin 6 columns (Bio-Rad, Germany). Proteins were then analyzed on a Q-Exactive Plus Orbitrap EMR mass spectrometer (Thermo Fisher Scientific, Germany). An aliquot of 2 μL protein solution was loaded into a gold-coated nano-ESI capillary prepared in-house, as previously described[29] and sprayed into the instrument. The mass spectrometer was operated at positive mode, capillary voltage was set to 1.7 kV and the inlet capillary temperature was set to 180 °C. Trapping gas pressure was set to 1.5 mbar. Spectra were recorded at a resolution of 8750, at minimal energy of 1V in the higher energy collision-induced dissociation cell, and argon was used as collision gas. Spectra are shown with no smoothing.

3.19   Analytical ultracentrifugation

Sedimentation velocity experiments were performed in a Beckman XL-I analytical ultracentrifuge using a UV/VIS optical system at a wavelength of 280 nm. YaxAB samples were diluted to a concentration of 0.2 - 0.5 mg/ml in buffer E, in absence or presence of 0.05 % (w/v) Cymal-6. The sedimentation speed was 25,000 rpm (Ti-50 rotor) at a temperature of 20 °C. Data analysis was performed in Sedfit[30].

3.20   Multiple sequence alignment

Multiple sequence alignment of amino acid sequences was performed with Clustal Omega[31] and graphical display thereof done in ESPript[2].

Bibliography

1. Emsley, P. & Cowtan, K. Coot: model-building tools for molecular graphics. *Acta Crystallogr. D Biol. Crystallogr.* **60,** 2126–2132 (2004).

2. Robert, X. & Gouet, P. Deciphering key features in protein structures with the new ENDscript server. *Nucleic Acids Res.* **42,** W320–W324 (2014).

3. Smart, O. S., Goodfellow, J. M. & Wallace, B. A. The pore dimensions of gramicidin A. *Biophys. J.* **65,** 2455–2460 (1993).

4. Adams, P. D. *et al.* PHENIX: a comprehensive Python-based system for macromolecular structure solution. *Acta Crystallogr. D Biol. Crystallogr.* **66,** 213–221 (2010).

5. Pettersen, E. F. *et al.* UCSF Chimera--a visualization system for exploratory research and analysis. *J. Comput. Chem.* **25,** 1605–1612 (2004).

6. Kabsch, W. Integration, scaling, space-group assignment and post-refinement. *Acta Crystallogr. D Biol. Crystallogr.* **66,** 133–144 (2010).

7. Unger, T., Jacobovitch, Y., Dantes, A., Bernheim, R. & Peleg, Y. Applications of the Restriction Free (RF) cloning procedure for molecular manipulations and protein expression. *J. Struct. Biol.* **172,** 34–44 (2010).

8. Van Duyne, G. D., Standaert, R. F., Karplus, P. A., Schreiber, S. L. & Clardy, J. Atomic structures of the human immunophilin FKBP-12 complexes with FK506 and rapamycin. *J. Mol. Biol.* **229,** 105–124 (1993).

9. Walter, T. S. *et al.* Lysine methylation as a routine rescue strategy for protein crystallization. *Struct. Lond. Engl. 1993* **14,** 1617–1622 (2006).

10. Holyoak, T. *et al.* Malonate: a versatile cryoprotectant and stabilizing solution for salt-grown macromolecular crystals. *Acta Crystallogr. D Biol. Crystallogr.* **59,** 2356–2358 (2003).

11. Sheldrick, G. M. A short history of SHELX. *Acta Crystallogr. A* **64,** 112–122 (2008).

12. Pape, T. & Schneider, T. R. *HKL2MAP*: a graphical user interface for macromolecular phasing with *SHELX* programs. *J. Appl. Crystallogr.* **37,** 843–844 (2004).

13. McCoy, A. J. *et al.* Phaser crystallographic software. *J. Appl. Crystallogr.* **40,** 658–674 (2007).

14. Terwilliger, T. SOLVE and RESOLVE: automated structure solution, density modification and model building. *J. Synchrotron Radiat.* **11,** 49–52 (2004).

15. McCoy, A. J. & Read, R. J. Experimental phasing: best practice and pitfalls. *Acta Crystallogr. D Biol. Crystallogr.* **66,** 458–469 (2010).

16. Chen, V. B. *et al.* MolProbity: all-atom structure validation for macromolecular crystallography. *Acta Crystallogr. D Biol. Crystallogr.* **66,** 12–21 (2010).

17. Terwilliger, T. C. *et al.* Decision-making in structure solution using Bayesian estimates of map quality: the PHENIX AutoSol wizard. *Acta Crystallogr. D Biol. Crystallogr.* **65,** 582–601 (2009).

18. Murshudov, G. N. *et al. REFMAC* 5 for the refinement of macromolecular crystal structures. *Acta Crystallogr. D Biol. Crystallogr.* **67,** 355–367 (2011).

19. Sali, A. & Blundell, T. L. Comparative protein modelling by satisfaction of spatial restraints. *J. Mol. Biol.* **234,** 779–815 (1993).

20. Schröder, G. F., Levitt, M. & Brunger, A. T. Super-resolution biomolecular crystallography with low-resolution data. *Nature* **464,** 1218–1222 (2010).

21. Scheres, S. H. W., Núñez-Ramírez, R., Sorzano, C. O. S., Carazo, J. M. & Marabini, R. Image processing for electron microscopy single-particle analysis using XMIPP. *Nat. Protoc.* **3,** 977–990 (2008).

22. Scheres, S. H. W. RELION: Implementation of a Bayesian approach to cryo-EM structure determination. *J. Struct. Biol.* **180,** 519–530 (2012).

23. van Heel, M., Harauz, G., Orlova, E. V., Schmidt, R. & Schatz, M. A New Generation of the IMAGIC Image Processing System. *J. Struct. Biol.* **116,** 17–24 (1996).

24. Kimanius, D., Forsberg, B. O., Scheres, S. H. & Lindahl, E. Accelerated cryo-EM structure determination with parallelisation using GPUs in RELION-2. *eLife* **5,** (2016).

25. Tang, G. *et al.* EMAN2: An extensible image processing suite for electron microscopy. *J. Struct. Biol.* **157,** 38–46 (2007).

26. Kelley, L. A., Mezulis, S., Yates, C. M., Wass, M. N. & Sternberg, M. J. E. The Phyre2 web portal for protein modeling, prediction and analysis. *Nat. Protoc.* **10,** 845–858 (2015).

27. Müller, M. Q., Dreiocker, F., Ihling, C. H., Schäfer, M. & Sinz, A. Cleavable cross-linker for protein structure analysis: reliable identification of cross-linking products by tandem MS. *Anal. Chem.* **82,** 6958–6968 (2010).

28. Götze, M. *et al.* Automated assignment of MS/MS cleavable cross-links in protein 3D-structure analysis. *J. Am. Soc. Mass Spectrom.* **26,** 83–97 (2015).

29. Kirshenbaum, N., Michaelevski, I. & Sharon, M. Analyzing large protein complexes by structural mass spectrometry. *J. Vis. Exp. JoVE* (2010). doi:10.3791/1954

30. Schuck, P. Size-distribution analysis of macromolecules by sedimentation velocity ultracentrifugation and lamm equation modeling. *Biophys. J.* **78,** 1606–1619 (2000).

31. Sievers, F. *et al.* Fast, scalable generation of high-quality protein multiple sequence alignments using Clustal Omega. *Mol. Syst. Biol.* **7,** 539–539 (2014).

Chapter 4

Results

Several figures including legends in this chapter are published in the following manuscript:

"Structure & mechanism of the two-component α-helical pore-forming toxin YaxAB"

Bastian Bräuning, Eva Bertosin, Florian Praetorius, Christian Ihling, Alexandra Schatt, Agnes Adler, Klaus Richter, Andrea Sinz, Hendrik Dietz, Michael Groll

Nature Communications **9** (1), 1806 (2018); DOI: 10.1038/s41467-018-04139-2

4.1   Statement of contributions

My contributions to the results presented in this chapter are summarized in this section:

- Conception and planning of the project, together with Prof. Michael Groll.
- Establishment of purification protocols for all recombinant proteins and protein complexes.
- Crystallization and structure determination of YaxA, YaxB and PaxB.
- Sample optimization for negative-stain and cryo-electron microscopy (cryo-EM), in collaboration with Dr. Florian Praetorius and Eva Bertosin (group of Prof. Hendrik Dietz, Department of Physics, TUM).
- Building and refinement of the YaxAB pore model into the cryo-EM map.
- Protein biochemical assays and mutagenesis studies.

The following people contributed experimental data and analysis used in some of the figures presented in this chapter:

- Eva Bertosin (**Fig. 4.14a,c; 4.15**): cryo-EM data acquisition and processing
- Dr. Florian Praetorius (**Fig. 4.10; 4.11a,d; 4.12a; 4.13; 4.17a; 4.25b**): negative-stain TEM analysis
- Dr. Christian Ihling, Alexandra Schatt, Prof. Andrea Sinz (**Fig. 4.17b,c**): crosslinking/mass spectrometry
- Dr. Klaus Richter (**4.12b**): analytical ultracentrifugation
- Dr. Gili Ben-Nissan (**Fig. 4.2d**): native mass spectrometry

4.2   Cloning, protein expression and purification

4.2.1 Cloning

Coding sequences for YaxA and YaxB were amplified from *Y. enterocolitica* genomic DNA (**Fig. 4.1**) and inserted as N-terminal His$_6$-SUMO (YaxA) or His$_6$-TEV (YaxB) fusion constructs into the pRSET-A vector, using restriction-free cloning.
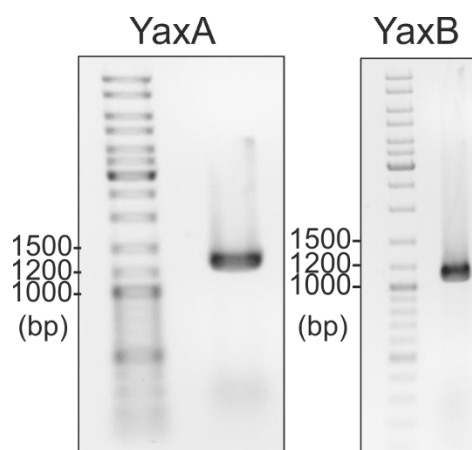
Fig. 4.1 Amplification of YaxA and YaxB coding regions from *Y. enterocolitica* genomic DNA. Shown are 1% (w/v) agarose electrophoresis gels of the PCR reactions. The YaxA and YaxB fragments were amplified using primer pairs pRSET-HT-YaxA-F / pRSET-HT-YaxA-R and pRSET-HT-YaxB-F / pRSET-HT-YaxB-R, respectively.

The coding sequence for PaxB was synthesized by Eurofins Genomics (Ebersberg, Germany) and includes flanking sequences complementary with the target site in the pRSET-A vector, generating the vector pRSET-A-His$_6$ –SUMO-PaxB. All further plasmid manipulations were carried out using restriction-free cloning and the primers listed in **3.1.2** (DNA primer list). Before plasmids were transformed, the correct DNA sequence was ascertained by Sanger sequencing (GATC, Germany).

4.2.2 Protein expression and purification

His$_6$-SUMO-YaxA was expressed in SoluBL21 (DE3) *E. coli* cells, whereas His$_6$-TEV-YaxB and His$_6$-SUMO-PaxB were expressed in BL21 (DE3) cells. Following IPTG induction and overnight

expression at 18 °C, cells were lysed and the cleared lysates loaded onto TALON cobalt affinity chromatography columns.
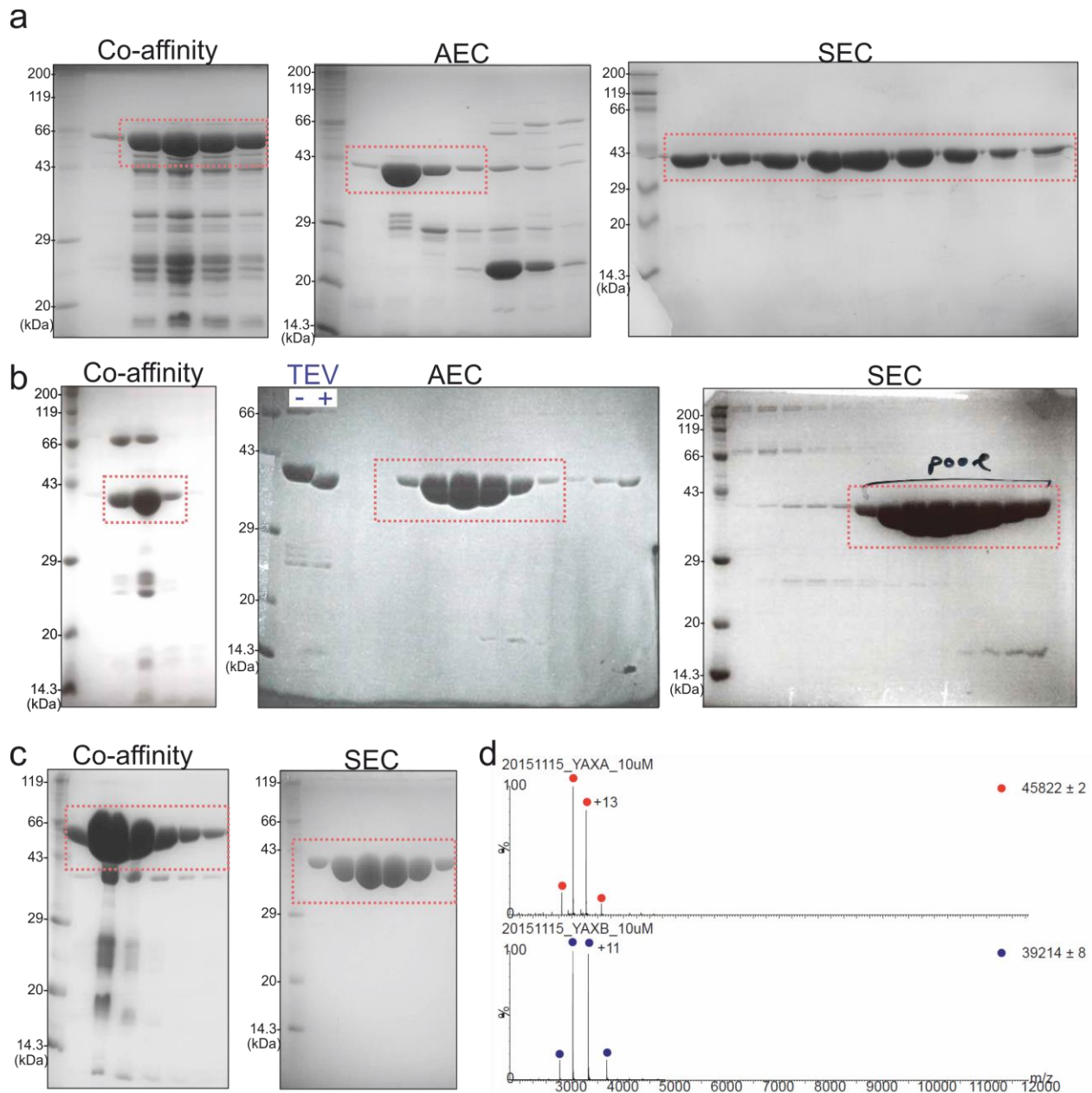
Fig. 4.2 Purification of YaxA, YaxB and PaxB. a) Purification of YaxA by cobalt-affinity chromatography (Co-affinity), anion-exchange chromatography (AEC: Resource Q 6 mL) and size-exclusion chromatography (SEC: Superdex 75). Shown are SDS-PAGE gels stained with Coomassie. Fractions with red dashed boxes were pooled and taken to the next step. b) Purification of YaxB. c) Purification of PaxB. d) Native mass spectrometry analysis of purified YaxA (red) and YaxB (blue), indicating that both toxin subunits are monomers.

After protease treatment overnight and dialysis into low-salt buffers, YaxA and YaxB were further purified by anion-exchange chromatography (Resource Q 6mL). As the final step, all three proteins were purified by size-exclusion chromatography (HiLoad Superdex 75 16/60). **Figure 4.2a-c** summarize each purification step, showing SDS-PAGE analyses for each chromatographic peak of interest. The intact mass and oligomeric state for YaxA and YaxB was determined by native mass spectrometry (**Fig. 4.2d**), indicating monomeric states in each case.

4.3   Protein crystallization and structure determination

4.3.1 Protein crystallization

All proteins were crystallized by the hanging-drop vapor diffusion method (**Fig. 4.3**). YaxB and PaxB required prior reductive lysine methylation before sizable crystals for diffraction analysis could be obtained. For YaxA and PaxB, selenomethionine derivatives for experimental phasing were grown in identical conditions as native proteins.
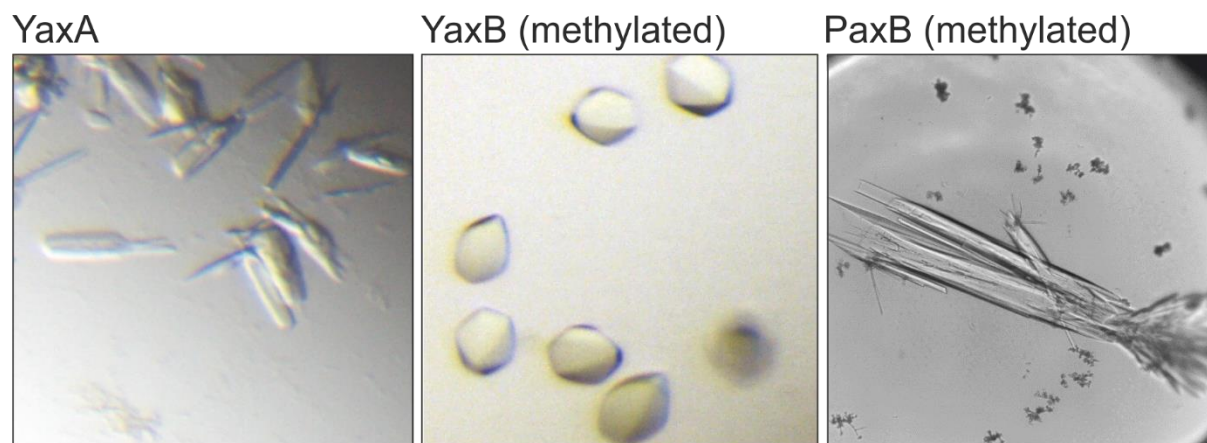
Fig. 4.3 Crystallization of YaxA, YaxB and PaxB. White light images, taken under a stereomicroscope, are shown for representative crystals used for diffraction data collection.

4.3.2 Experimental phasing of YaxA and PaxB by selenium SAD

Native data were collected on YaxA, YaxB and PaxB to 1.8 Å, 4.0 Å and 2.8 Å resolution, respectively, at a wavelength of 1.0 Å. As molecular replacement phasing attempts, using deposited coordinates of ClyA-like α-PFTs failed, experimental phasing was performed. PaxB crystals consistently diffracted to much higher resolution than YaxB. Therefore, single wavelength anomalous dispersion (SAD) experiments were performed with this orthologue. Se-SAD phasing was successful for both YaxA and PaxB selenomethionine derivatives, yielding readily interpretable electron density maps calculated with experimental phases (**Fig. 4.4**). A majority of secondary structural elements could be placed automatically for both YaxA and PaxB, after which backbone and sequence tracing were completed manually. Subsequently, the PaxB coordinates were successfully used to phase the 4.0 Å YaxB dataset by molecular replacement. All three models were refined against native data, to final R_{free} values of 22.8 %, 26.8 % and 33.9 %, for YaxA, PaxB and YaxB, respectively. Electron densities were interpretable for all three proteins, despite increased B-factor distribution in some protein regions (**Fig. 4.5**).

YaxA, Se-SAD, 2.8 Å, 1 copy / AU (SHELXE)
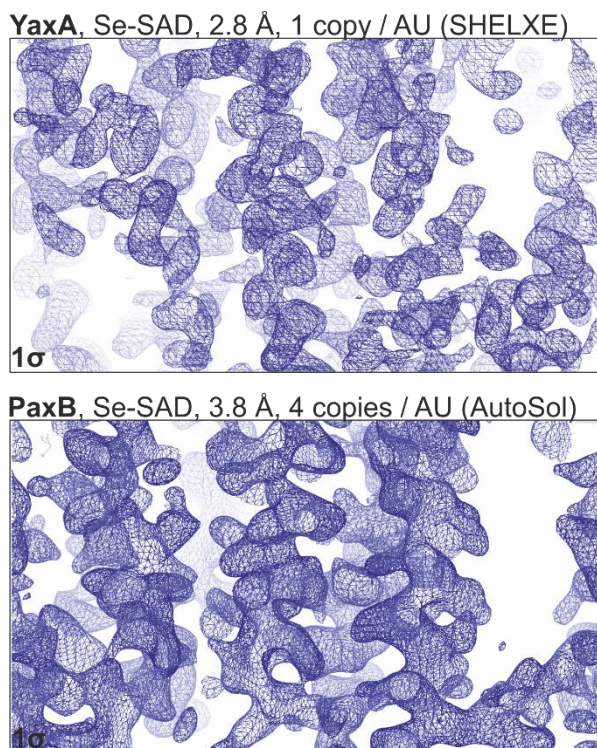
Fig. 4.4 Experimental Se-SAD electron densities for YaxA and PaxB following density modification. Clear helical features are apparent in both cases.

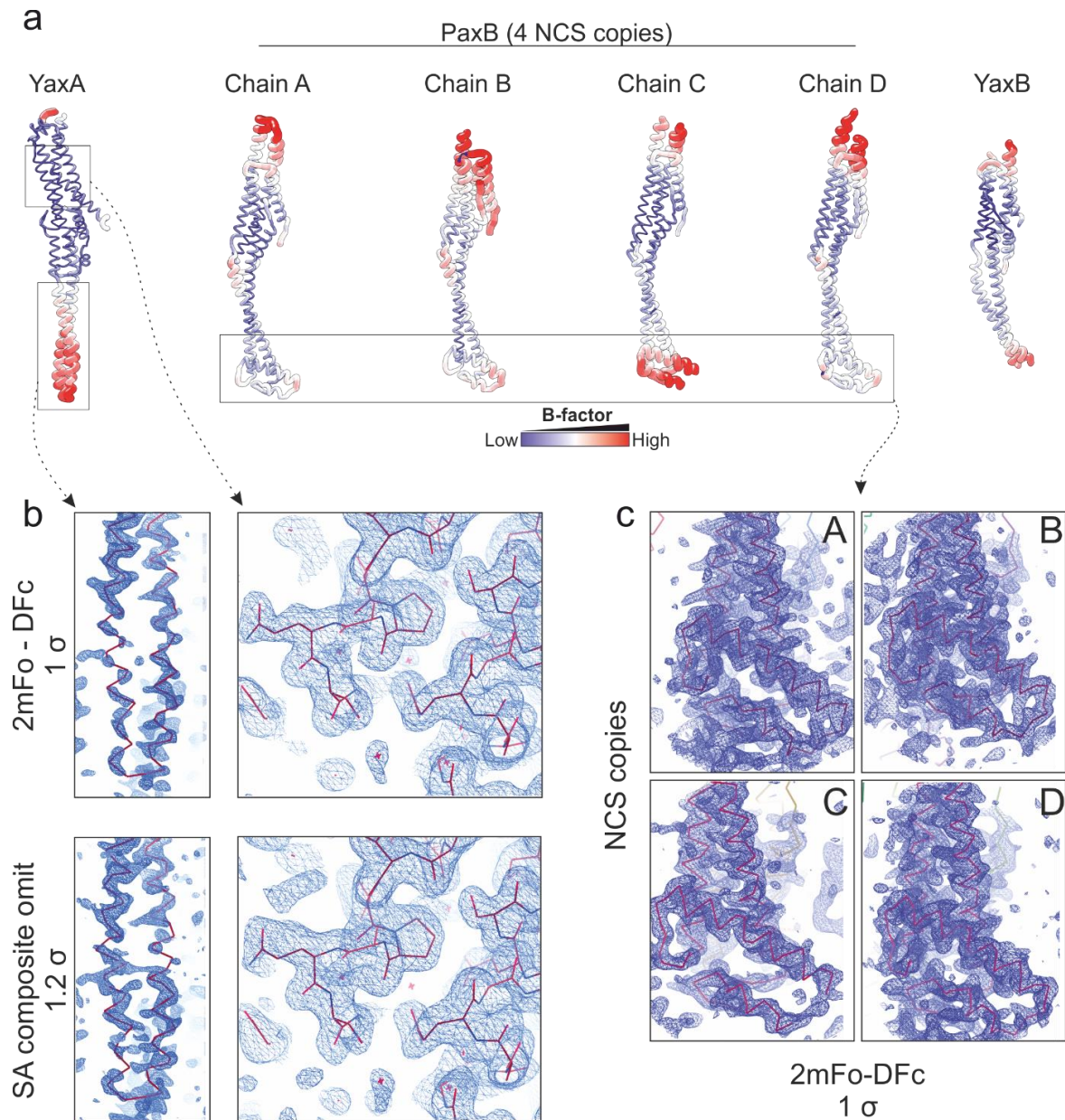**PaxB**, Se-SAD, 3.8 Å, 4 copies / AU (AutoSol)

Fig. 4.5 Crystal structure B-factor distribution and quality of the electron density maps. a) Rendering of YaxA, PaxB and YaxB crystal structures by B-factor values. For PaxB, all four NCS-related copies are presented. b) Electron density quality of two YaxA regions with distinct average B-factor values: the coiled-coil stalk and foot domains (left) and the head domain (right). Shown are three different maps for each region: 2mFo-DFc map (top), simulated-annealing (SA) composite omit 2mFo-DFc map (middle) and feature-enhanced map (bottom). All maps were calculated using PHENIX. c) 2mFo-DFc electron density quality for the foot domain of the four NCS-related PaxB models.

4.4   Crystal structure of YaxA, YaxB and PaxB

Comparing the crystal structures of YaxA, YaxB and PaxB reveals that a five-helix bundle head domain, connecting to a long, two-helix coiled-coil stalk domain, comprises the common structural frame of all three proteins (**Fig. 4.6a,b**). This is striking, since the proteins share only limited sequence identity: YaxA and YaxB are 22 % sequence identical, YaxB and PaxB are 40 % sequence identical. The 4 Å YaxB model lacks defined electron density for the foot domain. Since YaxB and PaxB are true structural homologs (2.1 Å RMSD across 210 C_α pairs; **Fig. 4.7a**), the PaxB model will be used for structural analyses when appropriate.
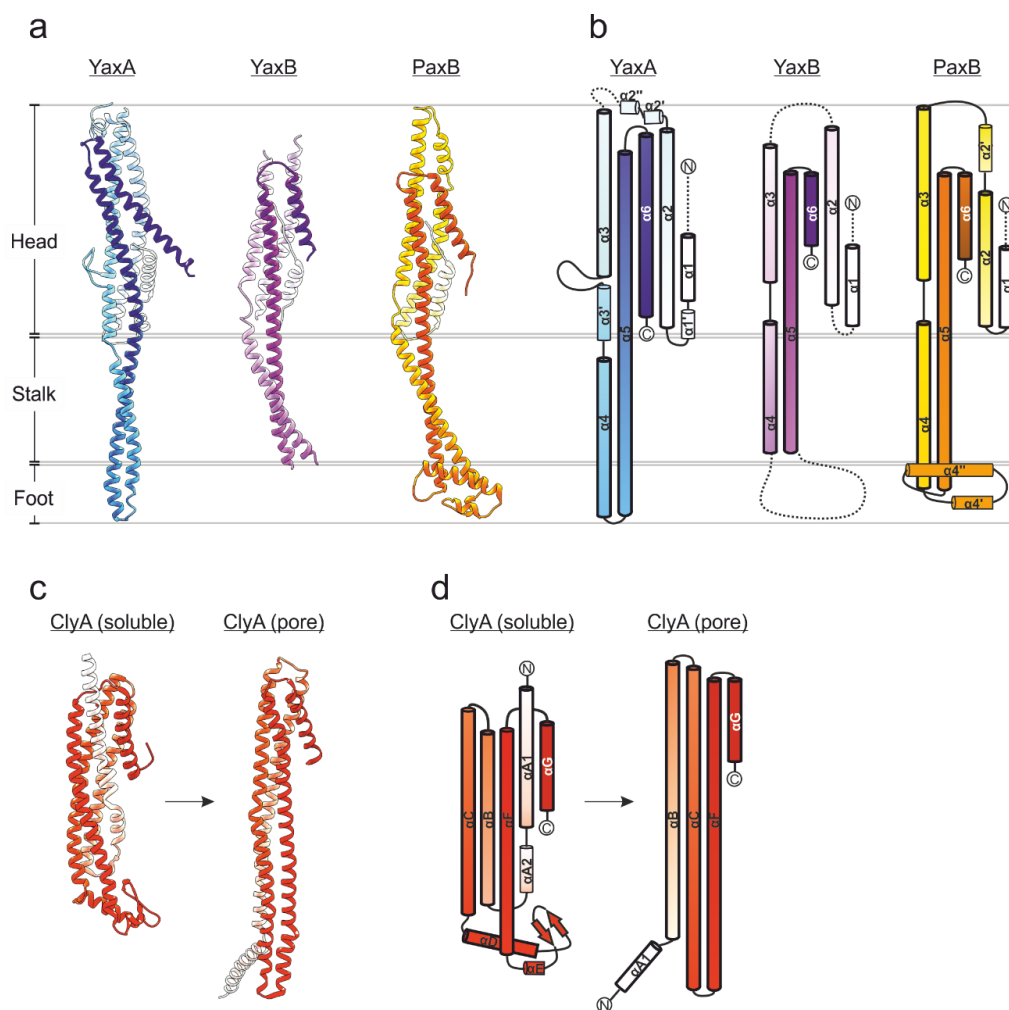
Fig. 4.6 X-ray analysis of YaxA, YaxB and the YaxB orthologue PaxB. a) Crystal structures of YaxA (blue), YaxB (pink) and the YaxB orthologue PaxB (orange). Ribbons are shaded from light (N-terminus) to dark (C-terminus). Lines delineate the approximate boundaries for the three protein domains. b) Topology diagrams of YaxA, YaxB and PaxB colored according to a). α1 - α6 in bold black outline denote the structural frame common to the toxin subunits. Dotted lines emphasize protein regions unresolved in the crystal structures. c) Crystal structures of ClyA in its soluble form (PDB code 1QOY) and as a pore-protomer (PDB code 2WCD). d) Topology diagrams of ClyA in soluble and pore-protomeric states.
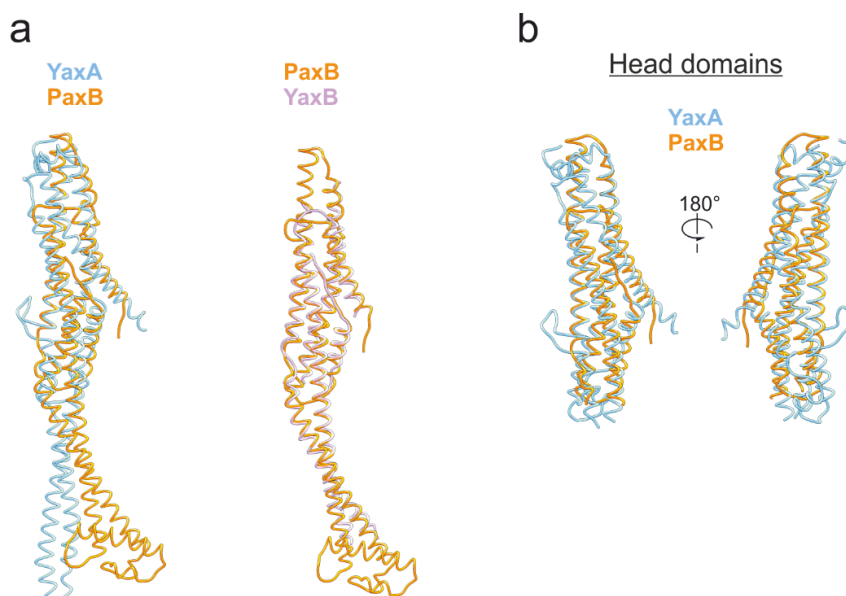
Fig. 4.7 : Overlays of YaxA, YaxB and PaxB. a) Ribbon plots of monomeric YaxA with PaxB (left) and YaxB with PaxB (right). b) Alignment of the YaxA and PaxB head domains.

As evident from a structural superposition, the head domains of YaxA and PaxB superpose well (RMSD of 2.9 Å across 159 C_α pairs; **Fig. 4.7b**). Structurally, the greatest point of distinction between the two toxin subunits lies in the foot domains: here, YaxA features a sharp turn between helices α4 and α5, whereas PaxB forms an additional small domain comprising helices α4' and α4'', which pack against the coiled-coil stalk (**Fig. 4.6a,b**). Notably, this homologous foot domain in YaxB is not resolved in the electron density map.

4.5   Comparison of YaxA and PaxB with known protein structures

In order to find structurally related proteins, the YaxA and PaxB coordinates were queried using the DALI[1] server. The head domains of YaxA and PaxB align well, while the coiled-coil stalk and foot domains differ both in orientation and structure, the head domain coordinates were entered into the search first. The highest scores were found within the wider ClyA family of α-PFTs (**Fig. 4.8a**, **Fig. 4.9a**). For the YaxA head domain, DALI Z-scores ranged from 9.6 (soluble ClyA, 5.5 Å RMSD; PDB code 1QOY[2]) to 12.2 (NheA, 3.4 Å RMSD; PDB code 4K1P[3]). Scores for the PaxB head domain ranged from 7.4 (soluble ClyA, 3.8 Å RMSD) to 13.3 (pore-protomeric ClyA, 2.4 Å RMSD; PDB code 2WCD[4]). ClyA, the founding member of this wider PFT family, has structures available

for both soluble and pore-protomeric states: a to-scale comparison of these structure with YaxA and PaxB/YaxB reveals topological similarities (**Fig. 4.6c,d**). Following apparent secondary structural correspondences can be made when comparing protein topologies: αA1 - α1, αB - α2, αC - α3, αD - α4, αF - α5 and αG - α6 (helix nomenclature for ClyA is adapted from previous work[4]). Despite this topological resemblance, superposition of pore-protomeric ClyA with full-length YaxA and PaxB (protomeric ClyA shows the closest overall resemblance in size and shape) highlights differences in the coiled-coil orientation and the domain character of the foot region (**Fig. 4.8b**, **Fig. 4.9b**). In summary, the head domains of YaxA and YaxB orthologues feature a structural consensus to the wider ClyA family of PFTs, while the coiled-coil stalk and foot domains distinguish from these former proteins.

4.6   Reconstituting a YaxAB pore complex

4.6.1 YaxA and YaxB form large hourglass shaped soluble complexes

As a first step towards reconstitution of a YaxAB pore complex, the interaction between YaxA and YaxB was assessed by analytical size-exclusion chromatography (Superdex 75; **Fig. 4.10**). This revealed that the two proteins form a high-molecular weight (MW) complex, eluting close to the column void volume (Superose 6 column exclusion limit ∼5 MDa). SDS-PAGE analysis of this peak fraction showed an apparent 1:1 ratio of both components, as assessed by band intensities. The peak fraction was analyzed by negative-stain transmission electron microscopy (TEM), revealing hourglass shaped particles that resemble two funnels attached at the base. These insights confirm a previous study performed on the YaxAB orthologue from *X. nematophila*, where direct interaction between the toxin subunits was shown by pull-down assays[5]. Though direct and apparently stoichiometric interaction between YaxA and YaxB could be established, the resulting complex had little resemblance to a membrane-embedded pore. Thus, the reconstitution of YaxAB in target membranes was performed next.
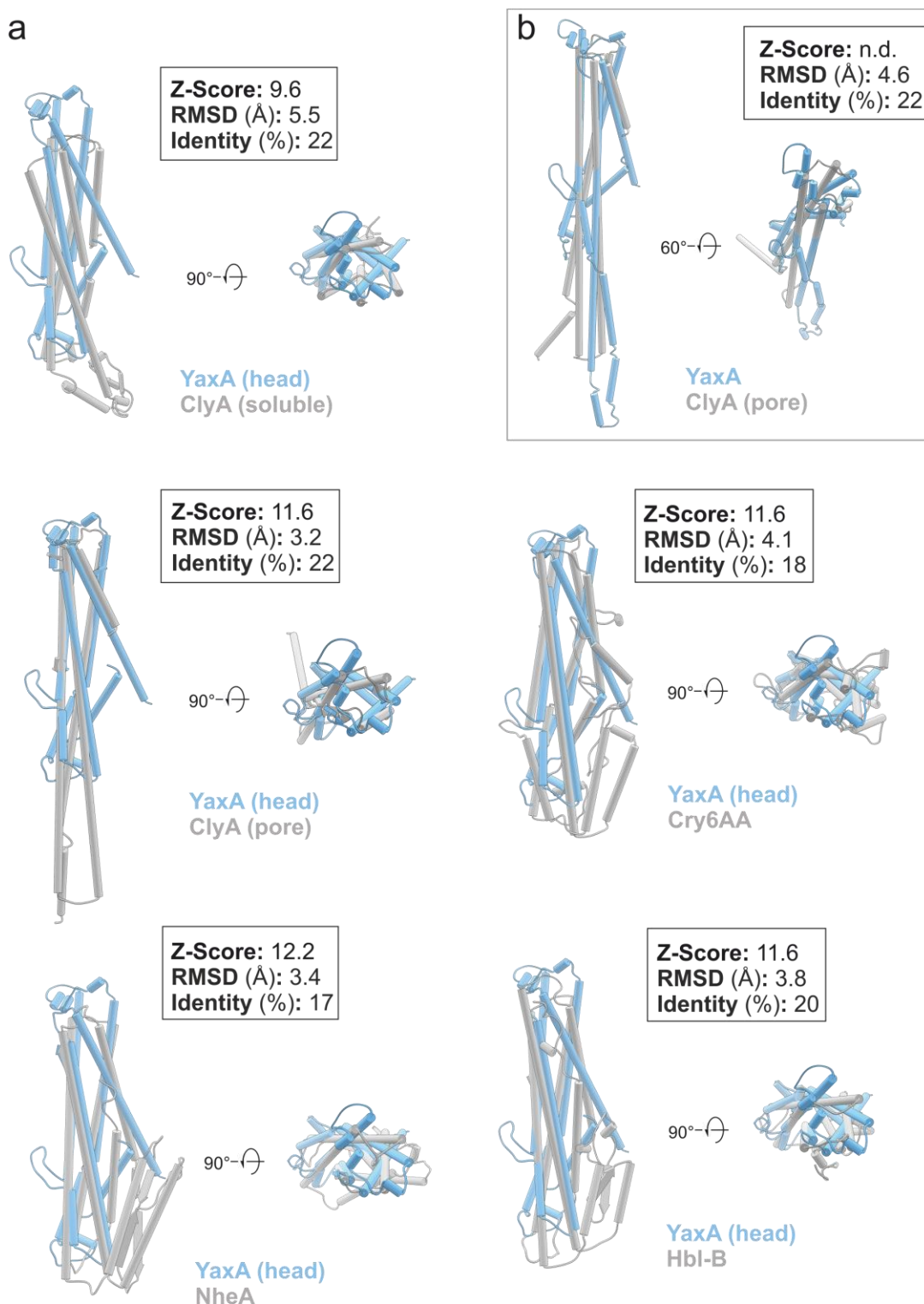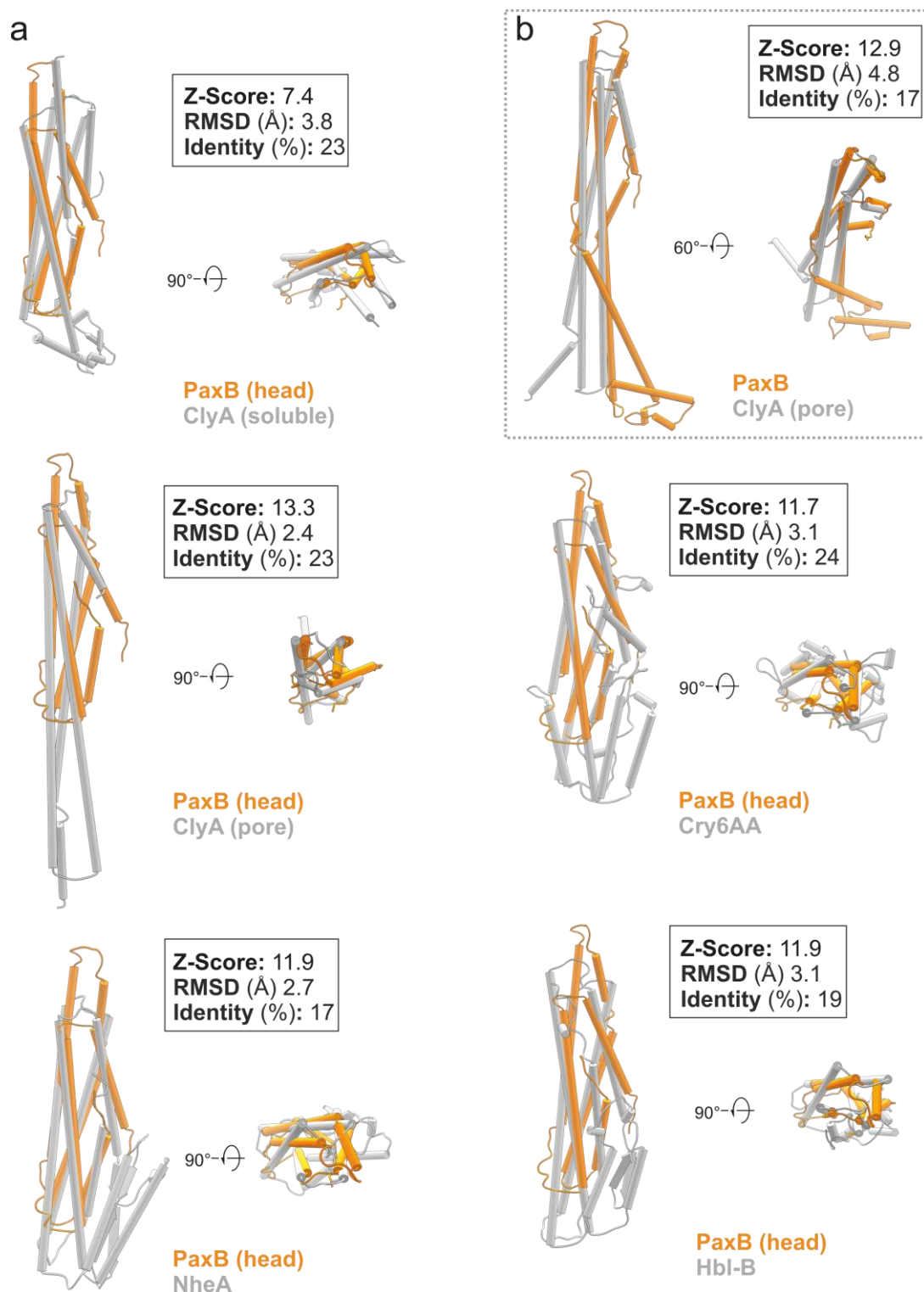
Fig. 4.8 Structural superposition of YaxA with ClyA family toxins. a) DALI analysis and alignment of the YaxA head domain (including residues 45 - 237 and 310 - 410) with various ClyA family toxins. PDB codes for aligned structures: 1QOY (soluble ClyA), 2WCD (pore-protomeric ClyA), 4K1P (NheA), 5KUC (Cry6AA), 2NRJ (Hbl-B). DALI Z-score, RMSD (Å) and sequence identity between aligned pairs are reported for each superposition. b) Superposition of YaxA (full-length) and pore-protomeric ClyA. The proteins were aligned by their head domains according to a). Full-length pore-protomeric ClyA produced no DALI match, despite well-aligning head domains.

Fig. 4.9 Structural superposition of PaxB with ClyA family toxins. a) DALI analysis and alignment of the PaxB head domain (including residues 12 – 153 and 279 – 353) with various ClyA family toxins. b) Superposition of PaxB (full-length) and pore-protomeric ClyA as output by DALI analysis.
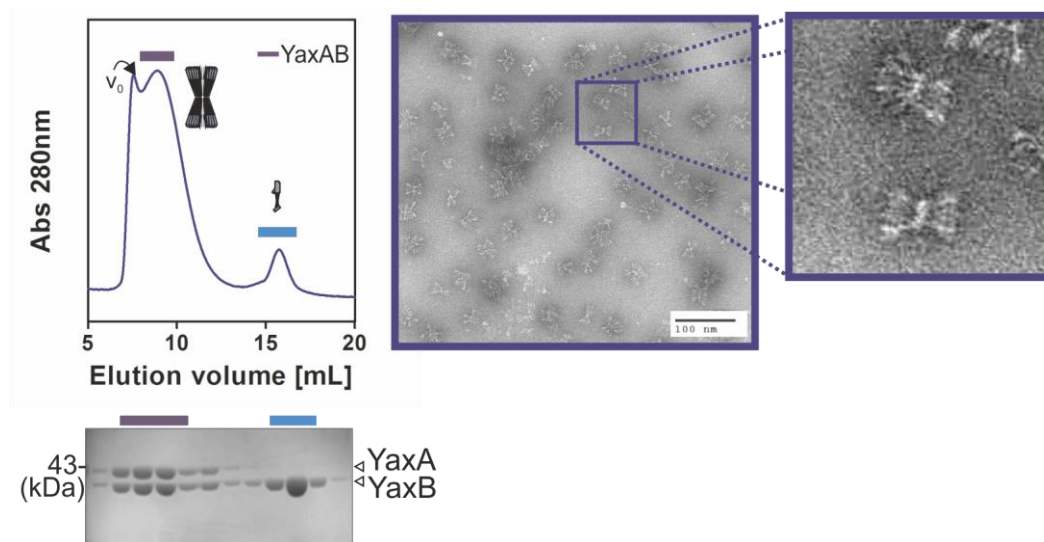
Fig. 4.10 Characterizing a soluble YaxAB complex. YaxA and YaxB were mixed 1:1 at protein concentrations of 1 mg/mL. 500 μL of the sample were injected onto a Superose 6 10/300 column. Peak fractions were analyzed by SDS-PAGE and Coomassie staining, depicted below the chromatogram. Fractions from the high-molecular weight peak, containing both YaxA and YaxB, were subsequently imaged by negative-stain TEM. A representative micrograph is shown to the right.

4.6.2 Low-resolution TEM analysis of the YaxAB pore extracted from membranes

To obtain a membrane-inserted YaxAB pore, YaxA and YaxB were added sequentially to erythrocyte ghosts (depleted of hemoglobin), as previous reports had observed a strict consecutive lytic mode of action for this toxin class *in vitro*[5,6]. Looking at these membranes in negative-stain TEM confirmed densely packed pores on the surface (**Fig. 4.11a**). In order to extract complexes for subsequent structural characterization, a series of mild detergents were tested for their ability to solubilize YaxAB and to produce a defined peak in analytical SEC (Superose 6; **Fig. 4.11b**). Cymal-6 was identified as a suitable detergent and used for a more preparative extraction of pores, followed by SEC (**Fig. 4.11c**). The fractions containing both YaxA and YaxB were identified by SDS-PAGE analysis and used for negative-stain TEM imaging (**Fig. 4.11d**).

Compared with YaxAB mixed in solution (**Fig. 4.10**), detergent extracted and purified YaxAB resulted in single pore complexes no longer aggregated at their base. This suggests that in absence of detergent, YaxAB aggregates most likely by sequestering hydrophobic, membrane active domains. Indeed, treating preformed YaxAB with Cymal-6 - without any reconstitution into membranes – revealed individual pores. Notably, complexes obtained in this way appeared

similar to membrane extracted complexes (**Fig. 4.12a**). Furthermore, YaxAB prepared both via membrane extraction and detergent treatment shared an overlapping population of particles in sedimentation-velocity analytical ultracentrifugation (AUC) experiments (**Fig. 4.12b**). Given this apparent equivalence between the samples prepared by both methods, the simpler approach, of treating the complex with detergent, was utilized to obtain a high-resolution cryo-EM map of the pore (**Section 4.7**).
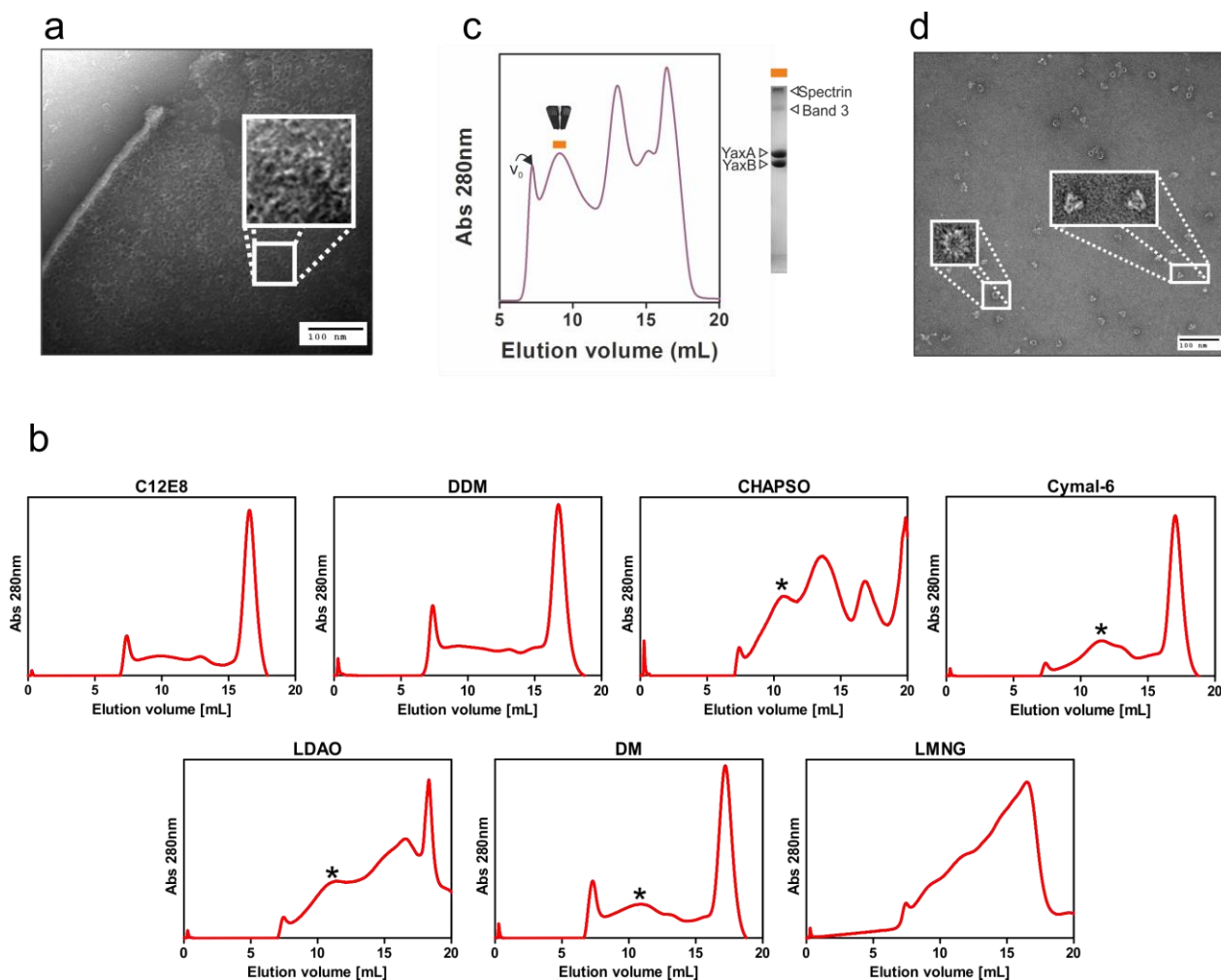

Fig. 4.11 Reconstitution of YaxAB pores on erythrocyte ghosts. a) YaxA and YaxB were added sequentially onto human erythrocyte ghosts and imaged by negative-stain TEM. The membranes were densely covered in pore complexes (enlarged view). b) Screening to find suitable detergents for YaxAB pore extraction. Superose 6 elution profiles are shown. Asteriks mark distinct peaks containing both subunits. c) YaxAB enriched membranes were solubilized with 1 % Cymal-6 and injected onto a Superose 6 gel filtration column. YaxAB eluted in the first peak, which was verified by SDS-PAGE analysis (shown on the right). d) Representative negative-stain TEM micrograph of the purified YaxAB complex.

Initial low-resolution structural data of the pore complex extracted from erythrocyte membranes were obtained by negative-stain TEM. Particle picking was performed automatically from micrographs and subjected to 2D classification, indicating significant heterogeneity in the apparent stoichiometry of pores, ranging from 8 to 12 radial spokes (**Fig. 4.13a**). 3D classification and refinement yielded a map at ~25 Å, bearing apparent C11 symmetry (**Fig. 4.13b**). Despite using initial models with different symmetries for 3D classification, the C11 class appeared to be prominent. Though at low resolution, this map already depicts an upper, spoked rim, from which density converges at a lower, cup-like funnel.
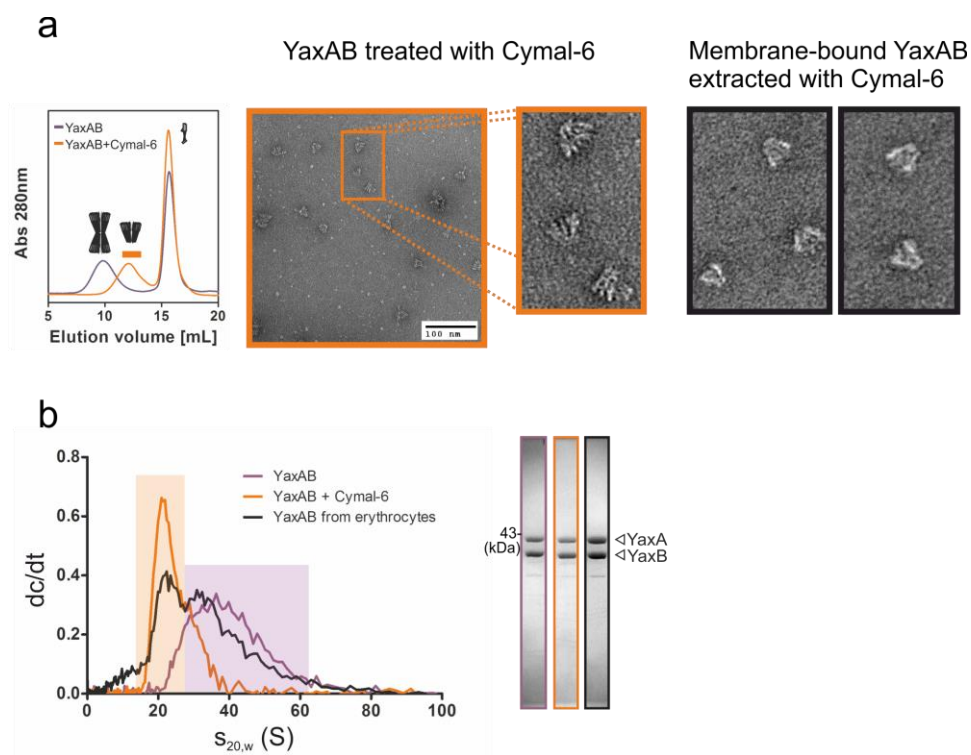

Fig. 4.12 Membrane extracted and detergent treated YaxAB samples are similar. a) Comparative gel filtration profiles between detergent-treated (orange trace) and non-treated (purple) YaxAB complexes (*left*). A representative TEM micrograph each, of detergent-treated (*middle*) and membrane extracted (*right*) complexes, is shown. b) Sedimentation-velocity ultracentrifugation analysis (AUC) of three differently obtained YaxAB complexes (*left*). As indicated by orange and purple boxes, YaxAB partitioned between a ~18-21 S and a diffuse 20-60 S fraction, respectively. Analyzed samples used were proven to contain both subunits (SDS-PAGE, *right*).
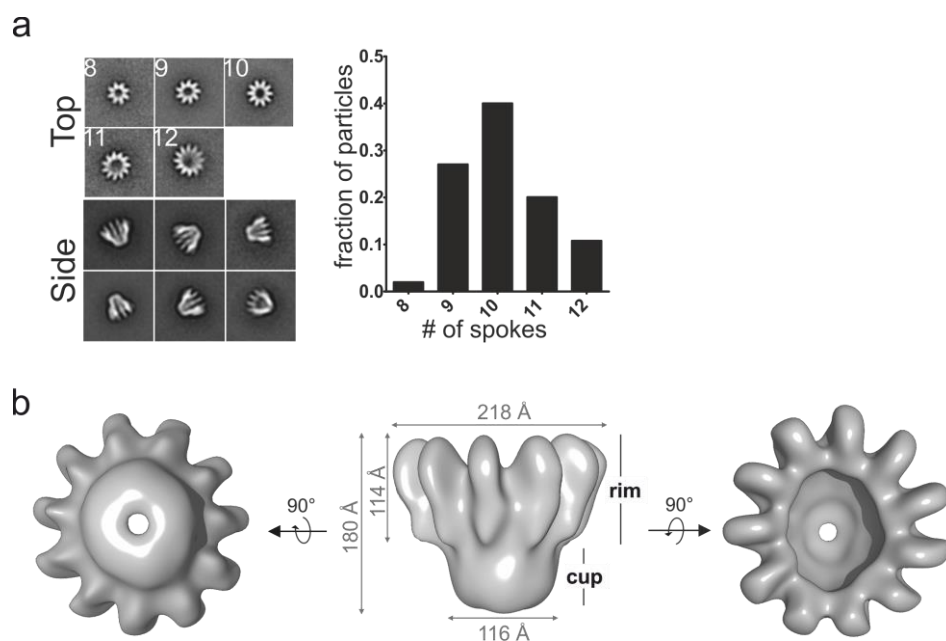
Fig. 4.13 Negative-stain TEM analysis of YaxAB. a) Gallery of top- and side-view 2D class averages of YaxAB (*left*) and the distribution of top-view radial spoke numbers (*right*). b) Three views from a 3D reconstruction of membrane-extracted YaxAB, bearing apparent C11 symmetry.

This reconstruction provided first indication that the YaxAB pores, extracted from erythrocyte ghosts using Cymal-6 detergent, maintain structural integrity upon purification. Importantly, the low-resolution map already unambiguously defines the general architecture and large overall size of the pore. When the strong compositional heterogeneity of YaxAB became apparent, crystallization trials for the complex were abandoned. To obtain higher resolution data – allowing the precise assignment of YaxA and YaxB subunits in the context of the pore – cryo-EM was pursued in the following.

4.7   Cryo-EM analysis of the YaxAB pore

4.7.1 The process of obtaining well-dispersed YaxAB particles in vitreous ice

For cryo-EM analysis, it was important to produce evenly distributed, non-aggregating pore samples in vitreous ice. Cryo-EM grids containing YaxAB, purified by SEC in buffer containing the detergent Cymal-6, displayed particles which were heavily aggregated and thus not suitable for automatic particle picking (**Fig. 4.14a**, *top*). Encouraged by previous studies reporting the successful use of amphipol surfactants, instead of detergent, for obtaining monodisperse membrane protein samples in vitreous ice[7,8], detergent in the YaxAB sample was exchanged to amphipol A8-35. To this end, detergent treated YaxAB was incubated with A8-35 and hydrophobic affinity resin (Bio-Beads) overnight to promote surfactant exchange. Subsequently, the sample was subjected to SEC, run in the absence of detergent in the mobile phase buffer, which confirmed that amphipol solubilized pores remained monodisperse. Notably, the SEC profile showed an even narrower elution profile compared to the sample eluted in presence of detergent (**Fig. 4.14b**). Negative-stain TEM micrographs revealed that pores in amphipol surfactant remained well separated in vitreous ice (**Fig. 4.14a**, *middle*). However, YaxAB now assumed a preferred top-view orientation, which is detrimental to achieving isotropic, high-resolution maps[9]. Recent cryo-EM work on other membrane proteins demonstrated that addition of fluorinated detergents, just prior to sample vitrification, alleviated preferred particle orientation[10,11]. Indeed, addition of up to 3 mM fluorinated Fos-choline 8 to amphipol solubilized YaxAB before vitrification improved its orientation distribution in ice (**Fig. 4.14a**, *bottom*). Using this optimized sample preparation procedure, several cryo-EM grids were prepared for high-resolution data acquisition as outlined in the next section.
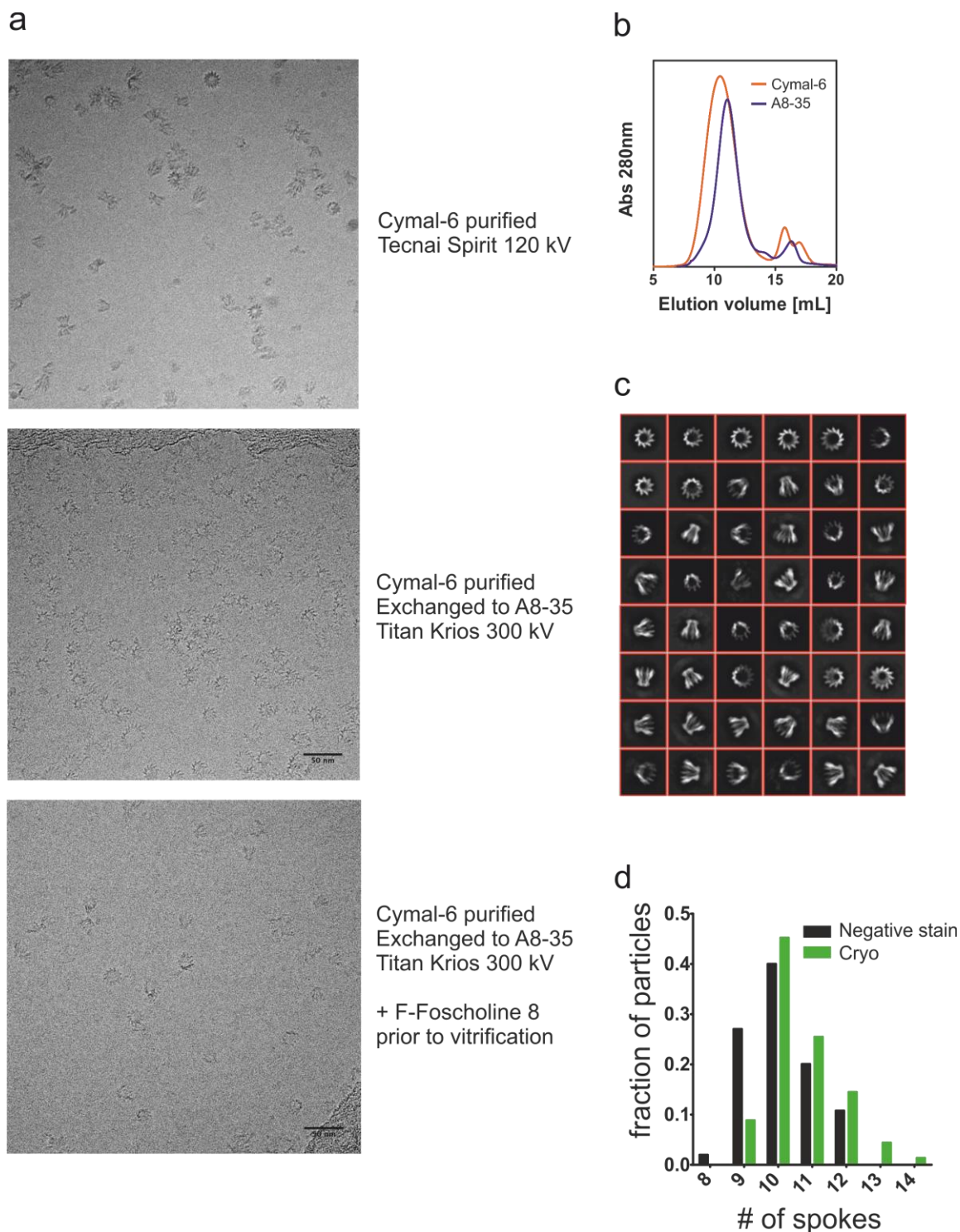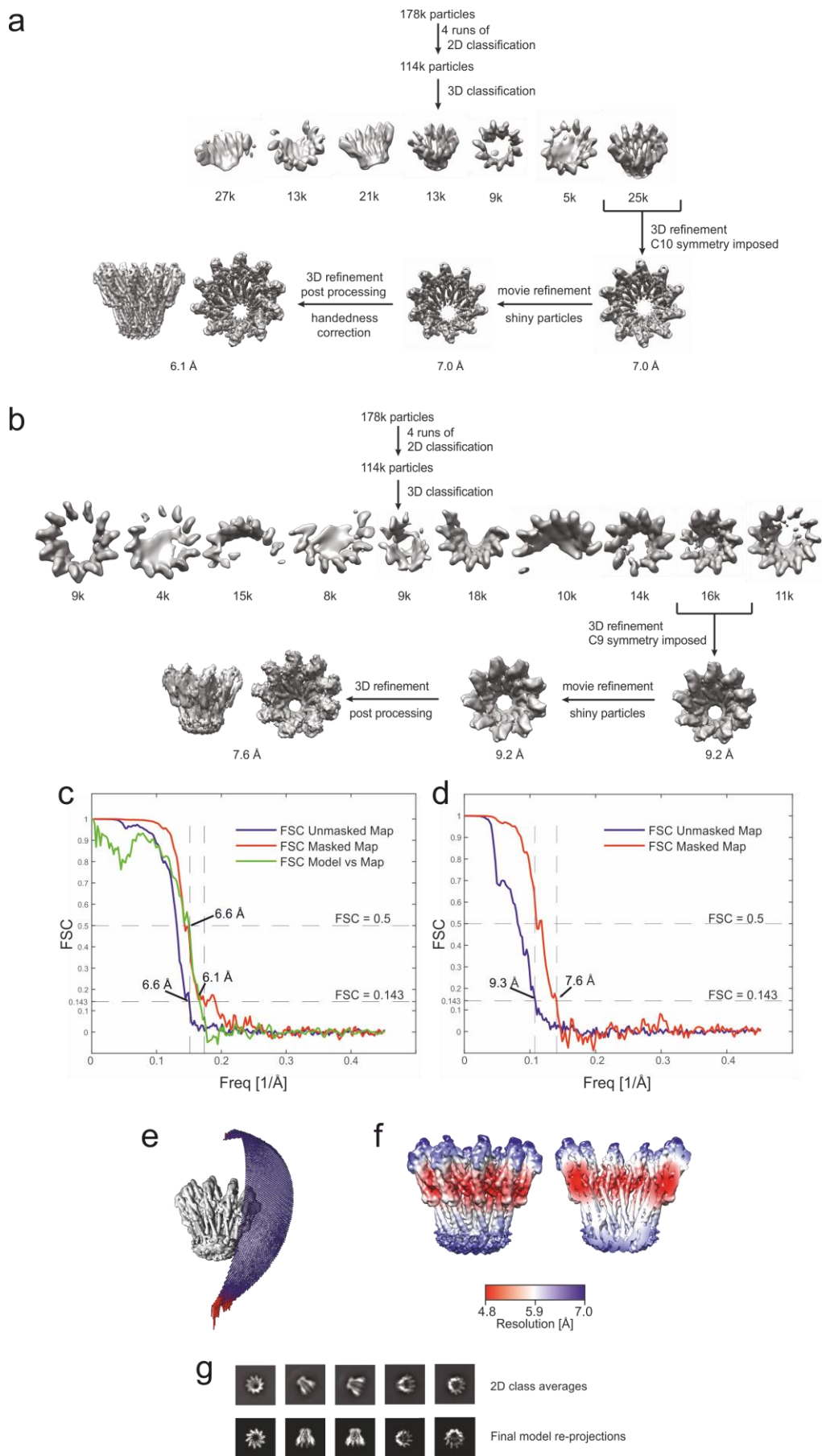
a

Cymal-6 purified
Tecnai Spirit 120 kV

b

Cymal-6 purified
Exchanged to A8-35
Titan Krios 300 kV

c

Cymal-6 purified
Exchanged to A8-35
Titan Krios 300 kV

+ F-Foscholine 8
prior to vitrification

d

Fig. 4.14 Cryo-EM analysis of YaxAB. a) Amphiphol exchange of Cymal-6 purified YaxAB as the last step of sample preparation for cryo-EM. Shown are the first SEC trace of detergent-treated YaxAB run in presence of Cymal-6 (orange) and the second SEC run after amphiphol exchange in absence of detergent (purple). b) Representative cryo-EM micrographs of detergent purified (top) and amphiphol exchanged (bottom) YaxAB. In detergent, particles tended to aggregate into long stacks while in amphiphol the complexes remained separate. c) Gallery of 2D class averages after four rounds of classification, starting from 178,000 raw particles selected from automated particle picking. d) Comparison of top-view radial spoke numbers between negative-stain and cryo-EM datasets. In both cases, the majority of particles possessed C10 symmetry.

4.7.2 Single-particle analysis of YaxAB in vitreous ice

In total, 4859 micrographs were collected on a Titan Krios microscope, operating at 300 kV and equipped with a Falcon III direct electron detector. 1000 particles were picked by hand, 2D classified and used as templates for automatic particle picking. This procedure yielded 178,148 raw particles, which were sorted through four rounds of 2D classification (**Fig. 4.14c**). Top-view classes with clear symmetries were apparent, showing a distribution similar to the one obtained with the negative-stain dataset (**Fig. 4.14d**). Again, particles bearing C10 symmetry were the most common.

This sorted set of particles was subsequently 3D classified, using the negative-stain YaxAB pore reconstruction (low-pass filtered to 60 Å) as an initial reference. **Figure 4.15a** displays the 3D classes obtained, whereby one class of 25,000 particles (~20 % of those classified) with C10 symmetry showed the most complete features. This group was 3D refined, imposing C10 symmetry, producing a map at 7 Å resolution (according to the Fourier shell correlation (FSC) = 0.143 criterion). Further post processing procedures, including the correction of handedness (apparent by the appearance of unusual right-handed coiled-coils), improved the map resolution to 6.1 Å (FSC = 0.143; **Fig. 4.15c**). Given that the pores adopt different stoichiometries, increasing the desired number of 3D classes revealed a population of C9 symmetric particles (**Fig. 4.15b**). These particles were refined as performed for the C10 complex, yielding a map with 7.6 Å resolution (FSC = 0.143; **Fig. 4.15d**). Because of the higher resolution achieved for the C10 complex, this map will be used for subsequent model building and analysis. The C9 complex reveals largely identical subunit arrangement as the predominant C10 complex, indicating that an amount of flexibility is inherent to the YaxAB system (**Section 4.7.4**). The final map (C10) was reconstructed from a wide distribution of particle orientations (**Fig. 4.15e**) and ranged in local resolution from 4.8 Å in the head domains to 7 Å in the pore periphery (**Fig. 4.15f**). A comparison between 2D projections of the C10 symmetric reconstruction, to experimentally derived 2D classes, confirmed correct data processing procedures (**Fig. 4.15g**).

Fig. 4.15 (next page) Cryo-EM 3D reconstruction and validation. a) Workflow of 3D reconstruction for the C10 symmetric complex. b) Workflow of 3D reconstruction for the C9 symmetric complex. c) FSC plot for C10 pore reconstruction. d) FSC plot for C9 pore reconstruction. e) Particle orientation distribution and f) local resolution maps for the final reconstruction with C10 symmetry. g) Comparison of selected experimental 2D class averages with similar views from 2D projections of the C10 symmetric map.

a

178k particles → 4 runs of 2D classification → 114k particles → 3D classification

27k 13k 21k 13k 9k 5k 25k

3D refinement
C10 symmetry imposed

3D refinement
post processing

handedness
correction

movie refinement
shiny particles

6.1 Å   7.0 Å   7.0 Å

b

178k particles → 4 runs of 2D classification → 114k particles → 3D classification

9k 4k 15k 8k 9k 18k 10k 14k 16k 11k

3D refinement
C9 symmetry imposed

3D refinement
post processing

movie refinement
shiny particles

7.6 Å   9.2 Å   9.2 Å

c

FSC Unmasked Map
FSC Masked Map
FSC Model vs Map

6.6 Å
6.6 Å   6.1 Å

FSC = 0.5
FSC = 0.143

FSC
Freq [1/Å]

d

FSC Unmasked Map
FSC Masked Map

9.3 Å   7.6 Å

FSC = 0.5
FSC = 0.143

FSC
Freq [1/Å]

e

f

4.8   5.9   7.0
Resolution [Å]

g

2D class averages

Final model re-projections

4.7.3 Fitting of YaxA and YaxB crystal structures into the YaxAB cryo-EM map

From the EM map (C10) it was apparent which densities could be assigned to YaxA to YaxB, given each subunit's distinct orientation of the head domain relative to the coiled-coil stalk (**Fig. 4.16a**). A full model of YaxB was obtained by threading its amino acid sequence through the PaxB crystal structure, which resulted in a fully modeled orthologue. Both YaxA and YaxB structures were first rigid body refined into the cryo EM map.

Subsequently, most protein regions could be placed into the helical densities by real space refinement, though the YaxB foot domain required retracing due to significant conformational changes compared to its structure as a monomer (**Fig. 4.16**). Despite the medium resolution of the map, bulky side-chain densities (for tryptophan, tyrosine, lysine, arginine and histidine) were occasionally visible, aiding in the accurate assignment of amino acid sequence register throughout the map. Finally, real space refinement including non-crystallographic symmetry (NCS) and secondary structure restraints produced a pore model with good stereochemistry and no Ramachandran geometry outliers.

Though the fitted and refined models were well accommodated by the cryo-EM density (with the map-to-model FSC = 0.5 occurring at 6.6 Å, indicating good correspondence between experimental and model-generated maps up to this resolution; **Fig. 4.15c**), independent biochemical validation was envisioned to confirm the modeled subunit arrangement. Two approaches were employed to this end. First, the C-termini of both YaxA and YaxB were fused to maltose-binding protein (MBP), a ~70 kDa protein. Each MBP-tagged subunit was mixed with the corresponding untagged interacting subunit, treated with Cymal-6 detergent to dissociate aggregated pores and purified by SEC (Superose 6). Subsequently, the complexes were imaged in negative-stain TEM and 2D-classified (**Fig. 4.17a**). Consistent with the cryo-EM model, complex containing YaxB-MBP show 2D classes with additional density inside the pore, while those with YaxA-MBP display extra density outside the pore. Another approach was crosslinking followed by mass spectrometry (XL-MS), which identifies residues in spatial proximity consistent with the crosslinker length (in this case up to 25 Å). Though the number of high-confidence crosslinks was relatively low, a set of residue pairs in the coiled-coil stalk domain was in agreement with the modeled arrangement of subunits (**Fig. 4.17b**). Together, these independent biochemical results validate the YaxAB model presented in the next section.
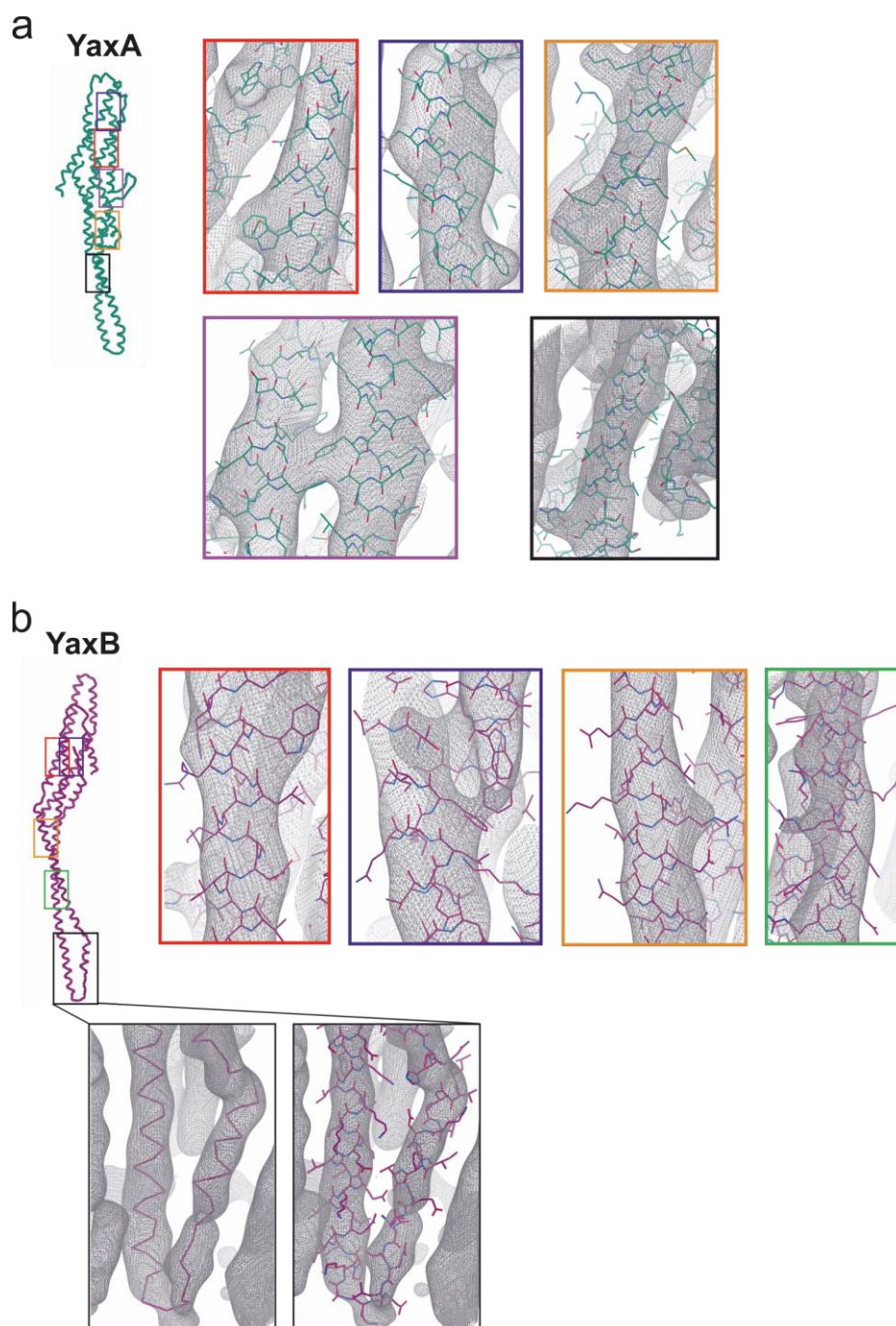
Fig. 4.16 Quality of the cryo-EM map and refined structures. a) Examples of the final map at different regions of the protomeric YaxA and b) YaxB models. Density for the YaxB transmembrane helices α4′ and α4′′ is overlaid with a Cα-trace (*left*) and with side-chains modeled (*right*). Maps are displayed at a contour level of 7σ.
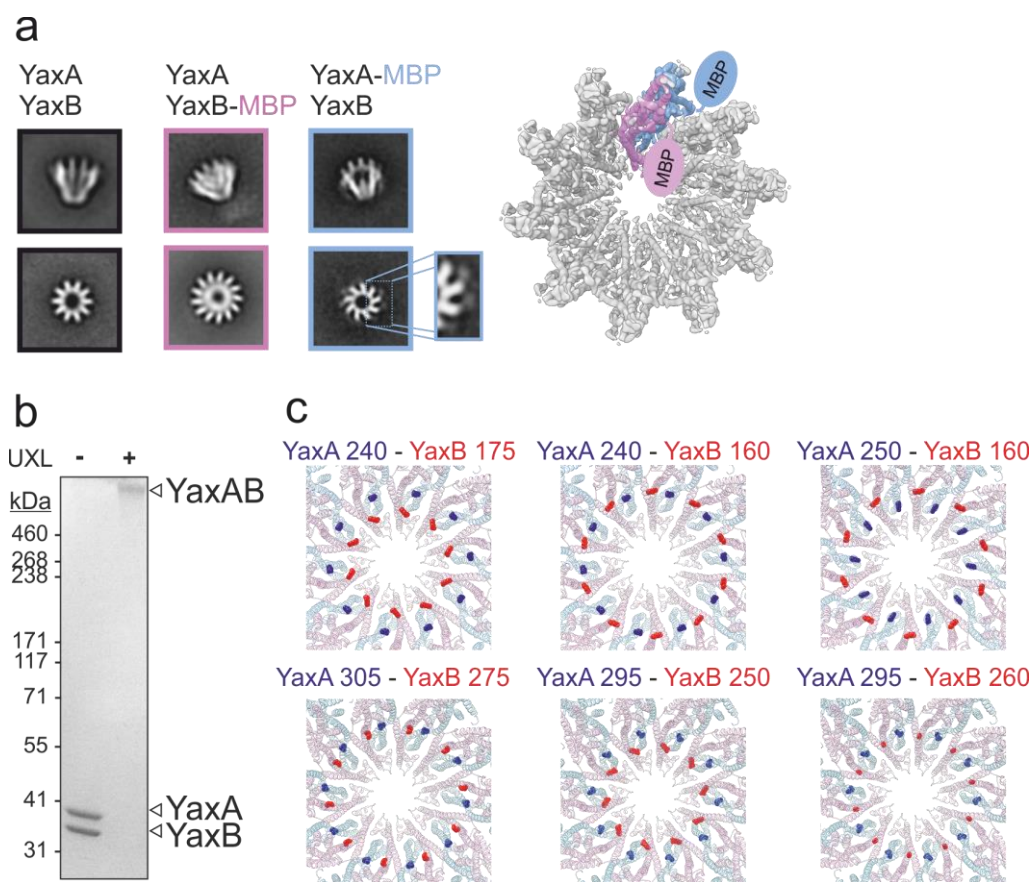
Fig. 4.17 Biochemical validation of the YaxAB model. a) Localization of the YaxA and YaxB C-termini within the YaxAB complex by MBP-tagging and TEM analysis. C-terminal MBP-fusions of YaxA and YaxB were mixed with the respective un-tagged interaction partner and detergent treated. Negative-stained complexes were imaged by TEM and subjected to 2D classification. Compared with native YaxAB classes (black), both MBP-tagged complexes revealed additional density inside (pink, YaxB-MBP) and outside (blue, YaxA-MBP) the spoked rim. The inset illustrates an enlarged detail of the additional densities encircling the complex containing YaxA-MBP. Shown on the right is the location of the MBP tags relative to the cryo-EM map of YaxAB. b) XL-MS supports the arrangement of YaxA and YaxB coiled-coils in the YaxAB model. YaxAB (membrane extracted as in Fig. S6) at 5 - 10 µM was crosslinked with the amine-reactive homobifunctional cross-linker DSBU. SDS-PAGE analysis and Coomassie staining (*left*) confirmed cross-linking efficiency, resulting in one covalent high-molecular weight species. A high density of cross-links was identified between the coiled-coil stalks of YaxA and YaxB. *Right*: Residues of YaxA (red) cross-linked to YaxB (blue) are presented pairwise. The DSBU cross-linker bridges distances up to 25 Å.

4.7.4 Architecture of the YaxAB pore

A distinct funnel shape and large overall dimensions of 160 Å (top to bottom) by 200 Å (side to side) characterize the C10 symmetric YaxAB pore architecture (**Fig. 4.18a**). As evident from the map, one radial spoke of density accomodates a YaxA-YaxB heterodimer. Notably, YaxA protomers lack contact sites to each other within the pore, but instead interact with two YaxB protomers in *cis* and *trans* (**Section 4.7.5**). Viewed from the top, the pore is built from an outer and inner ring YaxA and YaxB protomers, respectively, in agreement with the MBP-tag experiments (**Fig. 4.17a**). The amphipol surfactant density, colored in yellow in **Figure 4.18a**, delineates the approximate membrane boundaries. This feature is often observed in cryo-EM maps[7,12] and is useful in delineating the transmembrane regions of membrane proteins. Both YaxA foot helices α4 and α5 and YaxB helices α4' and α4'' are embedded inside this amphipol density, indicating these regions to be the likely transmembrane domains of the pore (**Fig. 4.18b,c**). Calculating the pore diameter along its axis indicates the narrowest distance of about 31 Å, which is comparable to the ClyA pore diameter[4].

In the C9 symmetric complex, the subunit arrangement remains largely identical to the predominant C10 particles (**Fig. 4.19a**). The pore diameter is uniformly reduced by ~10 Å along the entire z-axis, indicating a substantial degree of structural flexibility inherent to YaxAB (**Fig. 4.19b**). This flexibility is especially apparent in the coiled-coil stalk and foot domains of the subunits, when compared between C9 and C10 assemblies (**Fig. 4.19c**). Here, helices move to accommodate the tighter arrangement of YaxA-YaxB dimers in the smaller complex. Together, the ability to obtain pore reconstructions with C9, C10 and C11 (negative-stain; **Fig. 4.13**) symmetries demonstrates the unusually heterogeneous composition of YaxAB and the unique suitability of single particle EM in the analysis of this PFT class.
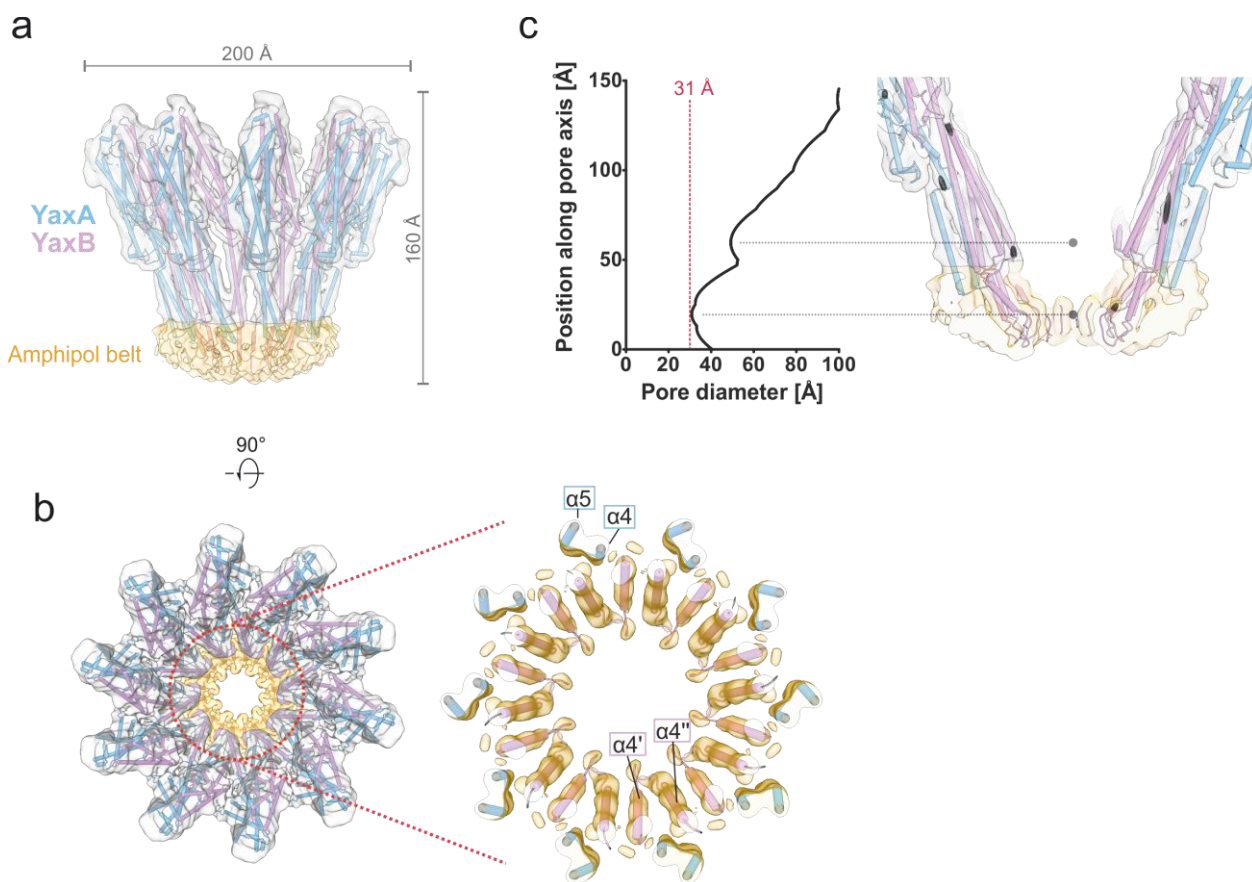
Fig. 4.18 Architecture of the YaxAB pore (C10). a) Final sharpened cryo-EM density of YaxAB together with the refined pore model (side view). The chosen contour level (4.5 σ) corresponds to 1.21 Å³/Dalton. Fitted YaxA and YaxB models are colored blue and pink, respectively. The amphipol belt, illustrated in gold, demarcates the putative transmembrane region. Dimensions of the complex are given in Å. b) Top view of the pore complex, overlaid with the cryo-EM map. YaxA and YaxB form outer and inner rings, respectively (*left*). A zoom of the amphipol-enclosed portion of the complex (*right*) is contoured at 6.5 σ to better distinguish individual helices. Labels of the secondary structure elements adhere to the nomenclature shown in Fig. 1b. c) Pore diameter plotted against the coordinate along the vertical axis. Calculations have been performed using the program HOLE[17] (*left*). The red line indicates the narrowest point in the channel. Two major constrictions along the YaxAB model are emphasized (*right*).
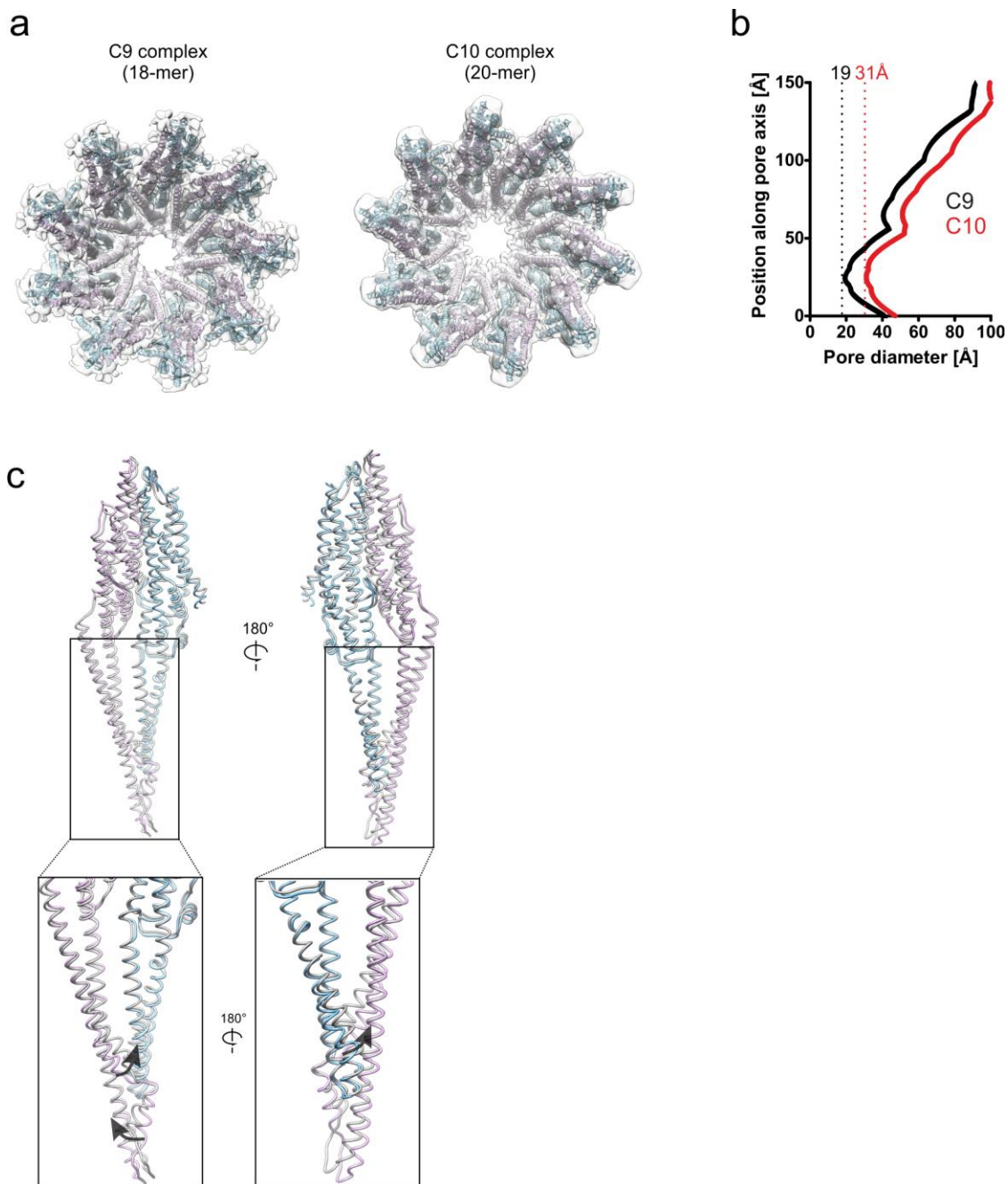
Fig. 4.19 Comparison of C9 and C10 symmetric pore complexes a) C9 symmetric (*left*) and C10 symmetric (*right*) YaxAB pore models fitted into the respective cryo-EM densities. b) Pore diameter of the C9 (black) and C10 (red) complex plotted against the coordinate along the vertical axis. Calculations have been carried out with the program HOLE. c) Superposition of *cis*-dimers in the C10 (blue/pink) and C9 (grey) complexes. Arrows emphasize regions of significant rearrangement.

4.7.5 Interfaces between subunits in the YaxAB pore

The cryo-EM model of the YaxAB pore allows for an analysis of the type of subunit interfaces governing its unusual multimer-of-heterodimers assembly. The complex is held together by heterotypic interfaces within and between neighboring radial spokes. Within one spoke (*cis*), YaxA and YaxB head domains form a large interface of about 1500 Å^2. Numerous hydrophobic and polar contacts line this interface, as illustrated in **Figure 4.20a** (amino acid side chains are shown in this figure, but were modeled as ideal rotamers, since the medium resolution of the map did not permit most residues to be visualized).

Conspicuously, the coiled-coil stalks of both subunits remain distinctly apart and do not engage in obvious interactions, which is somewhat surprising, as heteromeric coiled-coils are often seen to mediate protein-protein interaction[13–15]. The second major *cis*-interface is formed between the foot domains of YaxA and YaxB, burying a solvent accessible surface of about 1100 Å^2 (**Fig. 4.20a**). Unlike the first *cis*-interface formed between head domains, the mostly hydrophobic interfacial residues between the foot domains are generally well conserved (see **Fig. 5.1** in **Discussion**). These include L196, F237, F268, I272 and F285 from YaxA; and residues L196, F237, Y243 and I244 from YaxB.

On the other hand, the nature of the interaction between adjacent radial spokes, i.e. between adjacent YaxA-YaxB dimers (*trans*) remains to clarified. As illustrated in **Figure. 4.20b**, neighboring YaxA and YaxB protomers engage via an apolar interface formed at the junction between head and stalk domains. This region includes the well-conserved YaxA residues I52 and L325; and the YaxB residues V40, V42 and L43. To see whether this *trans*-interface can be perturbed by introducing charged residues, the mutants YaxA(I332D) and YaxB(V42D) were generated, which places opposing negative charges. As seen in subsequent SEC analysis (**Fig. 4.20c**), the elution profile of these mutant complexes shifts to smaller sizes, indicating a disturbed *trans*-interface. YaxA and YaxB still co-elute, given the intact *cis*-interface. These results support a model in which pore oligomerization proceeds by association of *cis*-dimers along their exposed *trans*-interfaces (see **Discussion**).

Apart from these three major heterotypic interaction sites, another smaller interface is formed between foot domain helices of adjacent YaxB protomers (**Fig. 4.20d**). This site is analyzed in more detail in **Section 4.7.6**.
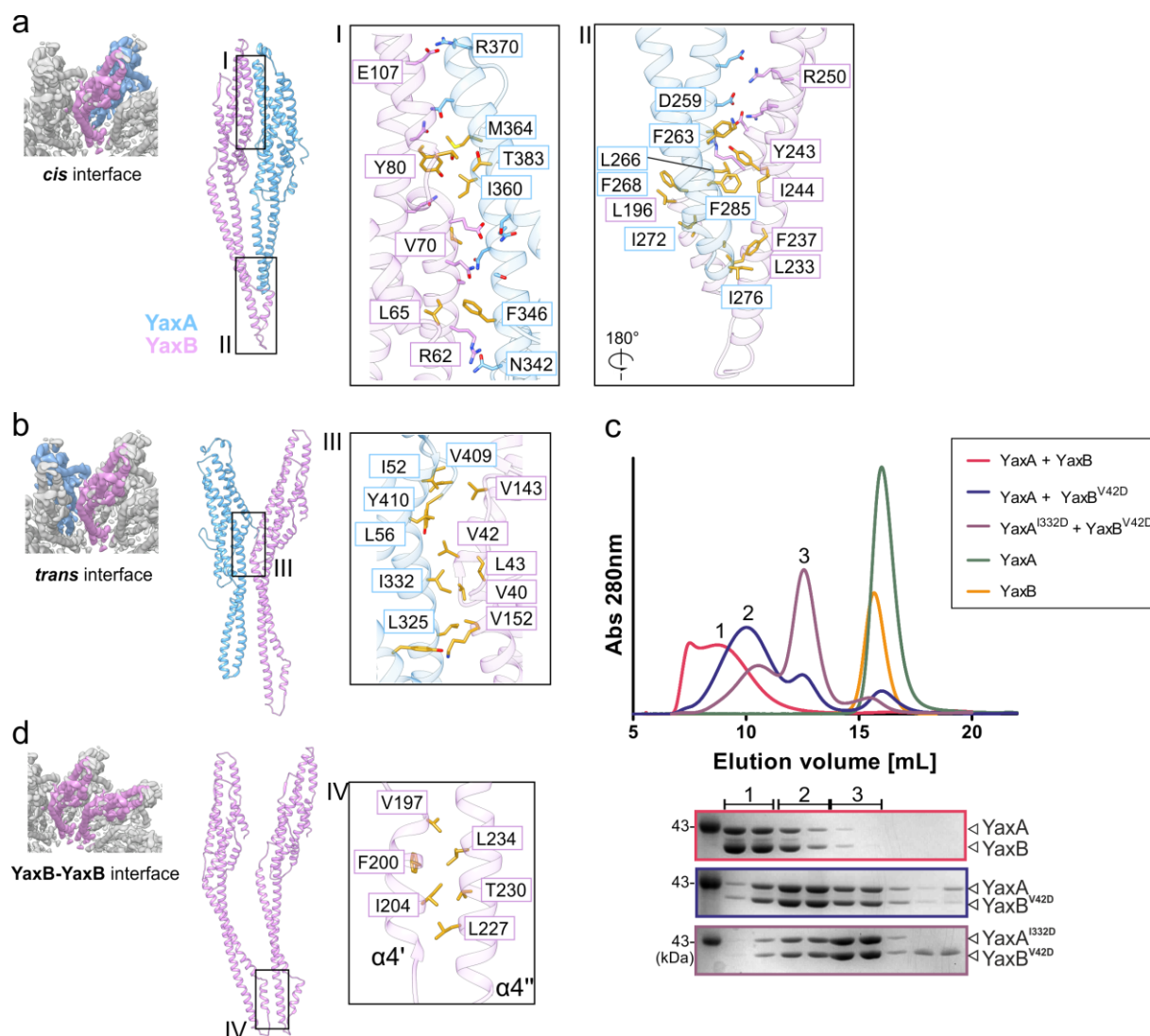

Fig. 4.20 Subunit interfaces in the YaxAB pore a) Cryo-EM map (*left*) and modeled structure (*right*) of the cis interface between YaxA (blue) and YaxB (pink) within a radial spoke (*cis*). Boxes labeled I and II indicate contact regions within the protomer pair that are displayed enlarged (*right*). Residues in interacting proximity are shown as sticks; hydrophobic side chains are colored in gold. b) Depiction as in a), but of the *trans* interface between YaxA and YaxB from two adjacent radial spokes. Box III indicates the contact region between the protomer pair, colored as in a). c) SEC analysis (Superose 6) of YaxAB complexes containing putative *trans*-interface mutants. SDS-PAGE analysis of the same fractions across different runs illustrates the shift in oligomer size, towards smaller assemblies, as more negative charges are introduced into the apolar interface. d) Depiction as in a), but of the homotypic YaxB-YaxB foot domain interface, colored as in a).

4.7.6 Characteristics of the YaxAB transmembrane segment

From the cryo-EM density, it is apparent that both YaxA and YaxB foot domain helices are localized inside the amphipol surfactant belt, i.e. that these helices are the likely transmembrane moieties of the toxin (**Fig. 4.18**). One such transmembrane segment – comprising the foot domain helices from one YaxA-YaxB *cis*-dimer – is shown in **Figure 4.21a**, after the entire pore complex was placed inside a membrane *in silico* using the PPM (positioning of proteins in membranes) server[16]. This approach delineates the hydrophobic thickness of the transmembrane domain, which is about 28 Å for YaxAB.

Strikingly, YaxA helices α4 and α5 traverse approximately half of the membrane distance, which is unlikely to suffice for full membrane penetration. However, the YaxB helices α4' and α4'' allow full penetration of the hydrophobic layer by the YaxA-YaxB dimer. Thus, both YaxA and YaxB foot domains partake in transmembrane pore formation, by each contributing aliphatic helix structures inside the target bilayer.

As the only apparent homotypic protomer-protomer interface of the complex, adjacent YaxB foot domain helices form a hydrophobic "seal" between the luminal and external faces of the pore, including the conserved α4' residues V197, F200 and I204, and the α4'' residues L234 and L227. This interaction likely contributes favorably to YaxA-YaxB dimer association inside the membrane, in addition to the solvent-exposed *trans*-interface (**Fig. 4.20b**). Surface rendering of the cryo-EM pore model confirms the hydrophobic nature of the membrane-exposed foot region (**Fig. 4.21b**) and the richly hydrophilic pore lumen (**Fig. 4.21c**).
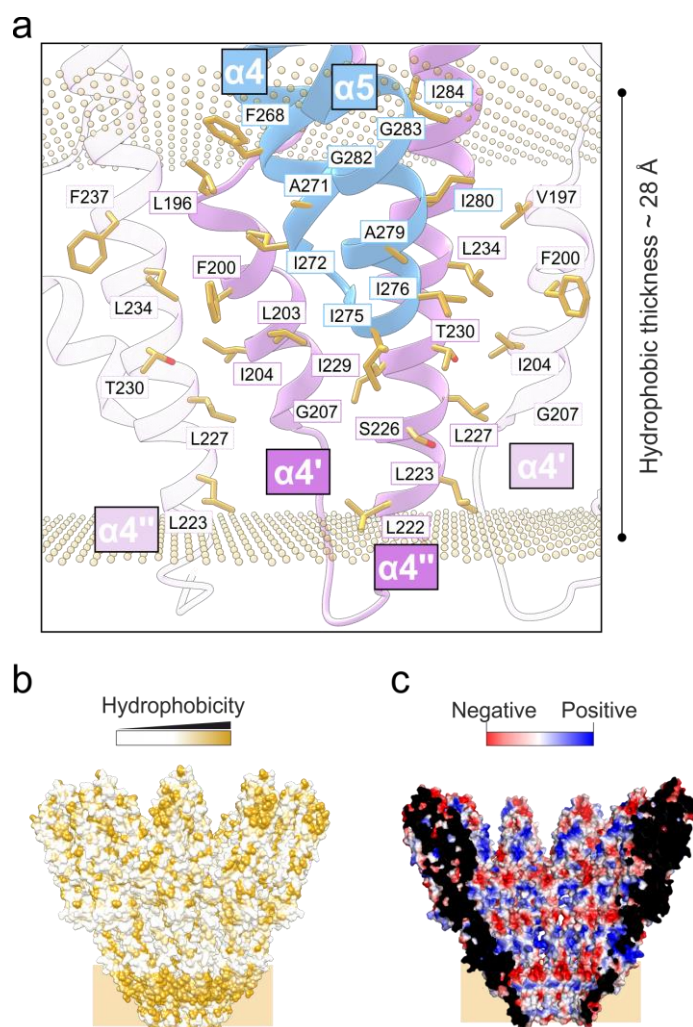
Fig. 4.21 Characteristic of the transmembrane segment. a) Details of a transmembrane segment of the pore. The YaxAB pore model was submitted to the PPM server to delineate the buried hydrophobic membrane surface. Shown are foot domains from one *cis*-dimer as well as the neighboring protomers (transparent ribbons). Membrane exposed residues are colored in gold. The golden spheres demarcate the calculated boundaries of the lipid membrane. b) Hydrophobic surface rendering of the YaxAB model. The golden rectangle delineates the approximate membrane boundaries. c) Charge distribution of the pore lumen. The surface is rendered by qualitative electrostatic representation in PyMOL (Schrödinger, LLC).

4.8 Conformational changes of YaxA and YaxB accompanying YaxAB pore formation

With both soluble and pore-protomeric forms of the YaxAB toxin components at hand (in case of YaxB, the full-length structure of PaxB serves as a surrogate for comparison, given its high degree of structural homology), the conformational changes accompanying pore transition can now be assessed. Structural superposition between monomeric and oligomeric states for both YaxA and YaxB/PaxB illustrates the regions undergoing the largest rearrangements (**Fig. 4.22a**).

Upon dimerization, YaxA's head domain shifts closer to the YaxB head domain to engage in the extensive *cis*-interaction outlined in **Figure 4.20a**. This movement results in a RMSD of 1.1 Å across 259 aligned C_α pairs, which is a modest overall shift. For the YaxB head domain, a comparably small rearrangement is observed upon interaction with YaxA (1.3 Å RMSD across 178 aligned C_α pairs; **Fig. 4.22b**).

In contrast, the coiled-coil and foot domains of YaxA and YaxB undergo significant displacements (**Fig. 4.22a**). In case of YaxA, these regions perform a swiveling motion towards the incoming YaxB foot domain, presumably to form the conserved hydrophobic interface in *cis*, as illustrated in **Figure 4.19a**. The YaxB foot domain is not resolved in the crystal structure of the monomer, hence a superposition of the PaxB structure, with protomeric YaxB, is necessary. This comparison is warranted, since the foot domain is the most sequence-conserved region between YaxB orthologues, showing ~60 % identity across species (**Fig. 5.1b**). The superposition reveals a striking rearrangement of the YaxB/PaxB foot domain upon complex formation. While this area maintains a globularly packed form in soluble PaxB, with helices α4' and α4'' burying a hydrophobic core against the coiled-coil stalk, this moiety opens up in protomeric YaxB, extruding its hydrophobic core towards the lipid milieu (**Fig. 4.22c**). In this process, the surrounding loops are partially extended and assume helical character together with α4' and α4'' (see also **Fig. 4.21a**).

To support a model, where the YaxB foot domain is poised to undergo large conformational changes required for pore formation, disulfide-locked YaxB foot domain mutants were generated, designed to constrain this lytic opening mechanism in a DTT-dependent manner (**Fig.**

4.23). Two sets of mutants were chosen to produce a disulfide bond at different positions along the foot domain. The I184C/I229C mutant pair rigidifies the foot domain against the coiled-coil helix α4, while the V190C/L223C mutant pair is designed to reduce movement between the two foot domain helices α4' and α4''. Indeed, oxidized YaxB mutants showed significantly impaired lytic activity compared to wild-type (WT) YaxB. Importantly, upon DTT addition, which resolves the disulfide lock, lytic activity returned to WT levels, underlining the importance of conformational freedom in the YaxB foot domain for toxin activity.

Together, the comparison between monomer and protomer structures suggests that YaxB acts as a lytic effector, induced to open its foot domain in a switchblade-like manner upon interacting with YaxA. A more detailed dissection of this functional divergence between the two subunits is presented in the next section, which includes a series of structure-guided mutant studies.
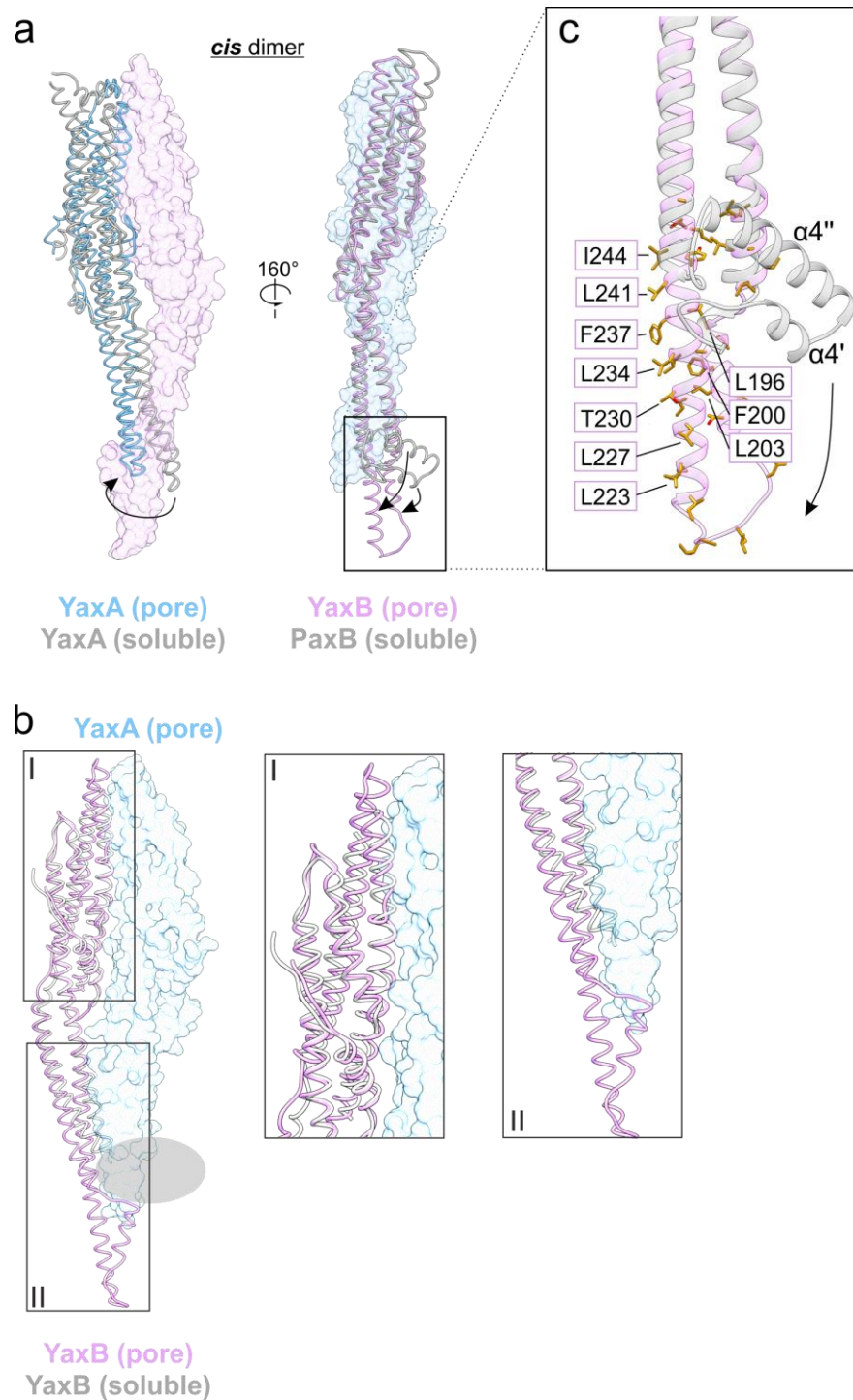
Fig. 4.22 Conformational changes accompanying pore formation. a) Overview of conformational changes within YaxA and YaxB in context of a *cis* dimer. The interacting protomer is shown in transparent surface representation. Alignment has been carried out between head domains only, given the small rearrangements in this region. *Left*: Monomeric (grey) and protomeric (blue) YaxA. *Right*: Monomeric PaxB (grey) and protomeric YaxB (pink). Arrows emphasize the structural rearrangements during oligomerization. b) Structural superposition of YaxB (soluble) with YaxB (pore). The interacting YaxA in *cis* is illustrated as transparent surface (blue). Note the foot domain is not resolved in the monomeric YaxB structure (indicated by a grey oval). c) Details of the conformational change in the YaxB/PaxB foot domain transitioning from monomeric to protomeric states. Apolar side chains are colored in gold.
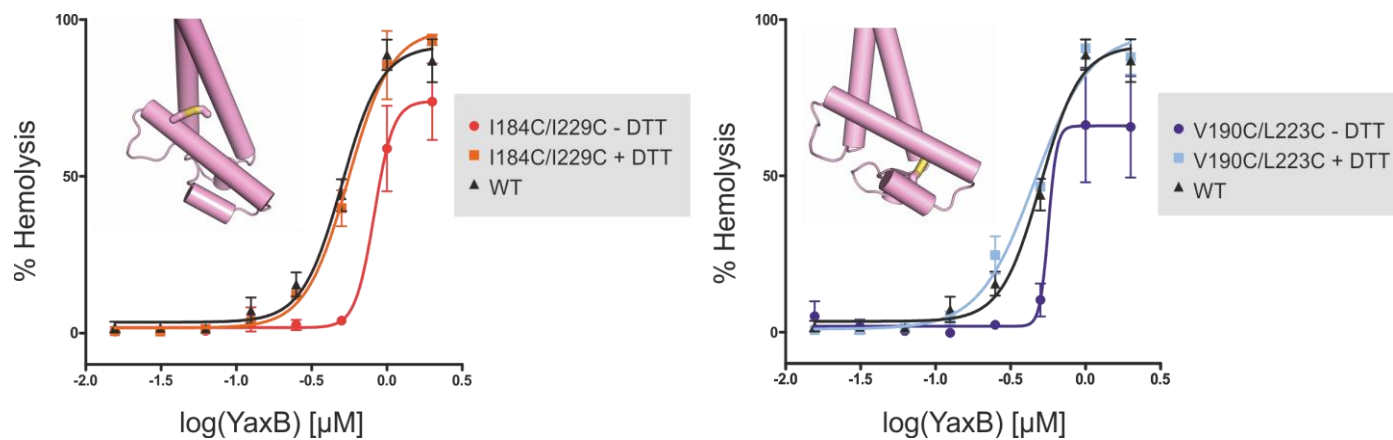
Fig. 4.23 Reducing the flexibility of the YaxB foot domain impair lytic activity. *Left*: the disulfide-locked mutant YaxB(I184C/I229C), after oxidation, shows reduced hemolytic activity compared to the WT (black trace). Erythrocytes were first incubated with YaxA (2 µM), after which YaxB was titrated. *Right*: the disulfide-locked mutant YaxB(V190C/L223C) assayed for hemolytic activity. Upon addition of DTT, lytic activity of both mutants were restored to WT levels. Figure insets illustrate the position of the disulfide bond, using a homology model of the YaxB foot domain based on the PaxB coordinates.

4.9   Biochemical dissection of YaxA and YaxB membrane binding capabilities

4.9.1 YaxA can bind membranes via its conserved foot domain

Having an understanding of the YaxAB pore architecture, including the arrangement of transmembrane moieties from each subunit, is an important insight on this recently discovered class of PFTs. As suggested by its two-component assembly, YaxA and YaxB are likely to have diverging functional roles towards pore formation, analogous to the case of γ-hemolysin outlined in **Section 1.3.3**, where only LukF possesses membrane binding capability on its own. However, it still remains open whether the individual subunits of YaxAB have the ability to bind membranes on their own, prior to pore formation. Thus, structure-guided mutagenesis, together with biochemical assays, were employed.

First, the requirement for sequential action of YaxA and YaxB on membranes, in order for lysis to occur, was confirmed[5,6]. To this end, a liposome floatation assay was applied, using liposomes composed of porcine heart lipids (**Fig. 4.24a**). YaxA alone was able to bind liposomes, while YaxB failed to do so, already indicating a functional non-redundancy between the two subunits. In agreement with previous activity assays (hemolysis for XaxAB[5] and LDH release for YaxAB[6]), adding YaxA and YaxB sequentially to liposomes resulted in binding of both subunits, while their prior mixing caused a loss of membrane association. This observation might indicate the presence of a membrane-binding moiety for YaxA. Strikingly, the YaxA foot domain – which is part of the transmembrane pore (**Fig. 4.21a**) – features a series of fully solvent exposed and conserved hydrophobic residues in its soluble state (**Fig. 4.24b**). To confirm whether this domain mediates YaxA membrane association, aspartate point mutants were introduced at four moderately to well conserved positions along helix α4 and assayed for their ability to cosediment with erythrocyte membranes (**Fig. 4.24c**). As a series of controls, YaxA alone (lane 2; used also as reference for densitometry quantification), YaxB alone (lane 3), sequential addition of YaxA → YaxB (lane 4) or YaxB → YaxA (lane 5), and premixed YaxA and YaxB (lane 6) were subjected to cosedimentation assays. All four aspartate point mutants displayed two- to three-fold reduced membrane cosedimentation relative to YaxA alone (lanes 7 – 10). As expected, a deletion of the entire hydrophobic foot domain (265 – 284) abrogated membrane cosedimentation. Together,

these results strongly imply that YaxA binds to membranes by itself and does so through its conserved foot domain.

How does the impaired membrane binding ability of the YaxA foot domain mutants influence their lytic behavior together with YaxB? The hemolysis assays in **Figure 4.24d** revealed a ~10-fold reduced lytic potential of the YaxA(V264D) mutant, while the other three substitutions (L266D, F268D, I272D) presented even greater loss of lytic activity. Whereas all four point mutants showed similar degrees of impaired membrane binding (**Fig. 4.24c**), these larger differences in lytic potential could be due to the latter three point mutants being at the *cis*-interface between YaxA and YaxB foot domains (**Fig. 4.20a**) and thus likely important in stabilizing the open (lytic) conformation of the YaxB foot domain.

4.9.2 Head domain interaction is sufficient for YaxB recruitment to membrane-bound YaxA

In light of the experimental support for a sequential mode of action for YaxAB, how is YaxB recruited to membrane bound YaxA? In the YaxAB pore model (**Fig. 4.18a**), the head domains of both subunits are projected over 100 Å above the membrane layer. This would be compatible with the head domains interaction first, prior to the series of conformational changes accompanying transmembrane pore formation (**Fig. 4.22**). In an initial experiment, erythrocyte membrane cosedimentation was performed with membranes incubated first with full-length YaxA; subsequently, the isolated YaxB head domain was added and membranes sedimented (**Fig. 4.25a**). This confirmed that the isolated YaxB head domain could be recruited to membrane-bound YaxA. Next, both head domains in isolation were mixed and analyzed by SEC and negative-stain TEM (**Fig. 4.25b**). Remarkably, the head domains were sufficient to form ring-like oligomers resembling the spoked rim of the full-length YaxAB pore. These results support a mechanism whereby YaxB, incapable of membrane association on its own, is recruited to membrane bound YaxA via initial interaction between the exposed head domains.
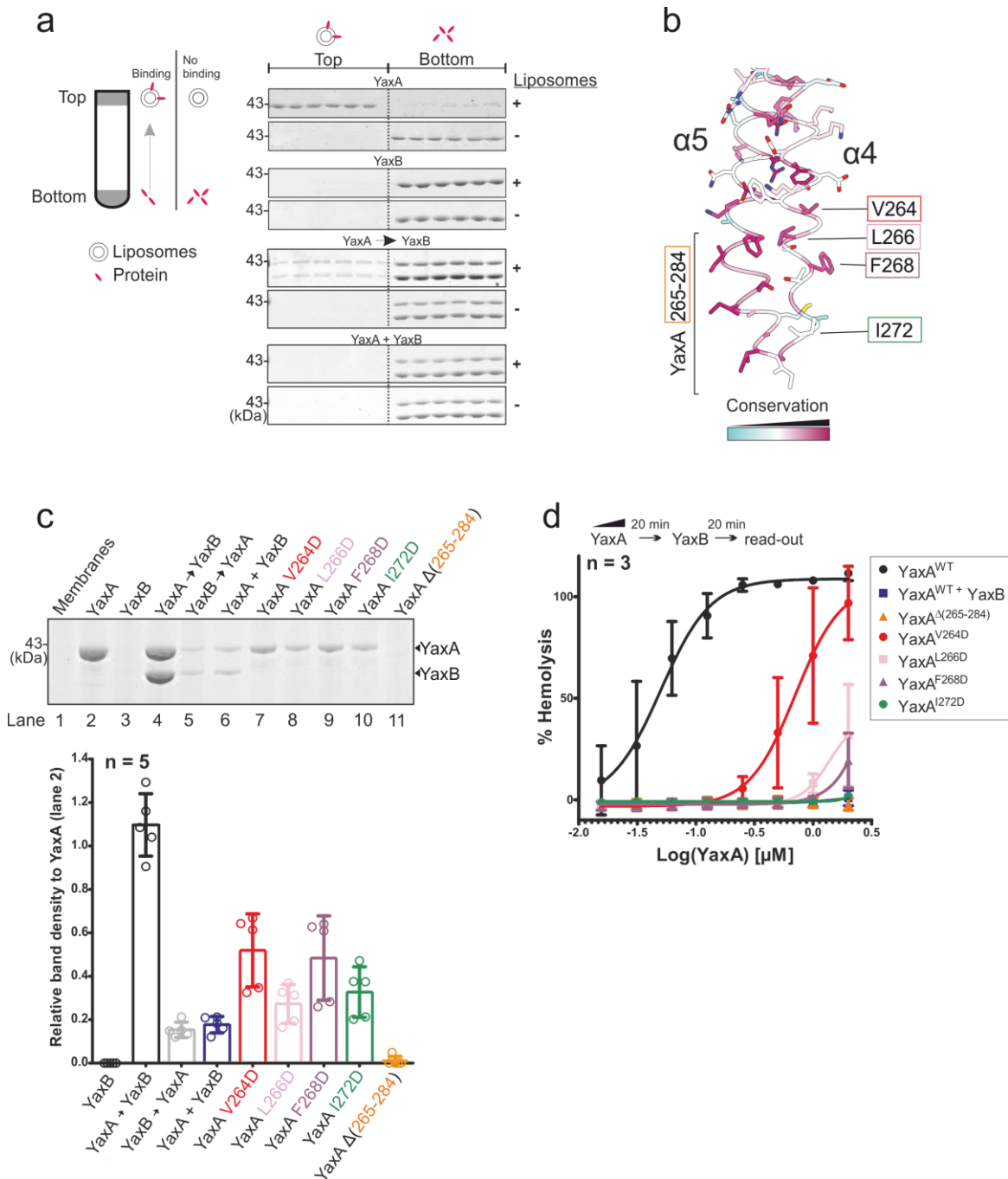
Fig. 4.24 YaxA binds to membranes via its foot domain. a) Liposome floatation assay to test membrane-binding abilities of YaxA and YaxB. *Left*: Schematic presentation of the experiment. *Right*: Membrane binding of YaxA, YaxB, sequentially added YaxA and YaxB (YaxA → YaxB) and pre-mixed YaxA and YaxB (YaxA + YaxB) assessed by Coomassie stained SDS-PAGE analysis of top and bottom gradient fractions. For each sample, a control run was performed without liposomes. b) Close-up view of YaxA's surface-hydrophobic foot domain. c) Erythrocyte membrane co-sedimentation assay of WT and mutant YaxA. *Top*: For each condition, trypsinized erythrocyte ghosts were incubated with the respective toxin component, sedimented and analyzed by Coomassie stained SDS-PAGE. *Bottom*: YaxA band intensities relative to the YaxA-only sample (lane 2) were determined densitometrically from the SDS-PAGE scans. Data points from five independent experiments (n = 5) are shown, along with their means and corresponding standard deviations (SD). d) Erythrocyte hemolysis assay of WT and mutant YaxA. Erythrocytes were treated first with serial dilutions of WT YaxA or its mutants, followed by YaxB addition. Plotted are the averages from three independent experiments (n = 3) along with the SD; solid lines correspond to the the fitted dose-response curves.
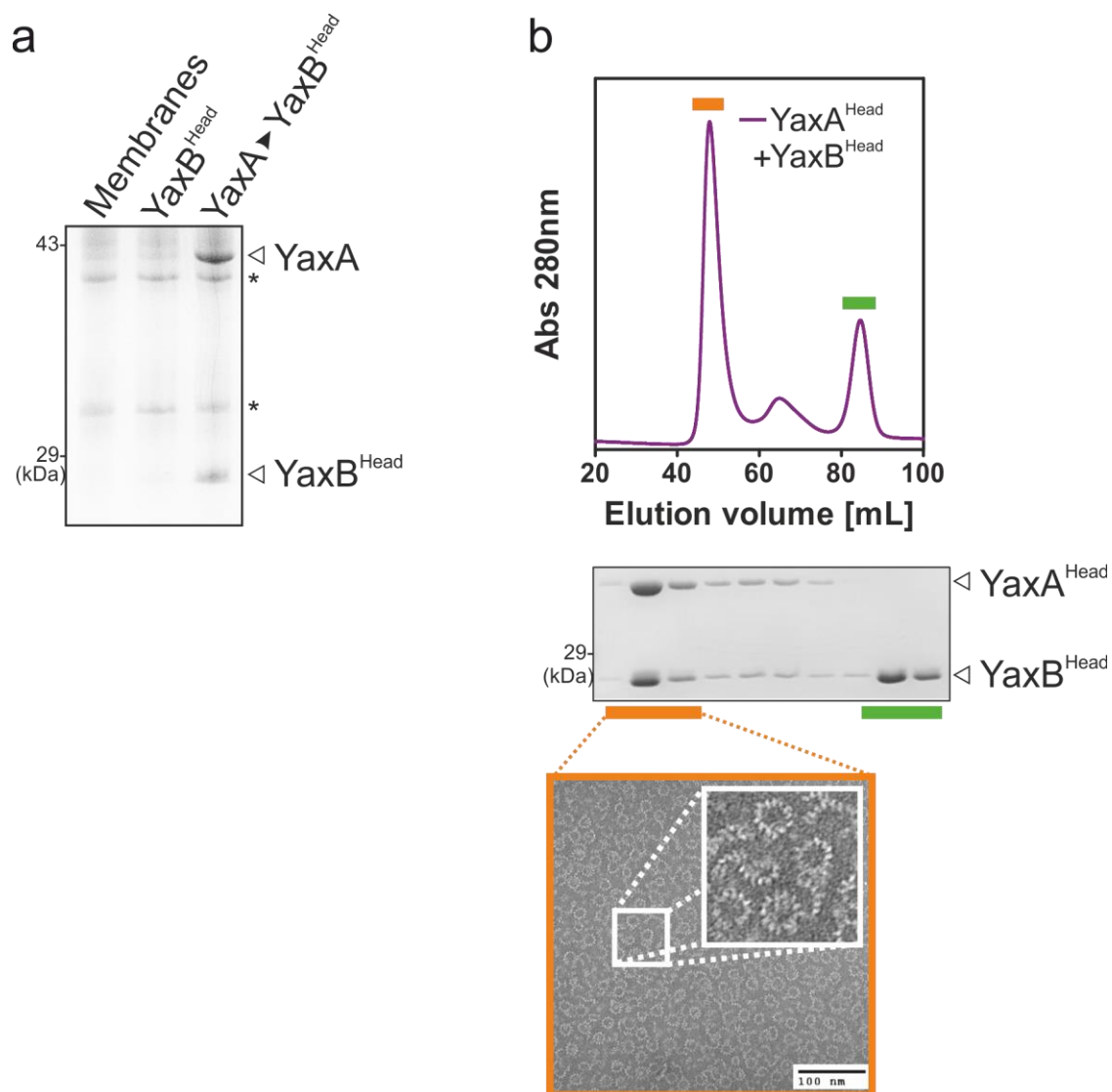
Fig. 4.25 Head domain interactions are sufficient for YaxB membrane recruitment. a) Membrane co-sedimentation assay demonstrating the ability of membrane-bound YaxA to recruit the isolated YaxB head domain to membranes. Membranes were not trypsinized beforehand; hence protein contaminants (asterisks) are present. b) Gel filtration of a 1:1 (w/w) mixture of YaxA and YaxB head domains revealed their oligomerization in solution (*top*). Peak fractions were analyzed by SDS-PAGE and Coomassie staining (*middle*) and fractions containing both proteins were imaged by negative-stain TEM (*bottom*). The isolated head domains form spoked rings resembling the rims of the full-length YaxAB complex. The inset show enlarged details of raw particles.

Bibliography

1. Holm, L. & Rosenström, P. Dali server: conservation mapping in 3D. *Nucleic Acids Res.* **38,** W545–W549 (2010).

2. Wallace, A. J. *et al.* E. coli hemolysin E (HlyE, ClyA, SheA): X-ray crystal structure of the toxin and observation of membrane pores by electron microscopy. *Cell* **100,** 265–276 (2000).

3. Ganash, M. *et al.* Structure of the NheA Component of the Nhe Toxin from Bacillus cereus: Implications for Function. *PLoS ONE* **8,** e74748 (2013).

4. Mueller, M., Grauschopf, U., Maier, T., Glockshuber, R. & Ban, N. The structure of a cytolytic α-helical toxin pore reveals its assembly mechanism. *Nature* **459,** 726–730 (2009).

5. Vigneux, F. *et al.* The xaxAB Genes Encoding a New Apoptotic Toxin from the Insect Pathogen Xenorhabdus nematophila Are Present in Plant and Human Pathogens. *J. Biol. Chem.* **282,** 9571–9580 (2007).

6. Wagner, N. J., Lin, C. P., Borst, L. B. & Miller, V. L. YaxAB, a Yersinia enterocolitica Pore-Forming Toxin Regulated by RovA. *Infect. Immun.* **81,** 4208–4219 (2013).

7. Chen, Y. *et al.* Structure of the STRA6 receptor for retinol uptake. *Science* **353,** aad8266–aad8266 (2016).

8. Zubcevic, L. *et al.* Cryo-electron microscopy structure of the TRPV2 ion channel. *Nat. Struct. Mol. Biol.* **23,** 180–186 (2016).

9. Naydenova, K. & Russo, C. J. Measuring the effects of particle orientation to improve the efficiency of electron cryomicroscopy. *Nat. Commun.* **8,** (2017).

10. Johnson, Z. L. & Chen, J. Structural Basis of Substrate Recognition by the Multidrug Resistance Protein MRP1. *Cell* **168,** 1075-1085.e9 (2017).

11. Zhang, Z., Liu, F. & Chen, J. Conformational Changes of CFTR upon Phosphorylation and ATP Binding. *Cell* **170,** 483-491.e8 (2017).

12. Huynh, K. W. *et al.* Structure of the full-length TRPV2 channel by cryo-EM. *Nat. Commun.* **7,** 11130 (2016).

13. Watkins, A. M., Wuo, M. G. & Arora, P. S. Protein–Protein Interactions Mediated by Helical Tertiary Structure Motifs. *J. Am. Chem. Soc.* **137,** 11622–11630 (2015).

14. Armony, G. *et al.* Cross-linking reveals laminin coiled-coil architecture. *Proc. Natl. Acad. Sci.* **113,** 13384–13389 (2016).

15. Truebestein, L. & Leonard, T. A. Coiled-coils: The long and short of it. *BioEssays News Rev. Mol. Cell. Dev. Biol.* **38,** 903–916 (2016).

16. Lomize, M. A., Pogozheva, I. D., Joo, H., Mosberg, H. I. & Lomize, A. L. OPM database and PPM web server: resources for positioning of proteins in membranes. *Nucleic Acids Res.* **40,** D370-376 (2012).

17. Smart, O. S., Goodfellow, J. M. & Wallace, B. A. The pore dimensions of gramicidin A. *Biophys. J.* **65,** 2455–2460 (1993).

Chapter 5

Discussion

Several figures including legends in this chapter are published in the following manuscript:

"Structure & mechanism of the two-component α-helical pore-forming toxin YaxAB"

Bastian Bräuning, Eva Bertosin, Florian Praetorius, Christian Ihling, Alexandra Schatt, Agnes Adler, Klaus Richter, Andrea Sinz, Hendrik Dietz, Michael Groll

The aim of this thesis was the structural and biochemical characterization of the YaxAB cytolysin from *Y. enterocolitica*. With several reports in the literature now describing the likely involvement of this PFT in virulence[1–4], the elucidation of the YaxAB structure represents an important contribution to the molecular understanding of this family of toxins.

Solving the crystal structures of both YaxA and YaxB – together with PaxB from *P. luminescens* – was a first important goal, as they represent the soluble, monomeric forms of the proteins. The X-ray analysis of these structures confirmed previously proposed[3] resemblance of YaxA to ClyA, the prototypic member of the wider ClyA-like family of PFTs. However, this structural resemblance is limited to the five-helix bundle head domain of YaxA and YaxB, beyond which the two PFT classes diverge substantially. Furthermore, transformation of the soluble ClyA to its homooligomeric pore complex entails large, global conformational changes as revealed by Ban and co-workers[5]. This is different from the modest overall changes in conformation, when YaxA and YaxB become protomeric in the YaxAB complex. Upon oligomerization, YaxB's foot domain opens to expose its amphipathic helices α4' and α4''. This localized motion represents the largest structural rearrangement observed upon pore formation. Here, the YaxA foot domain forms a hydrophobic interaction with the YaxB foot helices within one protomeric YaxA-YaxB pair, suggesting that dimerization might suffice for the opening of the YaxB foot domain.

The membrane active foot domains of YaxA and YaxB represent the protein regions with the highest degree of sequence conservation across bacteria harboring this PFT (**Fig. 5.1**). In YaxA orthologues, the foot sequence is almost invariantly conserved, attesting to its importance in initiating toxin assembly at target membranes. YaxB orthologues feature ~60% sequence identity in the foot domain. Thus, while YaxAB-like toxins exist in bacteria with a broad host range, including human, insect and plant pathogens, they most likely share the same lytic mechanism. Future work on these PFTs should address whether orthologues from bacteria with different host preferences show distinct membrane binding capabilities, considering the specific lipid compositions of plant and animal cell membranes. Identifying protein residues important for host membrane discrimination and analyzing their pattern of conservation offers an exciting opportunity to evaluate the coevolution of virulence factor biochemistry with distinct host membrane preferences.
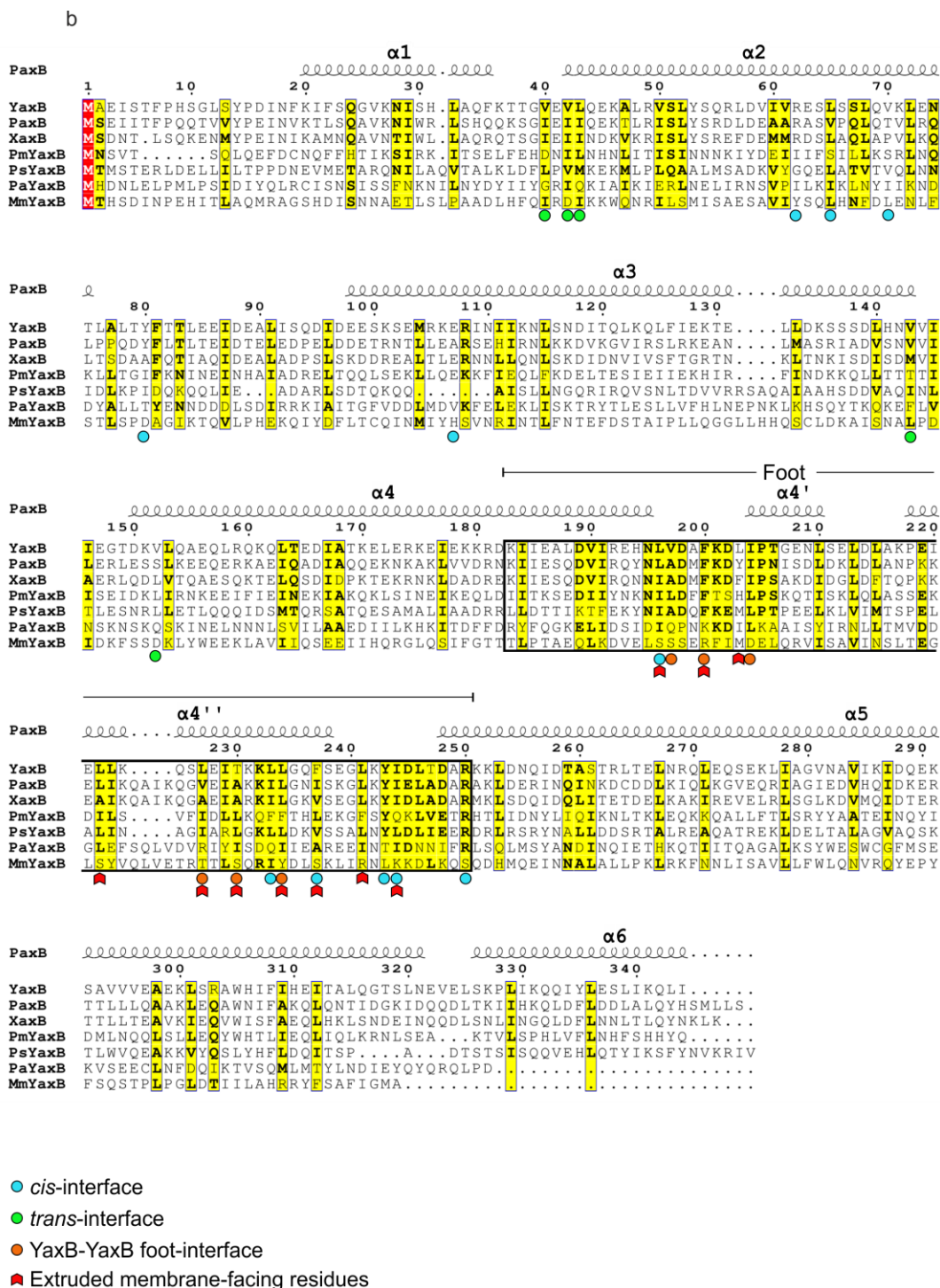
a
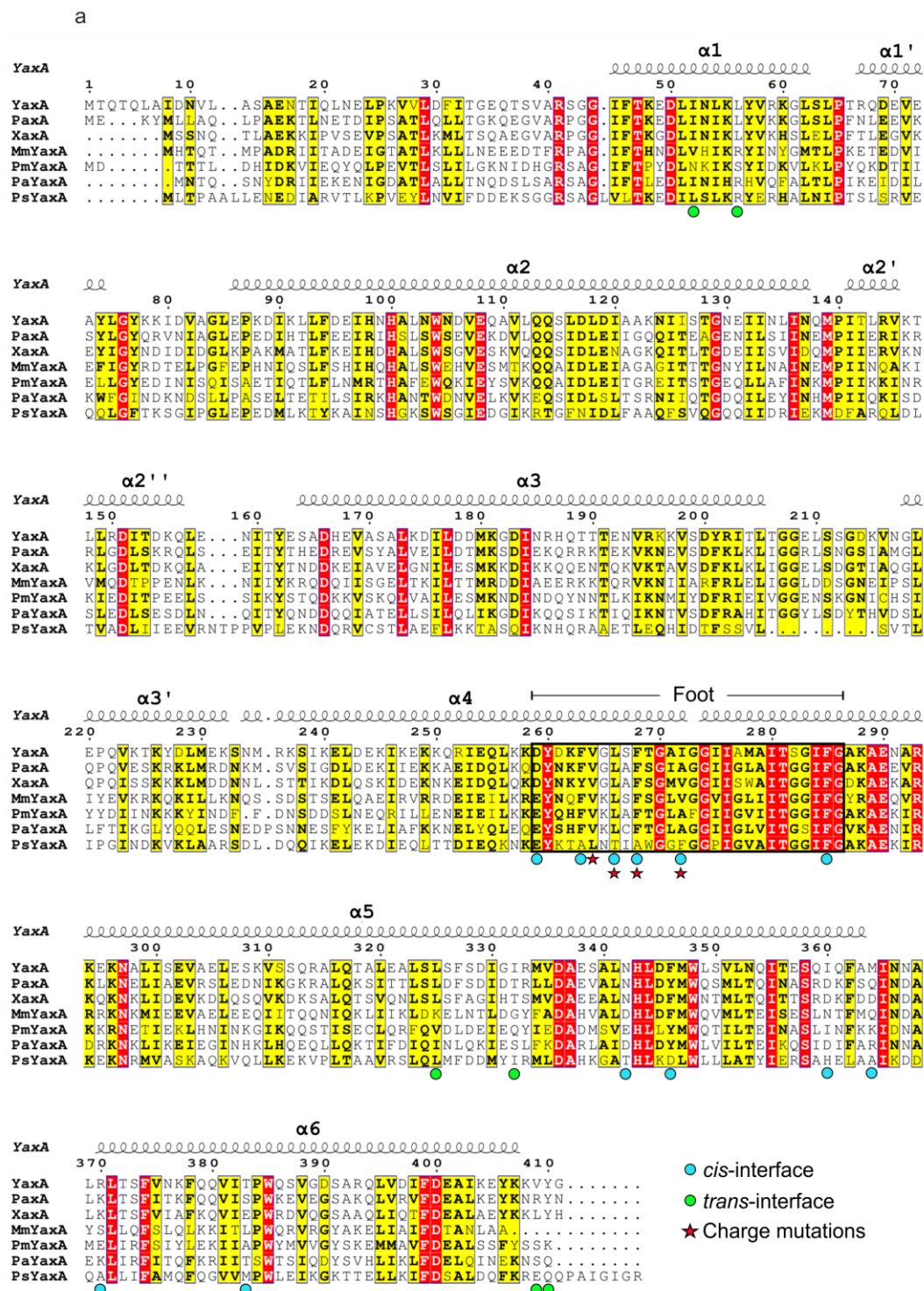
Fig. 5.1 Multiple sequence alignment of YaxA and YaxB orthologues. a) Sequence alignment of YaxA orthologues. Sequences correspond to orthologues from *Providencia alcalifaciens* (PaYaxA), *Pseudomonas syringae* (PsYaxA), *Proteus mirabilis* (PmYaxA), *Morganella morganii* (MmYaxA), *Yersinia enterocolitica* (YaxA), *Photorhabdus luminescens* (PaxA), *Xenorhabdus nematophila* (XaxA). The conserved hydrophobic foot is highlighted by a black frame; positions where charge mutants were introduced are indicated by red stars. Residues engaged in *cis*-type and *trans*-type interaction with YaxB are emphasized by cyan and green circles, respectively. b) Sequence alignment of YaxB orthologues. Sequences were named according to a). The conserved apical foot domain is framed in black. Residues engaged in YaxB-YaxB contacts inside the membrane plane are highlighted by orange circles. Red arrows denote conserved residues facing the lipid milieu as part of the transmembrane segment.

What insights can be gained into the possible assembly mechanism of YaxAB in light of the data presented in this thesis? Intriguingly, the pore-protomeric structure of ClyA closely resembles YaxA and YaxB, in contrast to soluble, monomeric ClyA[6]. This may reflect a similar underlying principle of oligomerization for both homomeric and heteromeric PFT systems. As was elegantly shown by Schuler and colleagues[7] using single-molecule spectroscopy, ClyA in its protomeric, membrane-inserted conformation, proceeds to form closed dodecameric pores by association of sterically compatible multimers (i.e. hexamer with hexamer, pentamer with heptamer etc.). For heteromeric YaxAB, this kind of isodesmic oligomerization could be achieved with membrane-bound, protomeric YaxA-YaxB dimers, which are free to associate through their exposed *trans* interaction patches. This resemblance to ClyA, together with the structural and biochemical data presented in this thesis, allow a proposal for the assembly mechanism of YaxAB and its orthologues (**Fig. 5.2**).
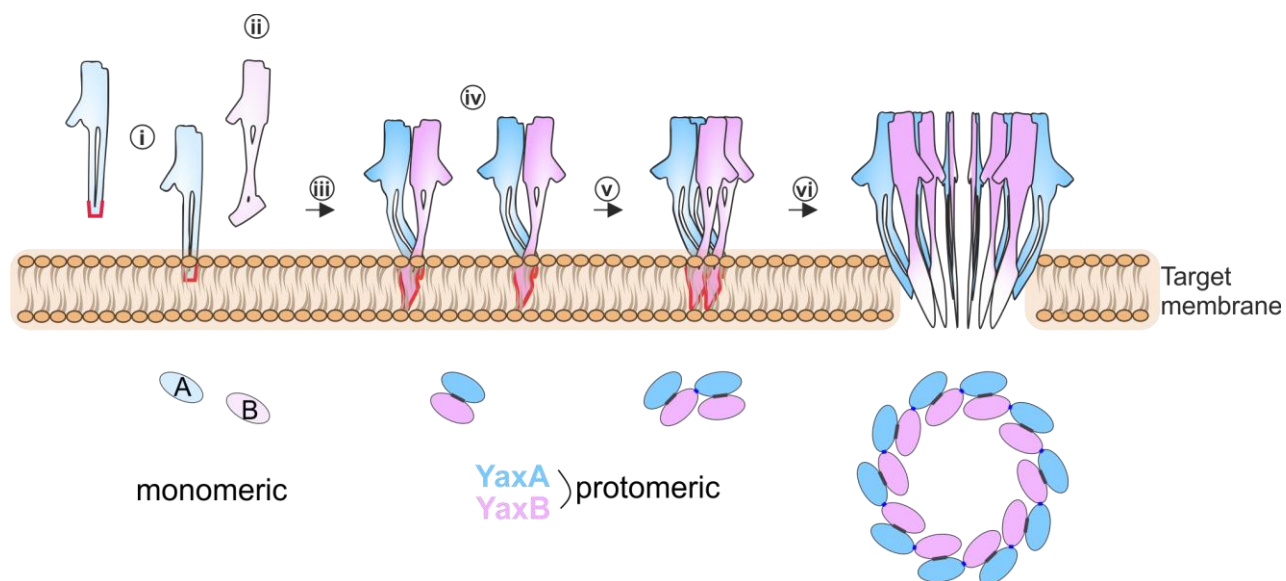

Fig. 5.2 Proposed assembly pathway of the YaxAB pore and comparison with ClyA: schematic overview of our proposed YaxAB pore assembly pathway at targeted membranes. i) YaxA binds to membranes via its hydrophobic foot, ii) after which YaxB, harboring no membrane binding capacity on its own, iii) is recruited via initial interaction between the head domains. iv) At this stage, YaxB's foot domain rearranges to its membrane-inserted state, stabilized by YaxA's hydrophobic foot. v) Another membrane-bound YaxAB dimer interacts with the first dimer via the *trans* YaxA-YaxB contact sites. vi) Further association of protomers eventually drive formation of the closed YaxAB pore complex. Red outlines indicate the exposure of membrane-active moieties.

Upon proximity to a susceptible membrane, YaxA can insert into the lipid bilayer through its solvent exposed hydrophobic foot domain. YaxA likely remains monomeric, as no obvious YaxA-YaxA contacts can be derived from the cryo-EM pore model. YaxB can subsequently be recruited to the membrane by interaction with YaxA's head domain, projecting away from the membrane. This heterodimerization may induce opening of the YaxB foot domain, allowing its amphipathic helices to insert into the membrane and engage in the conserved interface with YaxA's foot domain. At this point, the *trans*-interface between YaxA and YaxB is exposed and could mediate association with a second, membrane-bound YaxA-YaxB heterodimer. Further oligomerization towards the closed YaxAB pore may proceed analogous to the homomeric ClyA system as described above.

This proposed pathway of pore formation (**Fig. 5.2**) is derived from analysis of the cryo-EM structure and by biochemical assays discriminating between membrane-binding abilities of YaxA and YaxB. It is important to point out that this model likely holds true *in vitro*, using separately expressed and purified YaxA and YaxB. However, past studies have demonstrated that co-expression of XaxAB[1] (from X. nematophila) or YaxAB[3] produce lytic bacterial lysates, whereas a mixture of subunit containing lysates fails to do so. This latter observation can be explained by the aggregation of YaxAB complexes, when YaxA and YaxB are mixed, which appears to sequester the membrane-active domains of the proteins. While this behavior rationalizes the necessity of a sequential mode of action in vitro (thus avoiding formation of aggregated "dead-end" pores), it remains open how the toxin would retain lytic activity when the two components are coexpressed in the same cytoplasm. The puzzling discrepancy in lytic potential, between co-expressed and individually expressed YaxAB subunits, certainly warrants further investigation, especially since there is a consensus for two orthologues of this PFT class. However, *in vitro* experiments are unlikely to provide the level of insight required to understand this peculiar behavior. Attempts were made to co-express both YaxA/YaxB and XaxA/XaxB, but in neither case was it possible to copurify the two toxin subunits, which is why the two Yersinia subunits were expressed and purified separately for the experiments presented in this thesis. It should be stressed that the structural and biochemical data in this thesis are still pertinent to understanding the lytic mechanism of YaxAB, albeit outside the *in vivo* context. Importantly, this work identified and validated the membrane-active regions of both YaxA and YaxB.

Furthermore, a structural and biochemical framework for understanding the functional segregation of YaxA and YaxB as membrane-binding subunit and lytic effector, respectively, could be derived. Ascertaining if the sequential action of YaxAB holds true also *in vivo* will be an important piece of information regarding the biological role of the PFT as a virulence factor.

What can be learnt, from the structural and biochemical data on YaxAB, about the wider ClyA family of α-PFTs? After all, this branch of toxins includes homomeric (ClyA), binary (YaxAB) as well as tripartite (Nhe, Hbl) assemblies, making it an unusually diverse superfamily of PFTs (**Fig. 5.3**). A direct comparison between YaxAB and ClyA pores makes clear the very different architectures between these two PFTs. A comprehensive view on this family of toxins will be possible once structures of the tripartite Nhe or Hbl systems become available. So far, high-resolution models of Hbl-B[8] and NheA[9] are available, which are closely related to each other and also to ClyA. Intriguingly, both Nhe and Hbl toxins require sequential modes of assembly on membranes *in vitro* just like YaxAB orthologues[10], yet experimental evidence suggests that the three protein components of Hbl (Hbl-B, Hbl-L$_1$, Hbl-L$_2$) and Nhe (NheA, NheB, NheC) may assemble as non-stoichiometric pores. Indeed it was proposed that for each of these tripartite systems, two subunits assemble stoichiometrically, while the third acts substoichiometrically as a lytic effector[10,11].

With biochemical evidence supporting the strong functional segregation of YaxA and YaxB, it can be anticipated that Nhe and Hbl subunits also fulfil distinct roles in pore assembly and lysis. More recently, the crystal structure of the soluble form of the insecticidal Cry6Aa PFT was solved[12], revealing homologous topology to Hbl-B and NheA. There is so far no evidence that Cry6Aa functions as a heteromer. Thus, the wider ClyA family of PFTs have conserved a structural frame of the helical bundle head domain (which structurally aligns reasonably well across the different family members) whereas they reveal strikingly divergent compositions. Future biophysical work, in reference to the comprehensive single-molecule approach undertaken to dissect the assembly principles for ClyA[7], will be crucial to prove whether this compositionally diverse PFT family follows a unified lytic mechanism.
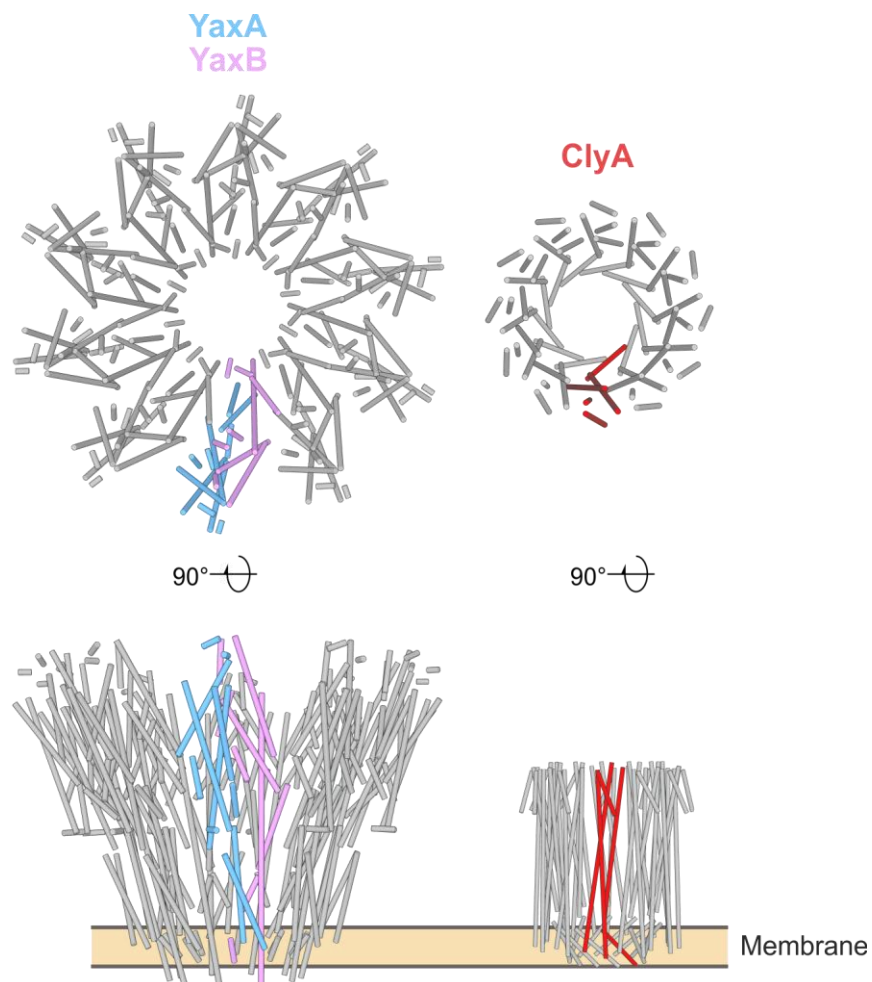
Fig. 5.3 Comparison of ClyA family pore architectures. For a to-scale comparison between YaxAB and ClyA pores (PDB accession code 2WCD) the structures were tiled in UCSF Chimera. The golden bar indicates approximate membrane boundaries.

Bibliography

1. Vigneux, F. *et al.* The xaxAB Genes Encoding a New Apoptotic Toxin from the Insect Pathogen Xenorhabdus nematophila Are Present in Plant and Human Pathogens. *J. Biol. Chem.* **282,** 9571–9580 (2007).

2. Jubelin, G. *et al.* Studies of the dynamic expression of the Xenorhabdus FliAZ regulon reveal atypical iron-dependent regulation of the flagellin and haemolysin genes during insect infection. *Environ. Microbiol.* **13,** 1271–1284 (2011).

3. Wagner, N. J., Lin, C. P., Borst, L. B. & Miller, V. L. YaxAB, a Yersinia enterocolitica Pore-Forming Toxin Regulated by RovA. *Infect. Immun.* **81,** 4208–4219 (2013).

4. Zhang, X. *et al.* XaxAB-like binary toxin from Photorhabdus luminescens exhibits both insecticidal activity and cytotoxicity. *FEMS Microbiol. Lett.* **350,** 48–56 (2014).

5. Mueller, M., Grauschopf, U., Maier, T., Glockshuber, R. & Ban, N. The structure of a cytolytic α-helical toxin pore reveals its assembly mechanism. *Nature* **459,** 726–730 (2009).

6. Wallace, A. J. *et al.* E. coli hemolysin E (HlyE, ClyA, SheA): X-ray crystal structure of the toxin and observation of membrane pores by electron microscopy. *Cell* **100,** 265–276 (2000).

7. Benke, S. *et al.* The assembly dynamics of the cytolytic pore toxin ClyA. *Nat. Commun.* **6,** 6198 (2015).

8. Madegowda, M., Eswaramoorthy, S., Burley, S. K. & Swaminathan, S. X-ray crystal structure of the B component of Hemolysin BL fromBacillus cereus. *Proteins Struct. Funct. Bioinforma.* **71,** 534–540 (2008).

9. Ganash, M. *et al.* Structure of the NheA Component of the Nhe Toxin from Bacillus cereus: Implications for Function. *PLoS ONE* **8,** e74748 (2013).

10. Sastalla, I. *et al.* The Bacillus cereus Hbl and Nhe Tripartite Enterotoxin Components Assemble Sequentially on the Surface of Target Cells and Are Not Interchangeable. *PLoS ONE* **8,** e76955 (2013).

11. Tausch, F. *et al.* Evidence for Complex Formation of the Bacillus cereus Haemolysin BL Components in Solution. *Toxins* **9,** 288 (2017).

12. Dementiev, A. *et al.* The pesticidal Cry6Aa toxin from Bacillus thuringiensis is structurally similar to HlyE-family alpha pore-forming toxins. *BMC Biol.* **14,** (2016).

Chapter 6

Appendix

Table 6.1: Minimal medium supplements

1L 100x trace elements	EDTA	5 g
	$FeCl_3$	0.8 g
	$ZnCl_2$	0.05 g
	$CuCl_2$	0.01 g
	$CoCl_2$	0.01 g
	H_3BO_3	0.01 g
	$MnCl_2$	1.6 g
	Ni_2SO_4	spatula tip
	molybdic acid	spatula tip
500mL 1000x vitamins	riboflavin	0.5 g
	niacinamide	0.5 g
	pyridoxine monohydrate	0.5 g
	thiamine	0.5 g

Table 6.2: X-ray data collection and refinement statistics
Each dataset was collected from a single crystal. Values in parentheses are for highest-resolution shell.

	YaxA (PDB – 6EK7)	PaxB (PDB – 6EK4)	YaxB (PDB – 6EK8)	YaxA (SeMet)	PaxB (SeMet)
Data collection					
Space group	C2	$P2_1$	$P6_522$	C2	$P2_1$
Cell dimensions					
a, *b*, *c* (Å)	203.8, 24.1, 109.4	104.6, 70.2, 136.9	111.7, 111.7, 169.7	205.1, 24.1, 106.8	105.3, 70.0, 136.3
α, β, γ (°)	90, 113.92, 90	90, 108.41, 90	90, 90, 120	90, 113.97, 90	90, 110.67, 90
Resolution (Å)	50-1.8 (1.9-1.8)	50-2.8 (2.9-2.8)	50-4.0 (4.1-4.0)	30-2.8 (2.9-2.8)	30-3.6 (3.7-3.6)
R_{meas} *(%)*	5.5 (55.0)	6.9 (51.5)	7.7 (95.8)	17 (68.1)	15.1 (76.2)
$I / \sigma I$	11.5 (2.0)	9.7 (1.8)	13.0 (2.1)	7.9 (2.7)	14.8 (5.0)
Completeness (%)	97.8 (97.6)	95.3 (94.7)	98.7 (99.2)	98.7 (99.2)	99.6 (99.7)
Redundancy	3.7	2.9	5.1	4.8	14.9
Refinement					
Resolution (Å)	15-1.8	15-2.8	50-4.0		
No. reflections	43,138	42,429	5,351		
R_{work} / R_{free} (%)	19.0 / 22.8	24.1 / 26.8	32.1 / 33.9		
No. atoms					
Protein	3,211	10,874	2,175		
Ligand/ion	72	4			
Water	240	226			
B-factors (Å^2)					
Protein	55.2	85.9	189.0		
Water, ligand	69.5	83.0			
R.m.s. deviations					
Bond lengths (Å)	0.009	0.004	0.007		
Bond angles (°)	0.9	0.7	1.0		
Ramachandran plot					
Favored (%)	98.6	97.6	98.3		
Allowed (%)	1.4	2.2	1.7		
Disallowed (%)	0	0.2	0		

Table 6.3: Cryo-EM data collection, refinement and validation statistics

	YaxAB (20-mer) (EMDB-3885) (PDB - 6EL1)
Data collection and processing	
Magnification	59,000
Voltage (kV)	300
Electron exposure (e–/Å^2)	60
Defocus range (μm)	1.1 – 2.5
Pixel size (Å)	1.106
Symmetry imposed	C10
Initial particle images (no.)	178,149
Final particle images (no.)	24,822
Map resolution (Å)	6.1
FSC threshold	0.143
Map resolution range (Å)	4.8 – 7.0
Refinement	
Initial model used (PDB code)	6EK7, 6EK8
Model resolution (Å)	6.1
FSC threshold	0.143
Model resolution range (Å)	4.8 – 7.0
Map sharpening B factor (Å^2)	-331
Model composition	
Protein residues	6,830
B factors (Å^2)	
Protein	322
R.m.s. deviations	
Bond lengths (Å)	0.005
Bond angles (°)	0.93
Validation	
MolProbity score	1.87
Clashscore	7.4
Poor rotamers (%)	0.5
Ramachandran plot	
Favored (%)	92.5
Allowed (%)	7.5
Disallowed (%)	0
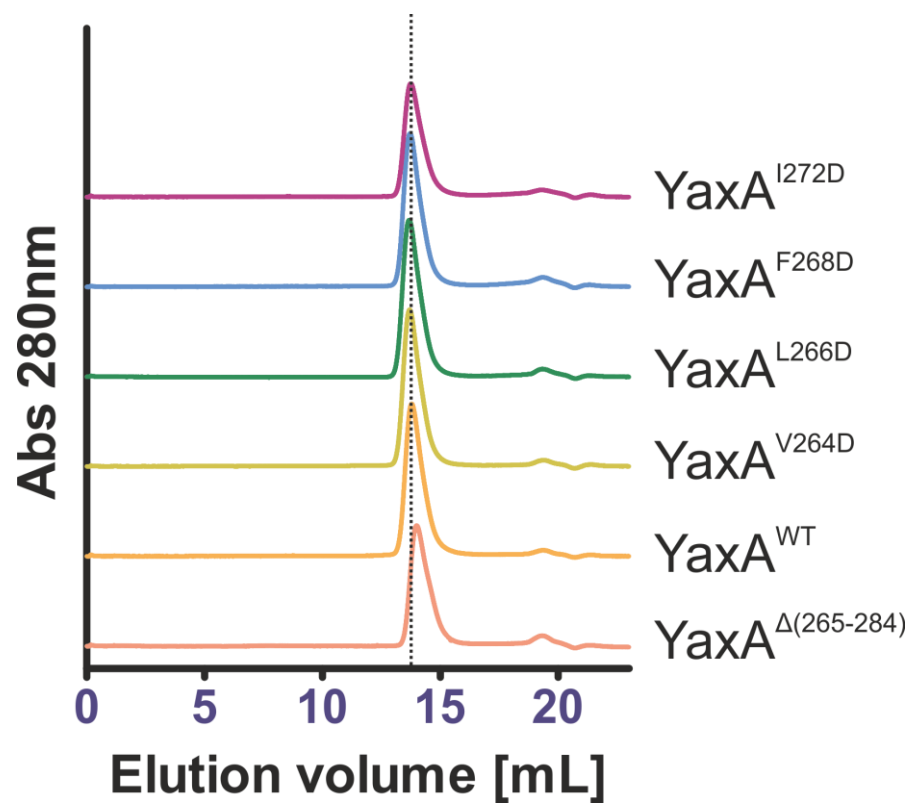
Fig. 6.1 Structural integrity of YaxA mutants studied. Gel filtration traces (Superdex 200 10/300 increase) of YaxA mutants used in this work, including wild-type (WT) protein. For each run, 500 μL of protein at ~0.3 mg / mL was injected.

List of publications

- [*#]Bräuning, B., [*]Bertosin, E., Praetorius, F., Ihling, C., Schatt, A., Adler, A., Richter, K., Sinz, A., Dietz, H., Groll, M. (2018). **Structure and mechanism of the two-component α-helical pore-forming toxin YaxAB.** Nature Communications *9, 1806*, doi: 10.1038/s41467-018-04139-2

- [*]Wachtel, R., [*]Bräuning, B., Mader, S.L., Ecker, F., Kaila, V.R.I., Groll, M., Itzen, A. (2018). **The protease GtgE from Salmonella exclusively targets inactive Rab GTPases.** Nature Communications *9*, 44, doi: 10.1038/s41467-017-02110-1

- Solomon, H., Bräuning, B., Fainer, I., Ben-Nissan, G., Rabani, S., Goldfinger, N., Moscovitz, O., Shakked, Z., Rotter, V., and Sharon, M. (2017). **Post-translational regulation of p53 function through 20S proteasome-mediated cleavage.** Cell Death Differ. September 8 2017.

- Kolek, S.A., Bräuning, B., and Stewart, P.D.S. (2016). **A novel microseeding method for the crystallization of membrane proteins in lipidic cubic phase.** Acta Crystallogr F Struct Biol Commun *72*, 307–312.

[*]Equal contributing first author

[#]Corresponding author

Acknowledgements

Anhang

Eidesstattliche Erklärung

Ich erkläre an Eides statt, dass ich die bei der promotionsführenden Einrichtung

Technische Universität München – Fakultät Chemie

der TUM zur Promotionsprüfung vorgelegte Arbeit mit dem Titel:

Structural and biochemical characterization of the YaxAB pore-forming toxin from Yersinia enterocolitica

in <u>Fakultät Chemie – Lehrstuhl Biochemie</u>

   Fakultät, Institut, Lehrstuhl, Klinik, Krankenhaus, Abteilung

unter der Anleitung und Betreuung durch: <u>Professor Dr. Michael Groll</u> ohne sonstige Hilfe erstellt und bei der Abfassung nur die gemäß § 6 Ab. 6 und 7 Satz 2 angebotenen Hilfsmittel benutzt habe.

☒ Ich habe keine Organisation eingeschaltet, die gegen Entgelt Betreuerinnen und Betreuer für die Anfertigung von Dissertationen sucht, oder die mir obliegenden Pflichten hinsichtlich der Prüfungsleistungen für mich ganz oder teilweise erledigt.

☒ Ich habe die Dissertation in dieser oder ähnlicher Form in keinem anderen Prüfungsverfahren als Prüfungsleistung vorgelegt.

☒ Die vollständige Dissertation wurde in <u>englischer Sprache</u> veröffentlicht. Die promotionsführende Einrichtung

Technische Universität – Fakultät Chemie

hat der Veröffentlichung zugestimmt.

☒ Ich habe den angestrebten Doktorgrad noch nicht erworben und bin nicht in einem früheren Promotionsverfahren für den angestrebten Doktorgrad endgültig gescheitert.

☐ Ich habe bereits am _____ bei der Fakultät für _____

_____

der Hochschule _____

unter Vorlage einer Dissertation mit dem Thema _____

_____

die Zulassung zur Promotion beantragt mit dem Ergebnis: _____

_____

Die öffentlich zugängliche Promotionsordnung der TUM ist mir bekannt, insbesondere habe ich die Bedeutung von § 28 (Nichtigkeit der Promotion) und § 29 (Entzug des Doktorgrades) zur Kenntnis genommen. Ich bin mir der Konsequenzen einer falschen Eidesstattlichen Erklärung bewusst.

Mit der Aufnahme meiner personenbezogenen Daten in die Alumni-Datei bei der TUM bin ich

☒ einverstanden,   ☐ nicht einverstanden.

GARCHING , 02.07.18
Ort, Datum, Unterschrift